University of Cincinnati

Date: 7/8/2022

I, Benjamin M Millard, hereby submit this original work as part of the requirements for the degree of Master of Science in Aerospace Engineering.

It is entitled:

An Investigation of Diffraction, Reinitiation and Amplification Behaviors in Detonations of Varying Fuel-Oxidizer Mixtures

Student's name: **Benjamin M Millard**

This work and its defense approved by:

Committee chair: Daniel Cuppoletti, Ph.D.

Committee member: Jongguen Lee, Ph.D.

Committee member: Timothy Ombrello, Ph.D.

UNIVERSITY OF Cincinnati

43053

An Investigation of Diffraction, Reinitiation, and Amplification Behaviors in Detonations of Varying Fuel-Oxidizer Mixture

A thesis submitted to the
Graduate School
of the University of Cincinnati
in partial fulfillment of the
requirements for the degree of

Master of Science

in the Department of Aerospace Engineering and Engineering Mechanics
College of Engineering and Applied Sciences

By
Benjamin Millard

Bachelor of Engineering, Mechanical Engineering
University of Dayton, December 2019

Date: 8 July 2022

Committee Chair: Dr. Daniel Cuppoletti

Abstract

This study seeks to further explore a detonation amplification that is caused by detonation diffraction and reinitiation event as a detonation passes through an area expansion. A study of changes in detonation amplification behavior was conducted using varying back pressure, equivalence ratios, and fuel oxidizer mixture to change the cell size and subsequent incoming detonation criticality. Detonation criticality being defined as the actual number of detonation cells divided by the critical number of cells also is theorized to influence relationship between area expansion and amplification behavior. A new pneumatic system was developed to allow the detonation reaction mixture to be controlled. This detonation was then passed into an area expansion chamber where the amplification process was observed using ion probes to measure wave speed and pressure probes to measure pressure impulse after which the detonation is exhausted out of the chamber.

Three amplification behaviors are observed, spike amplification, steady amplification, and end wall amplification. The steady amplification behavior occurs in detonations close to criticality or in smaller area expansion. The steady amplification behavior lacks the significant pressure spike at reinitiation with this reinitiation happening near the inlet of the chamber, reaching a pressure amplification of 2 to 3 times the steady-state impulse. Spike amplification occurred at lower detonation critically or in larger area expansion and is characterized by a reinitiation spike in impulse pressure to a peak amplification of between 3.5 to 5 times the incoming steady-state impulse with this typically occurring further in the chamber. This spike is followed by rapid attenuation of the pressure impulse to a lower amplified state with a slower attenuation observed during steady amplification. The third behavior of end wall amplification was observed to not recouple until near the end wall, this results in the peak amplified state being at the outlet of the

chamber. This was amplified further than either of the other two behavior and was characterized by a dramatic recoupling at the end wall. This behavior was generally observed in detonations that are both very subcritical and when expanding into a larger area expansion. The trend observed when changing criticality is that some threshold crossed in which a detonation will first display steady amplification at low cell size, then spike amplification behavior when the criticality is decreased, and then finally end wall amplification once the cell size passes a final threshold. The effect of cell size appears to be compounded by the change in area ratio with detonations being observed to transition between detonation behavior when changing the area ratio without changing the incoming detonation criticality. This study was however limited in its ability to directly measure detonation criticality and instead draws conclusions based on cell size data from previous studies.

Lastly, an optical study showed that two different reinitiation behaviors observed in the spike amplification range with one of the reinitiation behaviors matching that found in a previous study, with a third behavior capture that is believed to show the reinitiation mechanism at the end wall amplification behavior.

Acknowledgments

I would like first to thank my parents for supporting me I while pursued my master's degree. I had decided to attend grad school after getting my bachelor's at the last moment and they were very supportive in my pursuits. They helped me throughout this process, whether it was allowing me to stay at their house during work from home at the height of the pandemic, allowing me to vent over the phone when I had a setback during testing, or get me dinner when I had been locked in my apartment for days working on my thesis.

I would like to next thank my advisor Dr. Daniel Cuppoletti who has helped me navigate the graduate school process, supported me in my research pursuits, and allowed me to grow professionally as an engineer. There is a reason I signed up to continue to Ph.D. with Dr. Cuppoletti.

I would like to thank Dr. Tim Ombrello working at AFRL, who has worked closely with us to perform this research and was instrumental in getting this work funded under a DAGSI fellowship funded directly by AFRL. I would also like to thank him for taking the time out of his busy schedule to serve on the thesis committee and provide feedback.

I would like to thank Dr. Jongguen Lee for likewise serving on my thesis committee and providing feedback on my thesis. I would like to thank Curt Fox, Slade Brooks, Ethan Verquer, Ryan O'Rorke, and Vincent Onoja for their help in conducting the experiments. I would also like to thank the University of Cincinnati and Mr. & Mrs. Dean Godown for their financial support as I pursued my master's degree.

Table of Contents

Table of Figures

Table of Equations

List of Tables

Nomenclature

ν	Dynamic Viscosity
P	Pressure
$\dot{m}$	Mass Flow
γ	Heat Capacity
λ	Detonation Cell Size
Φ	Equivalence Ratio
$\dot{V}$	Volume Flow
T	Temperature
R	Gas Constant
SG	Specific Gravity
GCF	Gas Correction Factor
Tr	Transmissibility
n	Number of Mols
X	Mole Fraction
MW	Molecular Weight

Y	Mass Fraction
R_u	Universal Gas Constant
ρ	Density
$\frac{A}{F}$	Air-Fuel Ratio
Δx	Displacement
t	time
Ea	Activation Energy

Abbreviations

DDT	Deflagration to Detonation Transition
CJ	Chapman-Jouguet
ZND	Zel'dovich, Neumann, and Döring
P&ID	Plumbing and Instrumentation Diagram
MFC	Mass Flow Controller
SLPM	Standard Liters Per Minute
LPM	Liters Per Minute
PLC	Programmable Logic Controller
NI	National Instruments
TTL	Transistor-Transistor Logic
DAQ	Data Acquisition
FEA	Finite Element Analysis
ND	Neutral Density
LPAS	Low-Pressure Air System
SG	Savitzky–Golay
FPS	Frames Per Second

1-Introduction

Detonation combustion has recently become an area of increasing interest with related research moving away from seeking a more fundamental understanding of the detonation phenomenon to focus more on practical applications. Detonation combustion offers pressure gain and heat release benefits over deflagration combustion due to the control volume nature of detonation combustion resulting in an increase in usable work compared to unconfined deflagration combustion which acts more along the lines of a constant pressure reaction where work is wasted during expansion. Detonation combustors use the pressure gain process to improve the cycle of an engine and extract more usable work from a given amount of fuel than in the traditional Brayton cycle. Using detonation to ignite a combustor on the other hand has been shown to produce a more reliable ignition event in extreme ignition scenarios such as that found in scramjets. This is due to the global energy deposition compared to the localized energy deposition of traditional spark ignition systems [1-2]. A drawback of detonations is inherent to detonation combustion mechanism, which is the disruptive nature of the shockwave associated with a detonation. The strength of this shockwave is directly related to the area of the shock front and in turn the energy deposition of a detonation. This results in a detonation across a small annulus being less disruptive to the operation of the engine, but the detonation will be too weak to perform the task while a larger annulus will produce a strong impulse but also produce a strong distribution that is often detrimental to the overall operation of an engine. To address this issue, unsteady detonation phenomenon and Detonation to Deflagration Transition (DDT) processes have been looked at as means to control the impulse of the detonation. This can take the form of amplifying the detonation for better performance or decreasing the disruptive impulse to allow for smoother operation of an engine.

1.1-CJ Detonation

Steady-state detonations are modeled as a one-dimensional approximation of a detonation wave, an approach pioneered separately by Dave Chapman and Émile Jouguet. Chapman-Jouguet (CJ) theory models an infinitesimally thin detonation, thus ignoring any effect of distance between the shock and flame front or any detonation structure. The solution relies on the Rankine–Hugoniot relations to derive a curve for the relationship between the pre-shock and post-shock states called the Rankine-Hugoniot curve, derived using Equation 2, and the relationship between the pre-heat release state and the post-heat release state called the Rayleigh line, calculated using Equation 1. With the structure of the detonation being ignored in this theory, the relationship between the pre-combustion and the post-combustion states is the intersection of the Hugoniot curve and the Rayleigh line. This gives four unique solutions, a strong and weak detonation, and a strong and weak deflagration. CJ theory assumed that combustion is most stable when the Rayleigh line and Rankine-Hugoniot curve are tangential and thus only have two solutions, a CJ detonation, and a CJ deflagration. This solution is shown in Figure 1 with points D and E showing the respective CJ detonation and deflagration conditions. The initial theory justified this tangential solution as having the minimum detonation wave speed obtainable from the intersection Hugoniot curve and the Rayleigh line and was theorized to be the most stable. It was later shown that the CJ condition provides the lowest entropy solution and thus would be the theoretical stability point of any given one-dimensional combustion wave. Predictions using CJ detonation theory correlate strongly with experimental results for pseudo-one-dimensional detonations. However, CJ theory is limited to explaining the pre-combustion and post-combustion state of one-dimensional detonation waves and doesn't provide any insight into the structure of a detonation wave.

$$\frac{P_2 - P_1}{\nu_2 - \nu_1} = \dot{m}''^2$$

Equation 1: Rayleigh Line [3]

$$\frac{\gamma}{\gamma - 1}(P_2\nu_2 - P_1\nu_1) - \frac{1}{2}(P_2 - P_1)(\nu_2 + \nu_1) - q = 0$$

Equation 2: Rankine-Hugoniot Curve [3]

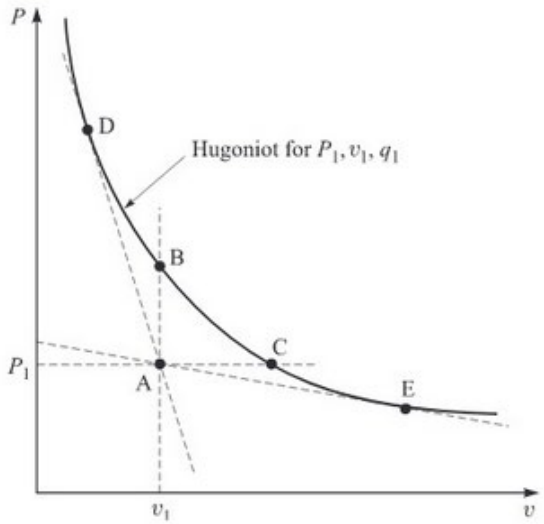

Figure 1: Rankine-Hugoniot Curve with tangential Rayleigh Lines AD and AE. Points D and E show the CJ detonation and deflagration points respectively [3]

1.2-ZND Detonation Structure Model

The first formal model for detonation structure is credited to independent investigations by Y. B. Zel'dovich, John von Neumann, and Werner Döring (ZND) and is shown in Figure 2 and Figure 3. The ZND model consists of the leading shock front that compresses the combustible gas and raises the temperature of the reactants to the auto-ignition point, shown as position 1 in Figure 3. Next comes an induction zone, shown as the area between position 1 and position 2' in Figure 3, where intermediate reaction species are produced through thermal disassociation caused by the initial shock, ultimately priming the reaction for rapid chain-branching. The induction zone is characterized by an elevated temperature zone over the initial condition but not elevated to the point of CJ temperature. This induction zone also is elevated in pressure and density over that of

the initial state and the final CJ condition with the gas in this zone being compressed by the initial shockwave but not undergoing the expansion caused by combustion heat release. These conditions within the induction zone are referred to as the Von Neman (VN) state. Once the intermediate species reach a critical mass within the induction zone the rapid chain-branching signifies the beginning of the reaction zone of the ZND detonation model, shown as the region between 2' and 2 in Figure 3. In this zone, the rapid heat release accompanying the rapid chain branching of the reaction results in an increase in temperature with a corresponding decrease in both pressure and density as the gas expands. This reaction zone lasts until chain branching has ceased and the detonation has reached the theoretical CJ state shown as position 2 in Figure 3. The thermal expansion of the gas as it leaves the reaction zone generates the thrust mechanism that creates and sustains the initial shock wave as the expanded gas is accelerated away from the reaction zone. Overall, the ZND model provides useful insight into the internal chemical kinetic behavior of a detonation. However, actual detonations rarely display behavior predicted by either the CJ Theory or the ZND model even in pseudo-one-dimensional conditions and instead develop either a two- or three-dimensional structure.

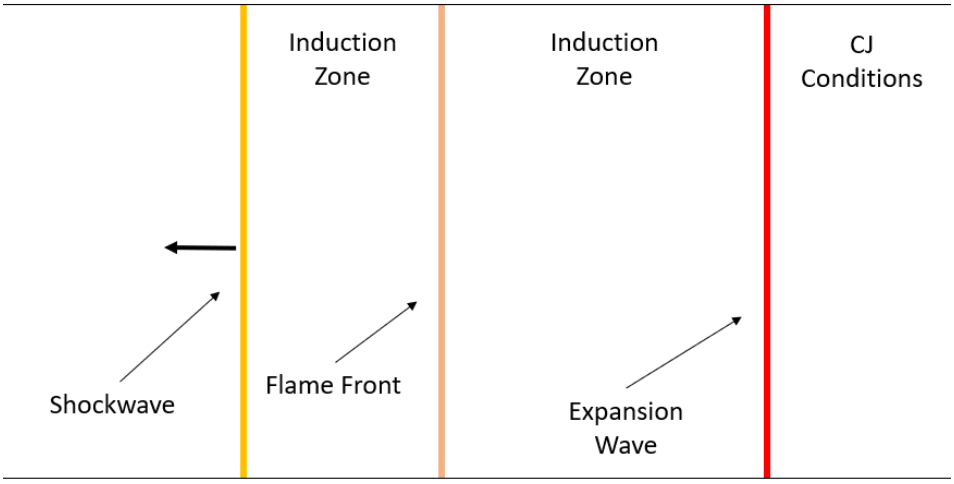

Figure 2: ZND Model Detonation Structure

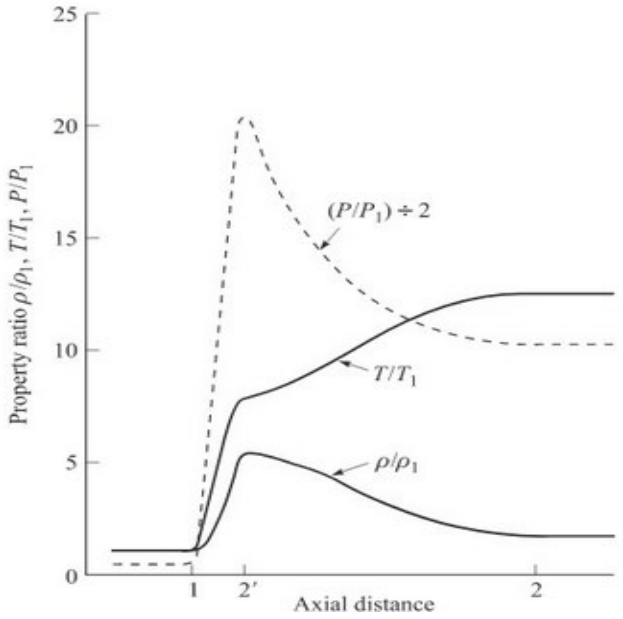

Figure 3: ZND Detonation state plotted vs detonation structure. Position 1 is the shock. Position 2' is the flame front. 2 is the CJ point [3]

1.3-Detonation Cells and Critical Tube Diameter

The ZND model and CJ theory are both limited to explaining one-dimensional detonation behavior and ignore any effects of multi-dimensionality that occur. Observations of two-dimensional and three-dimensional detonations generally show very different structures and behavior than cannot be explained by either the ZND model or CJ theory. The wavefront of a detonation is observed to be less uniform compared to the flat plane predicted by the CJ theory and ZND Model. This results in a fish-scale-like pattern of detonation cells developing when tracking the propagation of a detonation with a two-dimensional approximation shown in Figure 4. The detonation cells are formed from two transverse detonation waves reflecting off each other alternating between a Mach stem and incident shock. The point where the incident shock, shown as line A-B in Figure 4, the Mach stem, shown as line C-D in Figure 4, and the transverse shock meet is referred to as the triple point shown in Figure 4 as point 0. The size and number of

detonation cells are important indicators of detonation behavior. The cell size is typically measured by the maximum lateral width of the detonation cell and is denoted as λ.

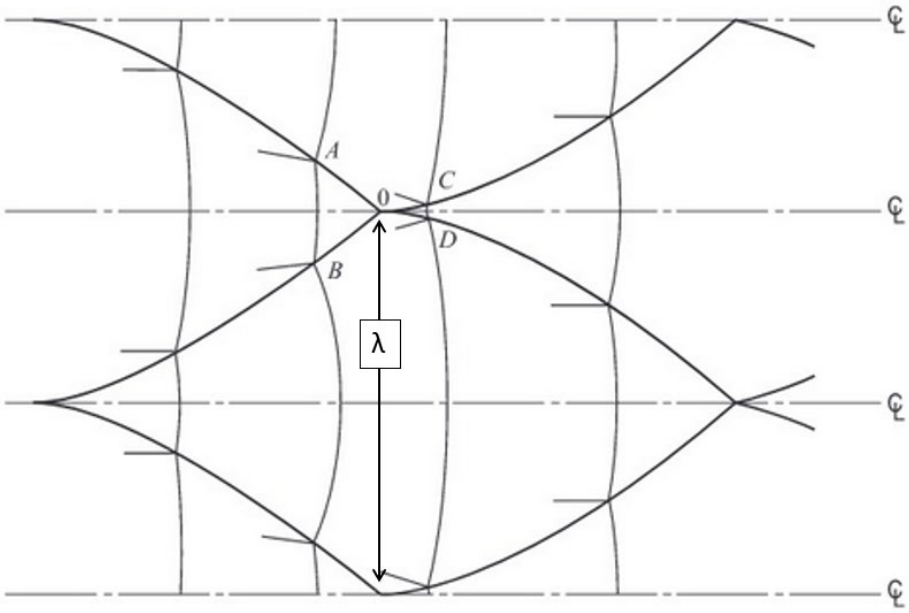

Figure 4: 2-D Idealized Detonation Cell Structure [3]

These detonation cells are a determining factor in the propagation behavior of a detonation during two and three-dimensional unsteady detonation behavior. This has been shown in an early study by Mitrofanov and Soloukhin [4] that showed for a given λ there is a critical tube diameter for which a pseudo-one-dimensional detonation propagating in a tube will have enough cells to successfully transition into a three-dimensional detonation when propagating into an unconfined space. This critical tube diameter was shown to be 13λ for a circular detonation tube and 10λ for a planar detonation tube for a detonation to successfully transition. A detonation below this critical tube diameter is said to be sub-critical and will undergo a transition to deflagration with the flame front completely decoupling from the shockwave and propagating separately. An incident detonation that is supercritical has enough cells to transition from a detonation tube into a three-dimensional detonation in unconfined space.

1.4-Detonation Diffraction and Reinitiation

A study by Pantow et al. [5] has a notable observation showing that this critical point is different when the detonation is semi-confined. This study observed that when a tube undergoes an area expansion with a detonation that would be typically sub-critical would be observed to successfully transition in the larger area section. These detonations were observed to diffract upon exiting the tube with this diffraction stretching the detonation structure and creating a larger induction and reaction zones. In an unconfined detonation, this diffraction would continue until the transitioning to deflagration is complete, but the confined area causes the reflected transverse shockwaves to reinitiate the detonation. Two sub-critical reinitiation behaviors were observed, transverse wave reinitiation and Mach stem reinitiation. In transverse reinitiation, the transverse portion of the detonation is the only part of the detonation to significantly decoupled, with reinitiation occurring once the shockwave reflects off the side wall and contacts the flame front and is shown in the left-most case in Figure 5. In Mach stem reinitiation, the diffraction of the detonation is complete across the entire wave front. When the shockwave reflects off the side wall, a Mach stem is created reinitiating the detonation locally by consuming the diffracted induct zone. As this Mach stem propagates transversely through the diffracted induction zone, shown as the middle case in Figure 5, it reinitiates the detonation as it travels until the two opposing Mach stems coalesce in the middle area completing the full reinitiation of the detonation.

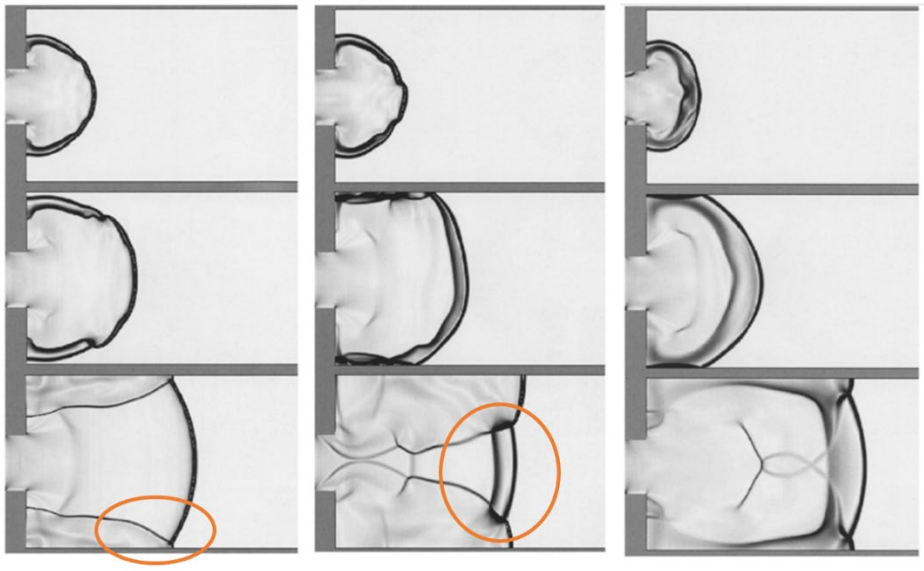

Figure 5: Simulation of 2D planar detonation transition though and area expansion showing different behavior. Left is Transverse detonation reinitiation. Middle is Mach stem reinitiation. Right is complete decoupling with no reinitiation [5]

1.5-Detonation Amplification

A recent observation by Cuppoletti et al. [6] has that shown this decoupling and reinitiation behavior is accompanied by transient amplification of the detonation with a follow-up optical study conducted by Chin et al [7] capturing high-speed imagery of this amplification process. This detonation amplification is defined by an increase in the heat deposition rate and detonation impulse pressure with a slight overdriving of the detonation. The overdriven wave speed allow is insufficient to explain the resultant amplification in pressure and temperature measured. In the Chin et al. [7] study, the high-speed imagery of the amplification process, seen in Figure 6, showed a sub-critical detonation diffracting upon entering a sudden area expansion with the shockwave undergoing spherical expansion and the flame front failing to do the same due to the sub-critical nature, with this shown in lines 1 and 2 in Figure 6. This diffraction causes a growth in the induction zone of the detonation resulting in a large slug of shocked but uncombusted reactants between the flame front and shockwave. The theory put forward by Cuppoletti et al. [6] and

supported by observations in Chin et al. [7] is that the transverse portion of the shockwave reflects off the side wall and coalesces in the middle of the expanded area section shown in lines 1-4 of Figure 6. This results in the shock interactions in the partially combusted reactants increasing heat release behind the flame front. As a result, the flame front accelerates to recouple with the shockwave resulting in the detonation reinitiating. When the detonation accelerates to recouple, it rapidly consumes the shock but uncombusted gas in the diffracted induction zones shown in line 4 of Figure 6. The consumption of this shocked but uncombusted gas is what is believed to be responsible for the amplification of the detonation with it creating an increased thrust impulse on the shockwave. The inertia of the shockwave and the impulse-like behavior of the resultant expansion thrust limit the ability of this detonation to overdrive. As a result, a transient spike in VN pressure is created with an accompanying spike in temperature in the induction zone with this being shown in the graphs in Figure 7. An observed increase in energy deposition rate then occurs. Once detonation is fully recoupled and excess uncombusted gas in the diffracted induction zone is consumed, this increased thrust is lost resulting in the amplified state beginning to attenuate back down towards the expected CJ conditions. It is important to note that the theory of the mechanism behind this amplification phenomenon is still a working theory, backed by only a few exploratory studies into the phenomenon. This work seeks to provide further insight into the mechanisms that causes the observed amplification behavior through a controlled parametric study on the dependence between the amplification mechanism and detonation criticality determined by the number of detonation cells in the incoming detonation and the critical number of detonation cells.

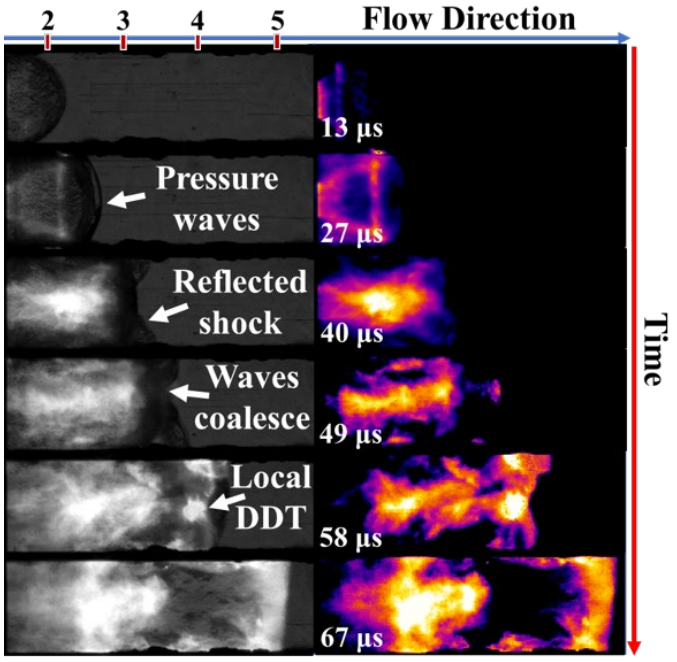

Figure 6: Schlieren and Chemiluminescence measurements of the Detonation Amplification Phenomenon [7]

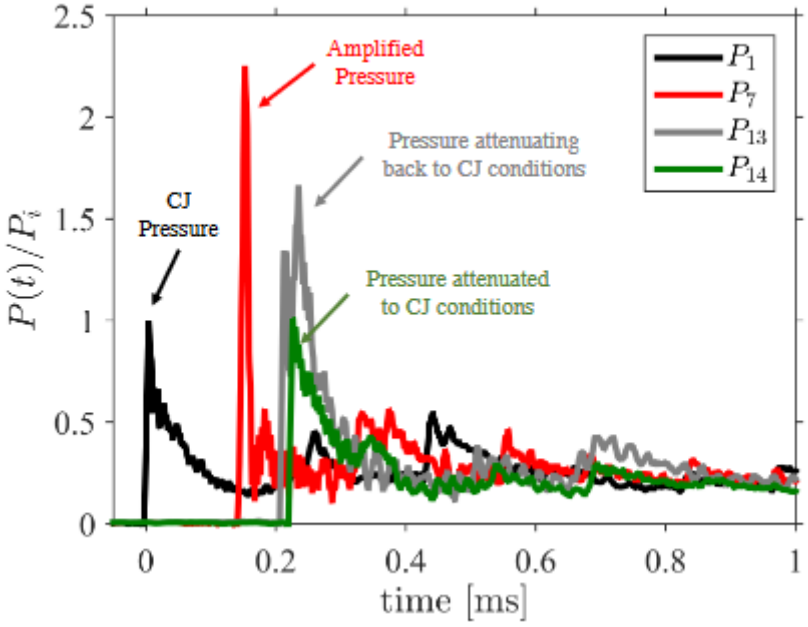

Figure 7:Temporal evolution of pressure illustrating pressure amplification [6]

2-Experiment Design

To further advance the study of this amplification phenomenon, an experiment was devised to vary the degree to which a detonation is critical. It was determined that the most practical way to change the criticality of a detonation was to change the λ of the detonation and keep a fixed tube geometry due rather than produce unique geometry for each test case. A twofold approach to vary λ was devised: 1) the equivalence ratio (Φ) would be varied first to allow for minor changes in λ 2) the reaction mixture could be changed to explore larger changes in λ. These changes were predicted based on general observation of λ with respect to changes in reactant mixtures [8]. The previous test rig that had been used to test this phenomenon lacked control over the fuel-oxidizer mixture being tested. As a result, a concept for a new test rid was built on the previous test rig design by Cuppoletti et. al [6] as a starting point. This new concept used mass flow controllers (MFC's) to regulate the flow of reactants into the pulse detonation with check valves and a flame arrestor to prevent flashback in order to allow for the continuous flow operation of the MFC's. The pneumatic system design needed to be compatible with multiple fuels and oxidizers to allow for the reaction mixture to be varied. The area expansion section of the detonation chamber would seek to reuse the modular test section devised by Cuppoletti et al. [6] for the geometry of the expanded area section. It was also identified that the move to continuous flow would introduce a significant amount of combustible gas into an exhaust system followed by an ignition event, so it was determined that a closed exhaust system with a large amount of dilution would be necessary to quench the combustion. Testing was envisioned to take place over two campaigns with the first focusing on taking pressure and wave speed data using the modular test section and then transitioning into a second campaign with an optically accessible test section for measuring high-

speed Schlieren and chemiluminescence. Lastly, it was desired that such a system be modular to facilitate further testing at other facilities beyond the initial two test campaigns.

2.1-Pneumatic System

The pneumatic system was designed around having three different gases, a gaseous oxidizer, a gaseous fuel, and an inert purging gas, all of which are supplied via a portable K-bottle. To maintain modularity in the system, the pneumatics control system was broken up into four different components: one main control module that regulates the mass flow of reactant into the pulse detonator and three gas supply submodules located at each gas supply bottle that regulate the supply of gas into the system and allow for the system to automatically purged at the nearest point to the gas supply. The Piping and Instrumentation Diagram (P&ID) that shows the entire pneumatics system is shown in Appendix 1.

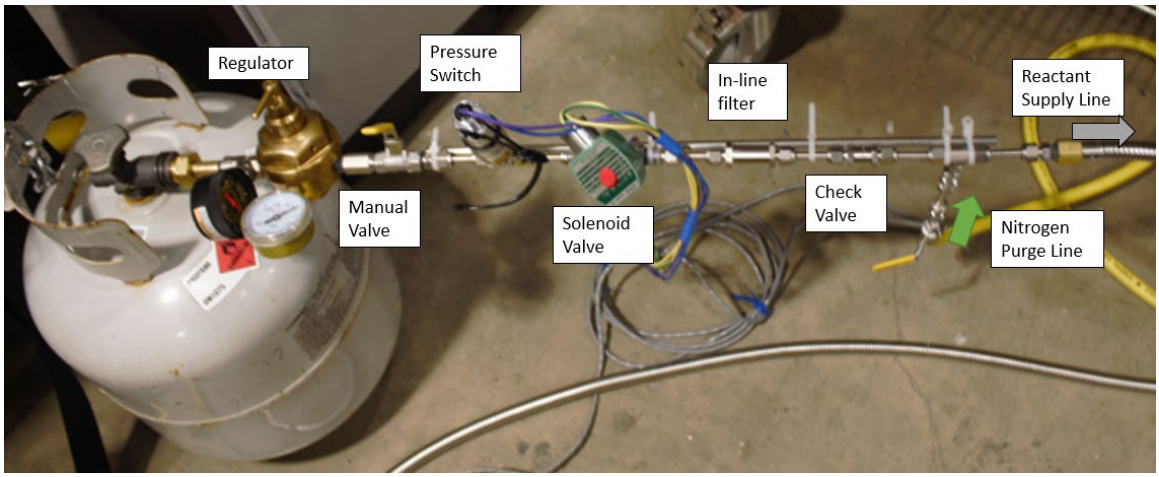

Figure 8: Fuel Gas Supply Control Module

The Oxidizer and Fuel control modules are functionally identical with the fuel control module shown in Figure 8. The oxidizer control module was made with readily available parts that had been cleaned of contamination that could potentially auto-ignite when used with pure oxygen. These modules consist of a pressure regulator mounted directly to the gas cylinder and a

manual shut-off valve. Following this valve is a pressure switch, which monitors the supply pressure of each line and communicates with the programable logic controller (PLC) to which line is pressurized. Immediately downstream of this pressure switch is an ASCO Redhat solenoid valve which allows the logic controller to automatically shut the gas supply on and off. A 0.5-micron particulate filter prevents any contamination from flowing downstream of the system, followed by a check valve. The line has a tee junction where the purging gas comes into the system through a check valve and a manual shut-off valve combination with the outlet to the tee being a flexible hose that feeds the main pneumatics control module. The purge gas control module shown in Figure 9 is a simplified design that similarly begins at the gas cylinder with a regulator. After this regulator is a pressure switch followed by a filter and then the ASCO solenoid valve. The gas then travels into a cross union with three outputs, two to the other gas supply submodules to supply them with purging gas and the third feeds directly to the main pneumatics control module. No manual shut-off control is present in this module as the main function is to supply other modules with purging gas and thus shutoff is handled either globally at the cylinder solenoid valve or locally at each control module using the manual shut-off valve.

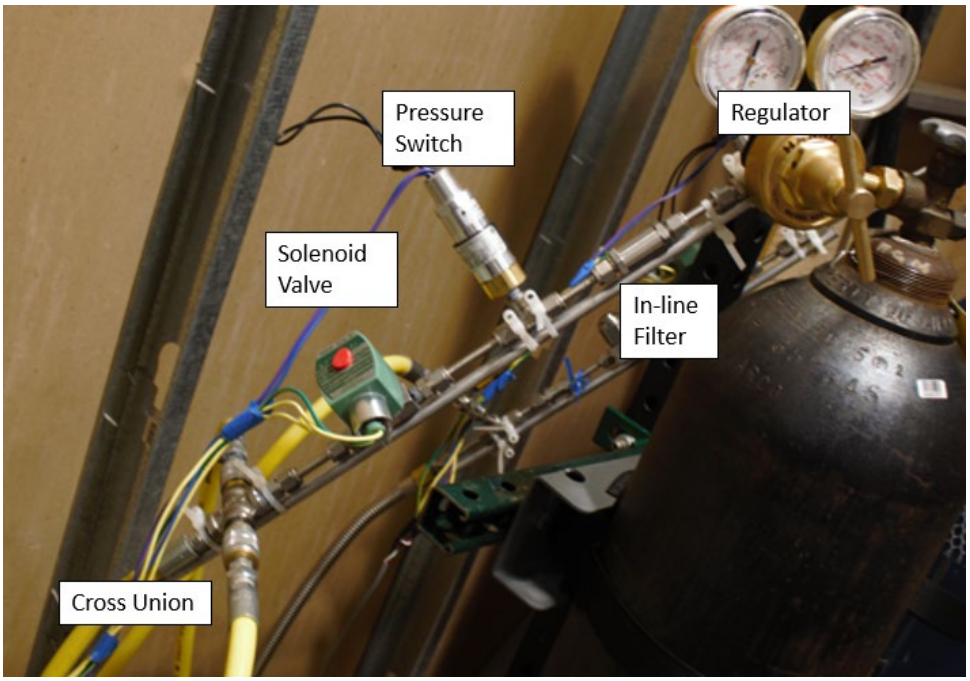

Figure 9: Purge Gas Supply Control Module

Each of the supply modules feeds the main pneumatics control module that is contained within a large aluminum case. A shutoff valve is located at each of the supply points for the three gases to allow for further isolated control. The fuel and oxidizer lines are then flown into MFC's which were sized based on a delivering 200 SLPM to the pulse detonator with the ratio being determined by the reaction mole fractions and Φ's being tested. A 500 SLPM rated MFC was used for the oxidizer flow, and a 100 SLPM rated MFC for the fuel flow. After these MFC's comes another ASCO shut-off solenoid valve that is controlled by the logic controller to allow for remote control of reactant flow, as the control valve located on the MFC's only act as a turn-down valve and does not completely shut off flow. After these shut-off valves are pressure transducers and T-type thermocouple probes to measure gas condition as they flow into the pulse detonator. The thermocouples have a direct readout on the lid to the aluminum case while the data from the pressure transducers have a readout on the control computer. The fuel side meets a tee joint with the N_2 purge gas supply being connected directly to this tee. This was done so that in the event of

an emergency, purge gas is delivered to the pulse detonator rapidly by bypassing the MFC's and various valves. Backflow of fuel gas through the direct purge line is prevented with another check valve. Both, the fuel and oxidizer lines are then plumbed out of the pneumatic box and into the detonator through stainless-steel flex lines.

2.2-Electrical and Logic Control

The logic control for the control system was split between a control computer and an onboard PLC. The PLC would handle the valve timing, safety logic, and the estop program while the computer would handle data acquisition, sending commands to the PLC to execute valve timing, and would handle triggering the ignition coil. This was done to isolate the pneumatic control from the computer such that if the computer froze or crashed, the pneumatic control would still operate, and the system could still be e-stopped. A Crouzet Millennium 3 CD20 PLC shown in Figure 10 was chosen as the PLC since it had the requisite number of integrated relays and was powered by 24V DC power. The computer used a National Instruments (NI) 6052E PCI card and a breakout board to interface with the system using a custom LabVIEW program as the interface, as seen in Appendix 3.

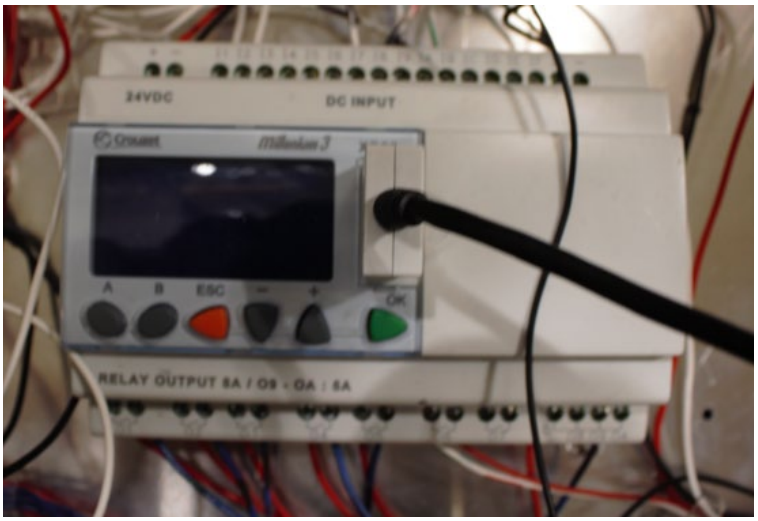

Figure 10: Crouzet Millennium 3 CD20 PLC

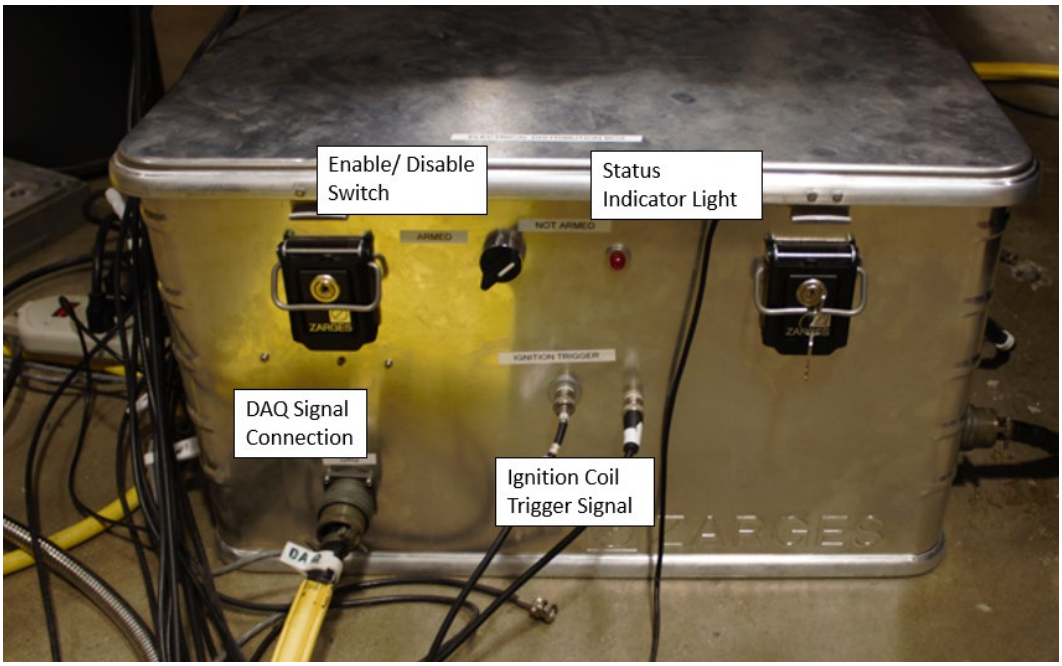

Figure 11: Electrical Box Front Panel

For the electronics, a second aluminum case was used to store the power supply and electronics control. This electrics box took in 120V AC power from the wall and converted it to DC using two 360W switching power supplies; one for 24V DC and another for 12V. This power distribution is shown in Figure 12. The majority of the system was powered off the 24V supply with the 12V supply primarily powering the ignition system with the cooling fans in each aluminum chest being secondary. Three six-pin electrical quick-connects shown in Figure 13, connect to each of the gas supply sub-modules to power and send valve open commands to the module and relay the pressure switch signal to the PLC from each module. Mounted above each of these plugs is a green LED indicator that displays when the respective line is pressurized when lit up. Another quick-connect runs both power and the trigger signal from the electrical box to the ignition system which is shown in the bottom right in Figure 14. The trigger for the ignition system originates on the NI breakout board but passes through the electrical box where a relay on the PLC acts as an enable for the ignition system. If the relay is open, the ignition system does not receive

the ignition trigger thus allowing the PLC to only enable the ignition system when it is ready. Two 16-pin quick-connects also run out of the electrical box, one running to the pneumatic control box also shown in Figure 14 and the other to the NI breakout board shown in Figure 11. The line running to the NI breakout board carries the PLC control signals and a separate E-stop signal controlled by an e-stop button near the control computer. The line running to the pneumatics control module run 12V and 24V power to the module as well as the control signals for the solenoid valves. The signals from the pressure transducers in the pneumatics control box and the pressure transducer in the exhaust system are passed from the pneumatic control module through the electronic box and into the NI breakout board operating as a secondary data acquisition system. An enable switch shown in Figure 11 and an arming switch shown in Figure 14 are located on the outside of the box. The enable switch turns the solenoid valve control over to the PLC allowing it to execute the valve sequence. The arming switch controls the power sent to the ignition coil allowing the coil to be disabled and preventing potential misfires of the system when flowing reactants during priming or purging. A red LED indicator light is mounted on the front panel of the box shown in Figure 11 and controlled by the PLC to indicate the status of the system. A rapidly blinking light indicates the PLC has indicated a fault. A slowly pulsing light indicates that the system is waiting to be primed. A solid light indicating that the system is primed with reactants and ready to fire.

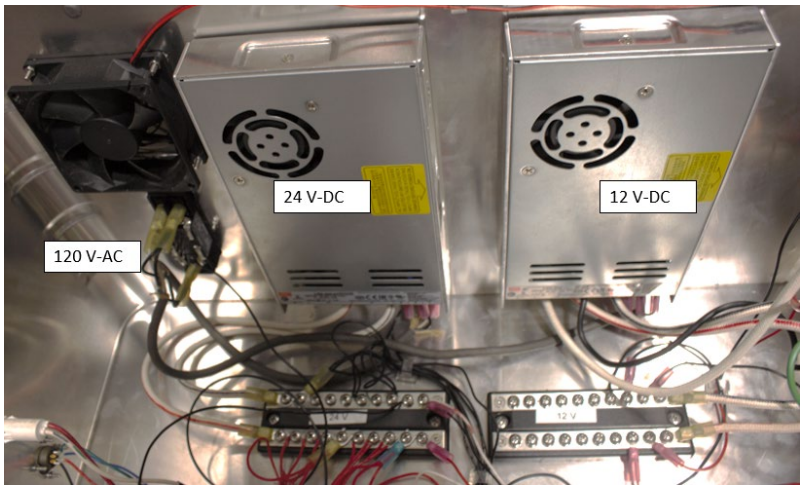

Figure 12: Power Supply and Distribution in Electrical Box

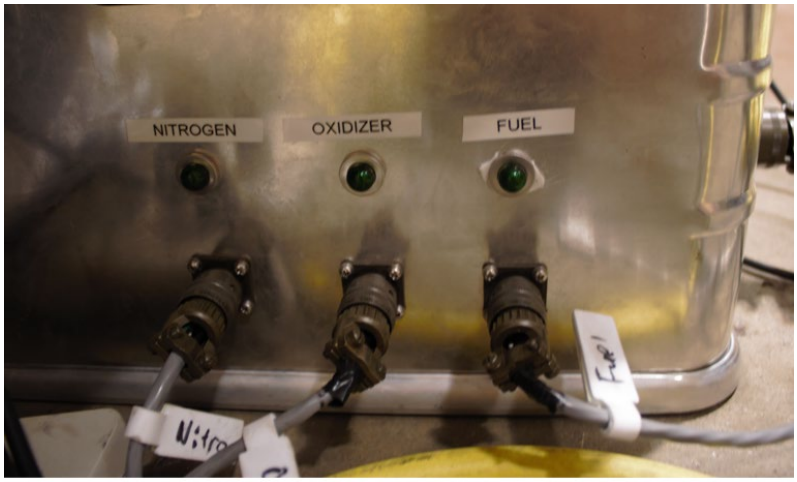

Figure 13: Control Module Electrical Connections and Indicator Lights

The PLC program was developed using the M3 Soft software provided with the PLC. The block diagram for this program is shown in Appendix 2 and consists of three main valve timing modules. The first is the prime modules which upon receiving an external trigger will open the nitrogen supply valve and the detonator supply valves, purging the air in the system with the purge gas. After a specified period of time, the nitrogen supply valve closes and the supply valve for the oxidizer and fuel gases are opened to fill the system with reactants. After another period of time, the two detonator supply valves are closed leaving the system primed with the reactants. Once this

module finishes, the pulse detonation module is enabled in the PLC logic and the prime module is disabled. Additionally, the external signal that primed the system is rerouted to the purge module allowing for one trigger signal to trigger both the prime and purge sequences when appropriate. Lastly, the module then turns the light on the front panel from a slow blinking red light to a solid red indicating the system status.

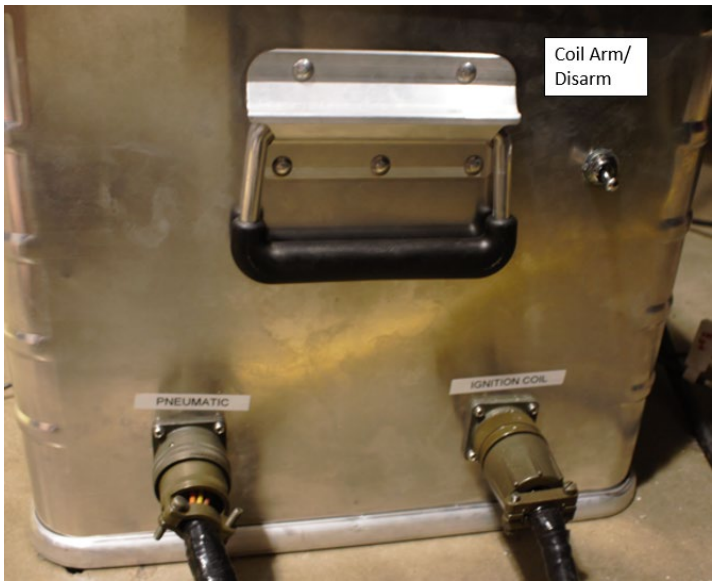

Figure 14: Pneumatic and Ignition Coil Connections and Coil Arm/Disarm Switch

The second module is the pulse detonation module that waits for a separate trigger from the NI board. Once this trigger is received both detonator supply valves open and flow a controlled ratio of reactant into the detonator. After a period of time to allow for the MFC's to stabilize, a relay on the PLC is closed allowing for the transistor-transistor logic (TTL) signal from the NI board to trigger the ignition system. This relay is only closed for a brief period of time to allow the ignition system to be fired and combustion initiated. The two detonator supply valves then are closed soon after this ignition window. After which, this module is then reset to allow the system to be fired in succession.

The last valve timing module is the purge module that is triggered off the same signal as the prime module. This is done to reduce the number of trigger signals needed to operate the PLC and is possible since the operation of the purge and prime modules are mutually exclusive. Due to this, the purge module is only able to be triggered in a primed state. Once the module is triggered the gas supply valves for the oxidizer and fuel are closed and the nitrogen supply valve and the detonator supply valves are opened to purge the reactants in the system. After a period of time, the purge gas supply valve is then closed with the detonator supply valves remaining open for further a period of time to allow the system to depressurize. The system is returned to the unprimed state in the PLC, waiting for the prime trigger signal.

These modules are built around the program's e-stop logic with the relays only allowed to open and close when the estop signal remains present. If the estop signal is cut off, the system will ignore any signals from other modules and will begin the e-stop valve sequence. This is done by shutting off the supply of the fuel and oxidizer and purging the system with nitrogen to quench any combustion in the system. Additionally, the ignition enable relay is forced open to prevent further ignition events in the system. After a period of time, the purge gas supply is shut off and the system is allowed to depressurize. The estop sequence is then completed at this point with the PLC now being locked out and presenting an estopped fault that requires the PLC program is reset. This is done so that the system cannot be restarted after being e-stopped without the entire system being reset and the PLC being returned to its original operation.

The last operation of the PLC worth mentioning is a manual valve override that is present that opens all of the solenoid valves in the system. This bypasses the pneumatic control of the PLC and allows the system to be controlled via the manual valves in the system. This serves two purposes, 1) the system can be completely depressurized up to the supply bottle instead of requiring

that the pressure regulators be removed to depressurize the system, 2) to allow for nonstandard operation of the system using the manual valves. This manual control was used during the MFC calibration rerouting the nitrogen supply to serve as the calibration gas. This override was prevented from being enabled when the automatic valve control in the PLC was enabled.

For the LabVIEW code and computer control, a simplistic control program was used for basic control of the system with the interface for this program being shown in Appendix 3. The main control is two buttons that correspond to the purge\prime trigger signal and the pulse detonation trigger signal. The purge/prime triggers are simple 5v pulses sent from the NI board to the PLC. The pulse detonation button similarly sends a 5v trigger signal to the PLC but also automatically sends the TTL signal to the ignition system after a specified delay. A parallel trigger signal is sent to the data acquisition system with this TTL signal. The length of this trigger signal is controlled by the LabVIEW program and can be set by a variable in the LabVIEW control panel. This is done as the length of TTL determines the charge time and thus energy output of the ignition coil. A secondary trigger button allows for the ignition trigger signal to be sent independently from the PLC pulse signal. The three pressure readings from the exhaust system and the fuel and oxidizer supply lines to the detonator are displayed in real time on the LabVIEW interface. The instantaneous values for each of these pressure readings are then recorded when the ignition event is triggered and written to an excel file automatically along with a rolling count of each detonation event. Lastly, a general lockout button and stop button are present that prevent the system from sending triggers to the PLC or ignition system and soft stop the LabVIEW program respectively.

2.3-Data Acquisition (DAQ) System

To measure the behavior of the detonation as propagates through the expansion chamber, two different types of probe measurements were used. The first was a piezoelectric pressure sensor

that used the variation in the voltage potential of a crystal to measure the impulse pressure of a detonation. These types of probes were selected due to their high-frequency response, high pressure range, and durability in a detonation environment. Four PCB Model 101AO2 pressure sensors were chosen for this purpose with the 5000 PSI rating of these sensors being in the expect amplified range of the detonation. These sensors are passed into a PCB Model 482C05 signal conditioner that applies signal filtering and gain to the signal and outputs a 0-10V signal. A room-temperature vulcanizing (RTV) silicone layer was applied to the diaphragm of these sensors as an ablative layer to prevent the heat of combustion from affecting the measurement or damaging the sensors. To measure the signal from these pressure probes, a four-channel Teledyne-LeCroy WaveRunner 6006Zi Oscilloscope operating at 100 MHZ was used. The oscilloscope took 100ms of pressure data around the ignition event. The data taken from the oscilloscope used LeCroy's enhanced bit depth feature to turn the output of the 8-bit analog to digital converter into 11-bit data. This feature works by taking data at a higher sampling rate and then applying a special filter to the data between sample points that remove outliers and averages the signal to produce data with an increased bit depth. This cuts down on the random noise seen in the data and gives a much greater bit resolution than the hardware is capable of measuring.

The second probes used were an ion probe that tracked the flame front progression. These probes were small ¼ in. hobby spark plugs that had a voltage differential induced across the electrode and the ground. As the flame front of detonation passes over the spark plug, the ionized gas bridges the spark gap and rapidly conducts the voltage potential off the spark plug. This results in a measurable voltage drop across the spark plug that can be used to track the progression of the flame front through the expansion chamber. To capture this voltage drop, two 4-channel Keysight DSOX1204G oscilloscopes were used to take eight simultaneous ion probe measurements in the

expansion chamber. These operated at 100 MHz to allow for the pressure and ion probe data to be synced off the same trigger signal. However, ion probe data could only be taken for 10ms, due to the limited memory of the oscilloscopes. To increase the rate of data ingest during testing, these two oscilloscopes were tethered via USB to the control computer to allow for the data to be directly downloaded.

Lastly, three secondary measurements were taken for each detonation event and recorded using the slower analog-to-digital converter on the NI board. The first of these measurements was an absolute pressure transducer mounted in the exhaust system that measured the back pressure of the detonator. With this transducer being a 4-20 mA sensor, an external shunt resistor was wired into the system and the voltage across this resistor was used to measure the current signal from the sensor and covert this valve into a back pressure. The other two measurements were pressure transducers placed in each reactant supply lines. Two different Omega pressure transducers were used with the fuel side transducer being a 200 psig sensor and the oxidizer sensor a 300 psig sensor. Both sensors were 0-5V with the NI board reading this voltage directly and converting the voltage data into a pressure based on the sensor calibration.

2.4-MFC Calibration

For the reactant flow control, the MFC's were used with a TYLAN 2925 Series 500 SLPM MFC on the oxidizer line and a Teledyne-Hastings HFC-303 100 SLPM MFC. A TYLAN RO-28 control box was used to set the mass flow setting for each MFC. Due to the out-of-date calibration of these MFC's, it was necessary to perform a calibration to ensure accurate mass flow control. This was done with MFC's already integrated into the pneumatic system. The mass flow setting on the control box appeared to be an arbitrary relative value, so it was necessary to calibrate the actual mass flow to this relative valve. The supply line to the pulse detonator for each line was

individually rerouted to a rotameter to measure volume flow. The nitrogen purge gas was used as the calibration gas and was flown through the MFC and out through the rotameter. The temperature and pressure measurements from sensors in the pneumatics system and the volume flow measured by the rotameter were used to calculate the actual mass flow using a modified form of the ideal gas equation in Equation 3. This mass flow value then needs to be converted to SLPM which is defined as the mass of air at standard conditions of 1atm and 0° C flowing at 1 LPM. To correction for the properties of a gas at different pressure and temperature or have a different composition, a gas correction factor (GFC) is calculated using Equation 4 and applied to the actual mass flow value to convert to the standardizer SLPM.

$$\dot{m} = \frac{P\dot{V}}{RT}$$

Equation 3: Volume flow to Mass Flow Conversion

$$\mathrm{GFC} = \sqrt{\frac{\mathrm{SG} * (460 + \mathrm{T_{Fahrenheit}})}{36 * \mathrm{P_{psia}}}}$$

Equation 4: Gas Correction Factor Formula [9]

Performing this calibration, the calibration curves for each MFC are shown in Figure 15 and Figure 16. The calibration lines for both MFC's were mostly linear so a linear curve fit was applied to each curve. This given an equation for setting on the control box for given mass flow in each line. These equations are used to convert the mass flow calculated for each reactant mixture into settings on the MFC control box.

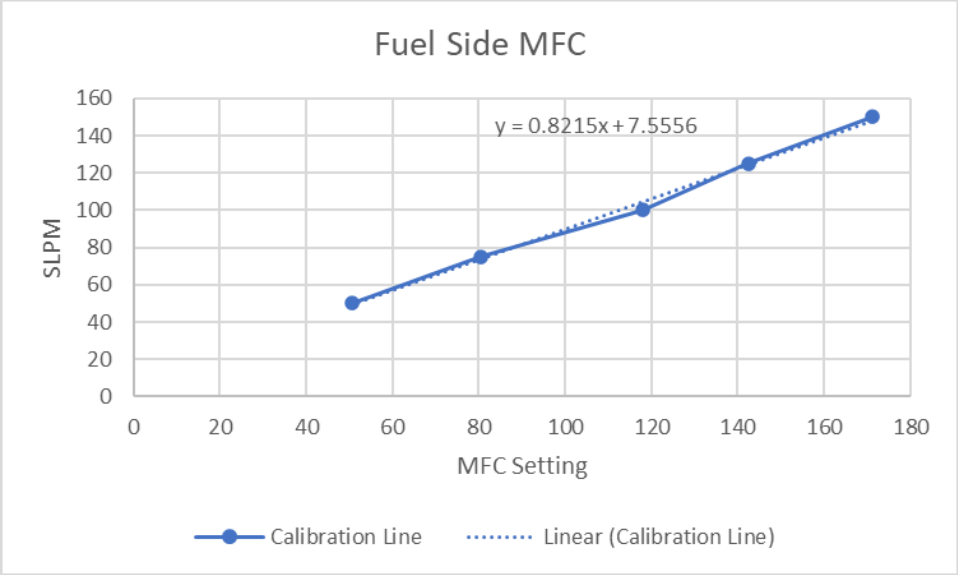

Figure 15: Fuel Side MFC Calibration Curve

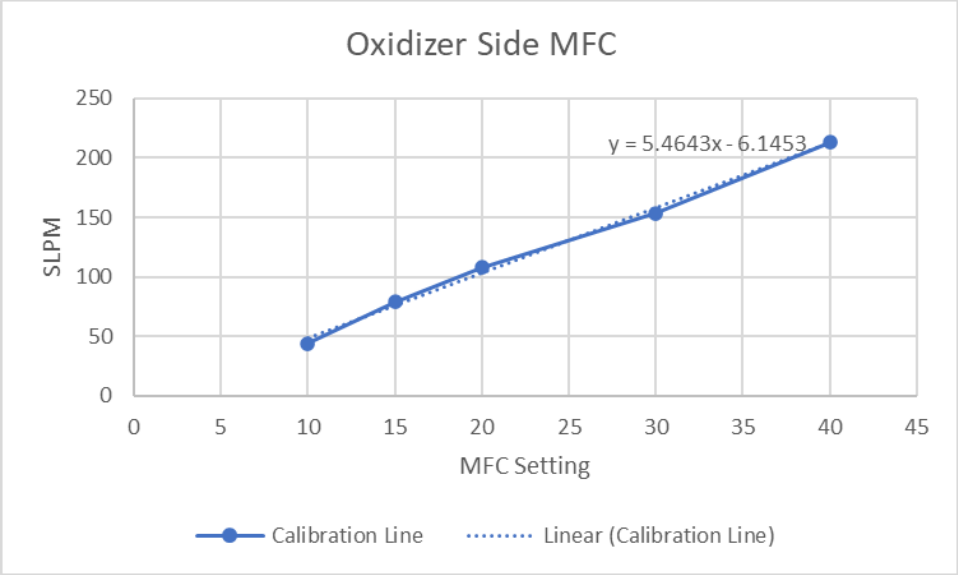

Figure 16: Oxidizer Side MFC Calibration Curve

2.5-Pulse Detonation Head Design

The basic functionality of the pulse detonation head is to initiate a detonation in the controlled reaction mixture. It was necessary to design a detonator that could safely handle a continuous flow of reactants that was desired for the testing concept. This was done by connecting

the reactant flex line coming out of the pneumatic box into a wye junction which allows the reactants to mix together over a short length of 0.5 in diameter pipe. Check valves mounted on both supply lines to prevent the mixing of reactants prior to the detonation head. The reactant mixture flow through the primary flame arrestor shown on the right in Figure 17. This flame arrestor was a previously machined stainless-steel design modeled in Figure 18. This design operates with reactants coming in from the left and passing over an alternating shim stack of .01in shims. This creates several narrow channels for the reactant to flow through with the ignition source mounted on the other side of this shim stack. When ignition occurs on the other side of the flame arrestor, a combination of the small channel size, and the heat transfer into the shims, slows the speed of the flame front in the flame arrestor such that the reactant flow is sufficient to stall the reaction in the flame arrestor and prevent flashback. From previous uses of this flame arrestor, a flow rate of 200 LPM was chosen as a safe operating point with this determined the reactant supply rate of 200 SLPM that was designed for in the pneumatic system.

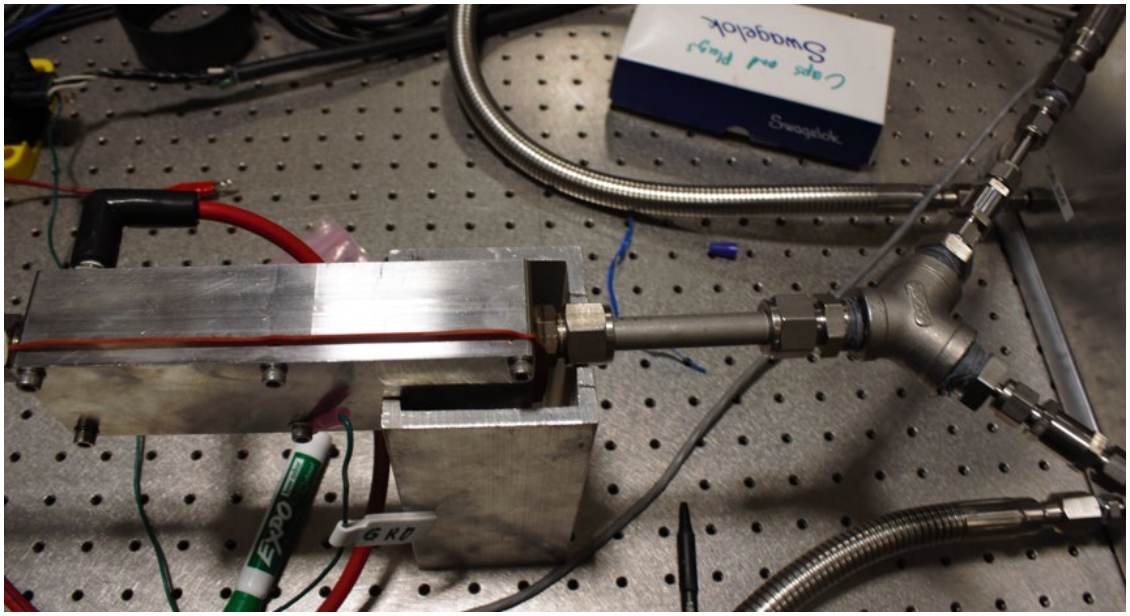

Figure 17: Detonation Head Mixing Section (Right) and Flame Arrestor (Left)

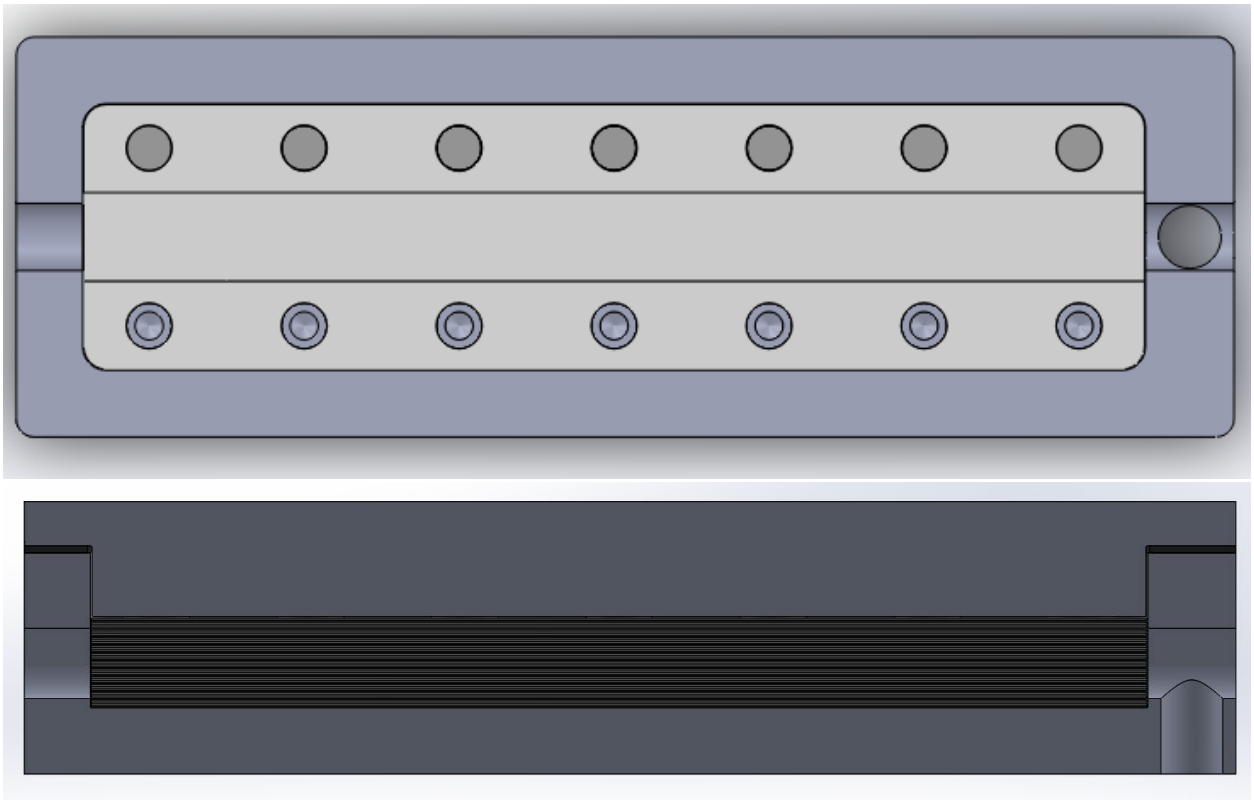

Figure 18: Shim Stack Flame Arrestor Design

For the ignition system, a standard 10mm automotive spark plug was mounted in the flame arrestor, serving as the ignition source. For the ignition coil, it was first attempted to use a simple inductive ignition coil controlled via an external MOSFET to charge and discharge the ignition coil. This system ran into issues with the back EMF voltage produced from the discharge of the coil forcing the relay open and damaging the coil and power supply in the process. To replace this system, an ignition coil with the transistor logic built in was chosen with the AEM 30-2853 "Smart Coil" being used, as shown in Figure 19. This coil is typically powered by a 12V battery but is instead supplied with 12V DC from the electronic box. A separate signal line then controls the triggering of the coil and its dwell time. This is done via a TTL signal which is a pulsed width 5V signal with the falling edge triggering the coil and the width being linked to the dwell time. This TTL signal was produced using the pulse counter output of the NI board, allowing for the parallel triggering of the DAQ system and control over the dwell time. A dwell time of 5 ms was used

during testing, but, when testing with a mixture that was difficult to ignite, the dwell time would be increased to 10ms to achieve a more energetic spark.

Figure 19: AEM Smart Ignition Coil

However, this ignition system does not have enough energy to directly initiate detonation and only initiates deflagration combustion at ignition. This deflagration flame was then allowed to accelerate into a detonation wave. This is done by first passing the detonation through an off-the-shelf 4 in spiral mixer with an ID of 0.494 inches shown in the foreground of Figure 20. The interaction between the spiral geometry and the flame front assists in the DDT process, increasing the flame front acceleration. After this spiral mixer is a 20in long length of 0.402-inch ID tubing also shown in Figure 20. This length of tube allows for the DDT process to be completed and the detonation to stabilize before entering the area expansion section.

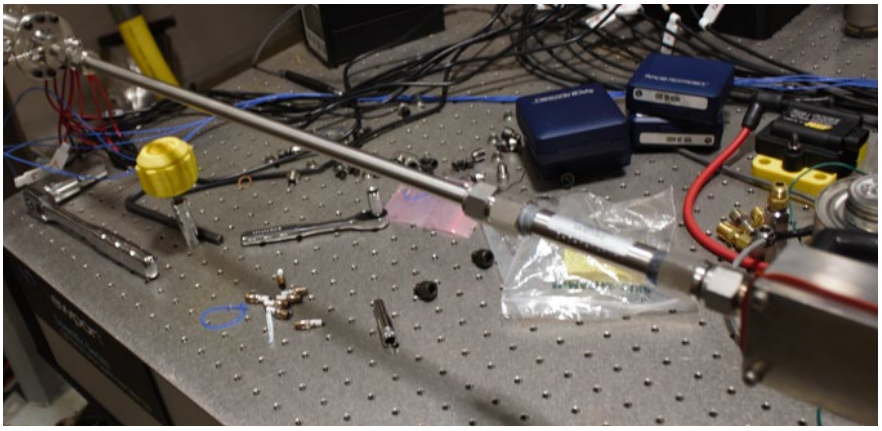

Figure 20: Detonation Head consisting of the spiral mixer (foreground) and the transition tube

2.6-Expanded Area Section

The detonation once initiated must pass through an area expansion section for the amplification phenomenon to occur. Two different area expansion chamber designs were used in this study. The first section was designed and used by Cuppoletti et al. [6] to first study this phenomenon. This design consisted of several 3-inch-long modular sections with a circular area expansion mounted in series. An individual section had mounts for six ion probes spaced at a 0.5-inch interval on one side of the chamber and mounts for three pressure probes on the other side at a 1-inch interval. These sections were designed with different area expansions to explore different expansion geometry. For this study, the 6.25 A/A_o and 25.00 25 A/A_o sections were used and shown in Figure 21. These sections were designed to test multiple chamber lengths, but only the full length of 12-inches was tested in this study. Mounted at either end of the chamber were end plates that transition back to the nominal 0.4 inches ID of the inlet tube. These end plates had additional mounting points for two ion probes and a pressure probe to measure the inlet and outlet conditions.

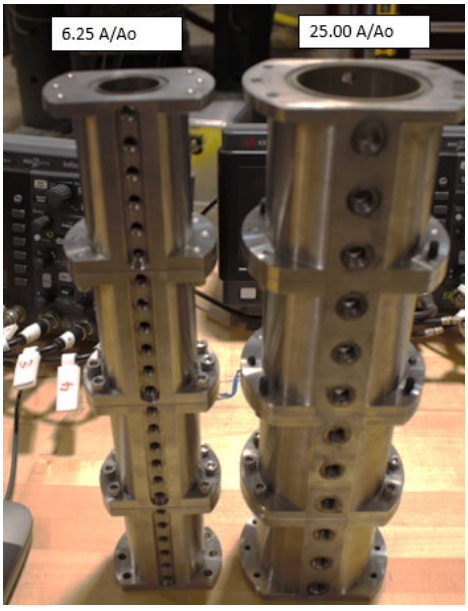

Figure 21: 6.25 A/A_O and 25.00 A/A_O expansion chambers showing ion probe mount points (left) and pressure probe mount points (right)

The second test section was designed to facilitate a more in-depth exploration of the amplification phenomenon. The main goal of the new design was to gain optical access to the amplification phenomenon while having a structure to able withstand extended testing. To facilitate the inclusion of a window, the geometry of the area expansion was changed from circular to square section with the expanded area being a 2-inch square with an area ratio of 31.83 A/A_o. The length of the chamber was increased from 12in to 20in to allow for the amplification phenomenon to further progress before contacting the end wall. The design called for the windows to be made out of optically clear polycarbonate as the alternative to quartz which would have caused a shrapnel hazard during a brittle failure. Polycarbonate fails in a ductile way and cleanly breaks in two during failure. However, polycarbonate is unlikely to hold up for an extended period of time in a high pressure and high temperature environment forcing the window to be replaced after a number of tests. To design around this limitation, a four-piece metal structure was designed for two polycarbonate windows to sit in slots on either side of the expansion chamber with the windows supported on all sides. The windows were designed to be simple rectangles cut to shape to save on the cost of the expendable windows. The structure consisted of a top and bottom piece with mounting points for the ion and pressure probes and two end pieces that were compatible with the end pieces of the original modular expansion chamber. This structure is fastened together via four bolts in a cross pattern at each shoulder joint. An O-ring grove was placed in the window slot to use an O-ring to seal the chamber rather than a sealing compound. This resulted in the design shown in Figure 22 with the top and bottom pieces being 0.375” thick stainless steel and the end pieces being .625” thick stainless steel.

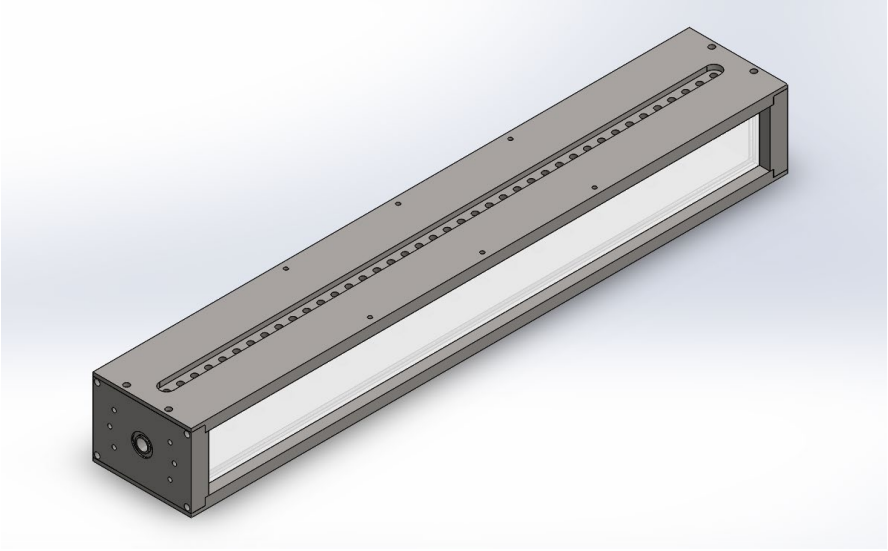

Figure 22: Initial Design of the Optical Test Section

This expansion chamber design however had several design issues that were identified. The first was that the two-sided cross-bolt pattern at the shoulder didn't work. The bolts from the top and bottom had no issues, but the hole for the bolts that come in from the side, called out in Figure 23, could not be tapped due to clearance issues with the shoulder. While this was less than ideal, testing moved forward without these side bolts present. The next issue was more problematic. The top and bottom support pieces were less stiff than expected with the separation in the middle of the chamber being significant from the pressure caused by the O-ring seal. If this separation in the middle was large enough, the windows would likely blow out of the support channel. A temporary solution of clamping the middle of the chamber with two c-clamps was devised. However, this was insufficient to prevent the failure of the chamber during the first test fire. The claps used to support the section were bent by the force of the detonation and the windows were blown out. This results in the top and bottom support pieces being deformed by the detonation shown in Figure 24. This failure was attributed to a lack of stiffness in the top and bottom pieces allowing for the material to deform enough for the windows to blow out and the concentration of the pressure forces involved in the structure causing the stainless steel to yield. This failure

necessitated a remake of the top and bottom pieces, so a redesign of the test section was attempted to address these failure points.

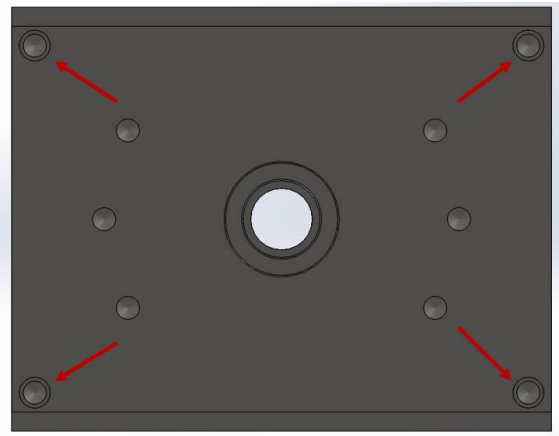

Figure 23: Bolting Problem Points in Original Optical Test Section Design

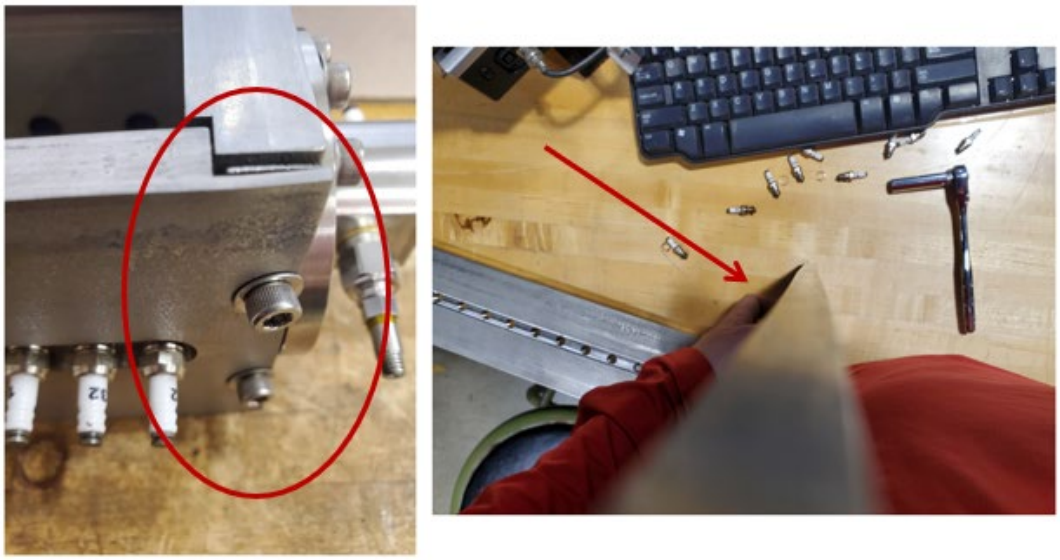

Figure 24: Damage to the First Optically Accessible Expansion Chamber Design

To avoid the further cost and potential safety risk building more unproven detonation test sections, the redesigns were simulated using the finite element analysis (FEA) tools present in the Solidworks CAD software. The main goal of this FEA was a design tool so simulating the dynamics of the detonation wave was too time and computationally intensive, so a simple static pressure load of 750 psi was simulated in the expansion chamber. The bolts were simulated as

simple force couplings using the bolts connection tool in the Solidworks FEA tools. This simulation was not expected to give an accurate prediction of the deformation caused by the detonation pressure wave but does simulate a case that is generally more strenuous on the chamber than the transient load that is expected for a detonation.

To address the separation issues that caused the windows to blow out, a cross bolting solution was devised where bolts would be run through both top and bottom pieces. This would have the unfortunate effect of cutting down on optical access to the expansion chamber as the bolts would block part of the windows. This was deemed necessary as FEA simulations without these bolts showed significant separation in the middle of the top and bottom pieces even when stiffened. The thickness of the top and bottom pieces was increased for the redesign and the material in any remade part was changed from stainless steel to carbon steel. This material change was both for the added strength of the carbon steel and to avoid some of the machining issues present in the original design.

For the test section redesign, the top and bottom pieces were widened to facilitate though bolt holes on each side of the expansion chamber and space at a 1-inch interval. Two different redesigns were explored that kept the same basic structure of the first design but changed various features. The first of these two designs, shown in Figure 25, kept the same windows and end pieces as the original design to be reused but remade the top and bottom pieces to be double the thickness with the probe mount hole and the lateral cross bolts omitted. The second design, shown in Figure 26, remade every piece of the test section. The windows were increased in thickness from .375” to 0.5” with the window support slot being doubled in depth. The metal structure material thickness was increased to a uniform 1” and the cross-bolting pattern was reintroduced with thicker bolts and more clearance. A third radically different design, shown in Figure 27, was also mocked up to

test a bolt-on window concept that would reintroduce full optical access. This model was a simple mockup that lacked any detail that wasn't necessary for the FEA simulation.

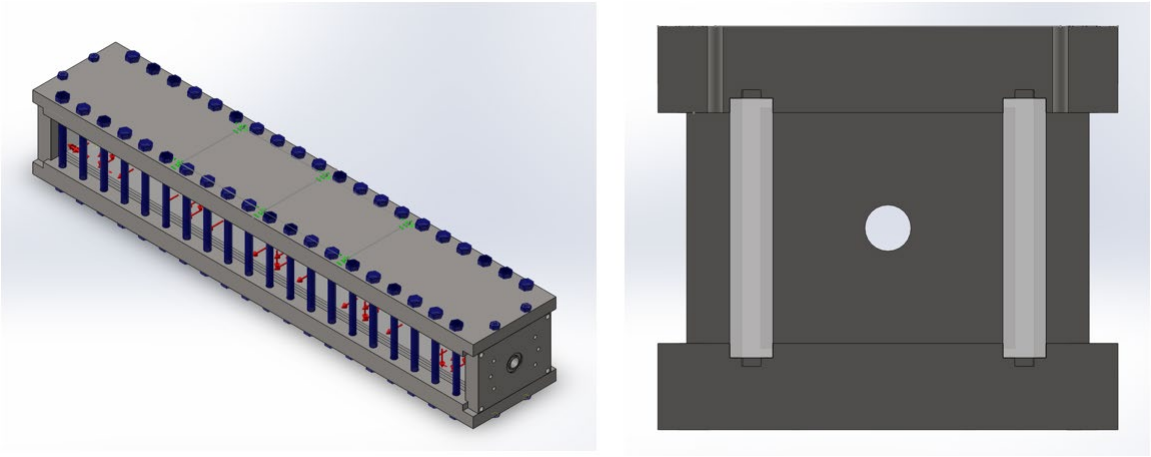

Figure 25: Test Section Redesign 1, remade top and bottom pieces

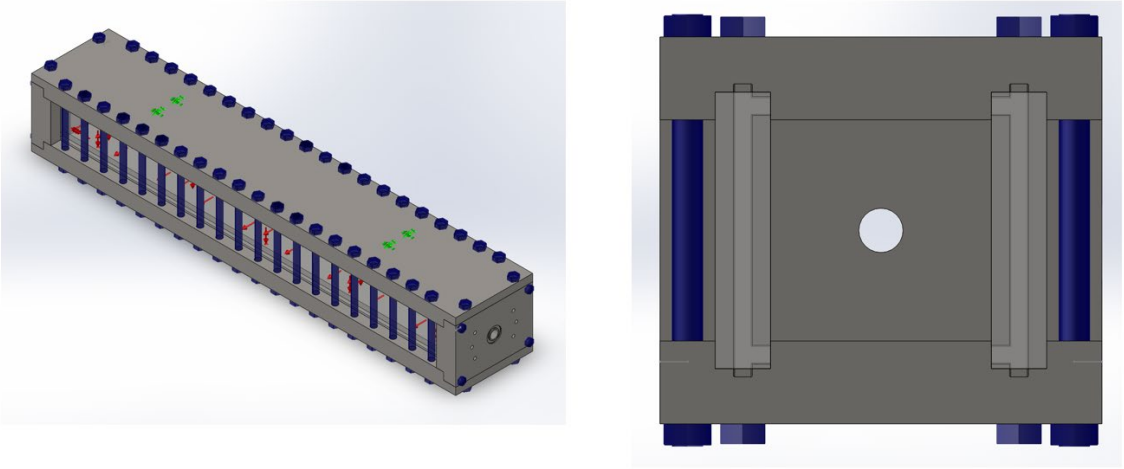

Figure 26: Test Section Redesign 2, complete remake

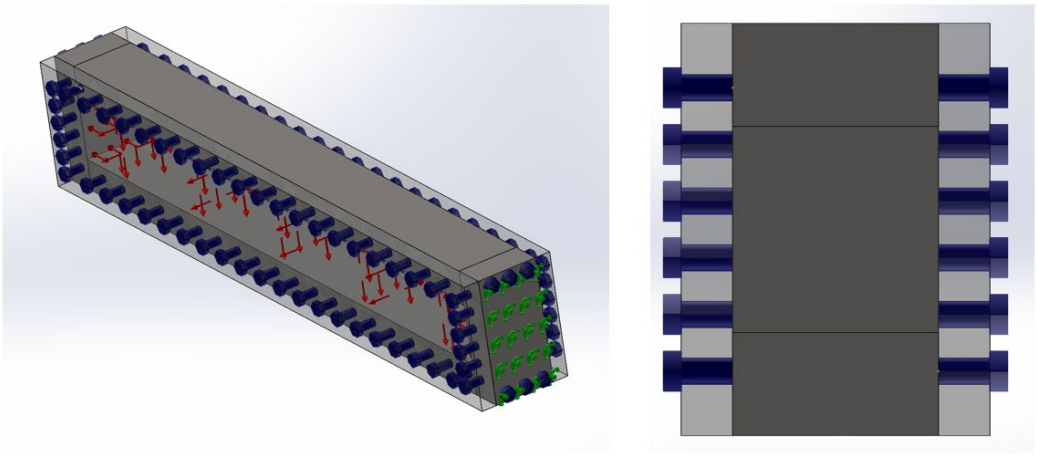

Figure 27: Test Section Redesign 3, Bolt-on windows remake

The results from these three FEA simulations are shown in Appendix 4. The first design simulation showed that the windows would fail at the simulated pressure but showed that the window would yield before blowing out the slot as in the original failure point. The simulation also showed that the bolting pattern for the end pieces was insufficient to keep the ends in place and would separate under load. The second design showed a significant decrease both in the displacement and stress within the windows and neither yielded nor had the windows blown out of the slots. The third design showed only slightly less displacement of the window than in the first redesign with the failure point being at the bolt hole where the stresses concentrated. It is also noted that there was movement in the top and bottom pieces in this design as similar to the end piece in the first design although could be remedied with a further design revision.

With these simulations not being representative of the actual load, a real-world test of the though bolting solution was performed to verify that windows could be prevented from blowing out. It was decided to have the first design quickly machined out of aluminum to serve as the quickest and cheapest way to validate the results of the FEA simulations. When testing with this section, the end would be clamped together using long bar clamps to prevent the ends from

separating as simulated with this setup shown in Figure 28. This test section only was expected to last long enough to test the through bolting solution and take some initial optical data. During testing with this temporary solution, the section was able to contain a few dozen detonations with the movement of the end pieces causing the section to sustain damage, shown in Figure 29. The end clamp support provided by the bar clamps was only partially effective with the solution not preventing damage to the test section but prevented the section from failing entirely even when damaged. This allowed for the test section to hold up long enough for some optical data to be taken as part of this study with a future in-depth optical study using the redesign section.

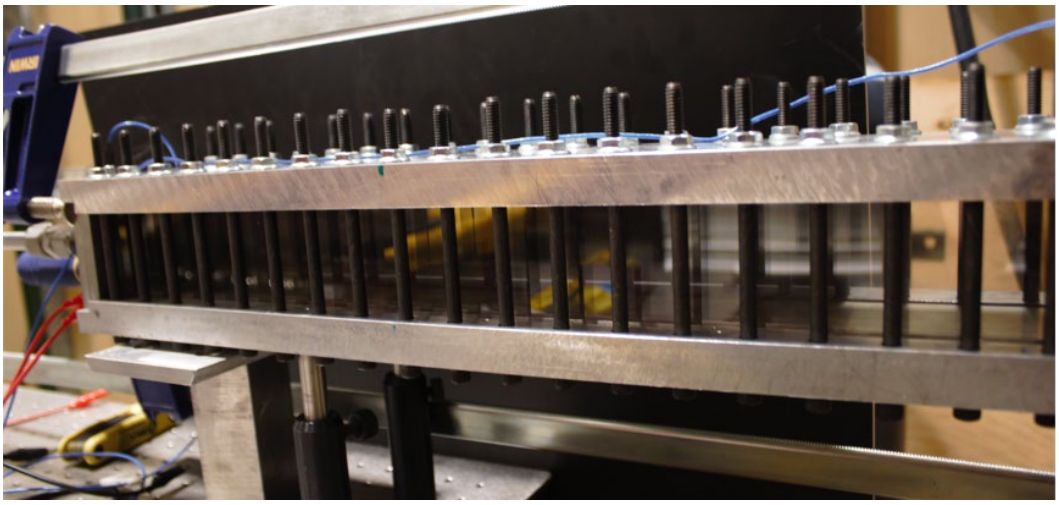

Figure 28: Redesign Optical Test Section with end clamping support

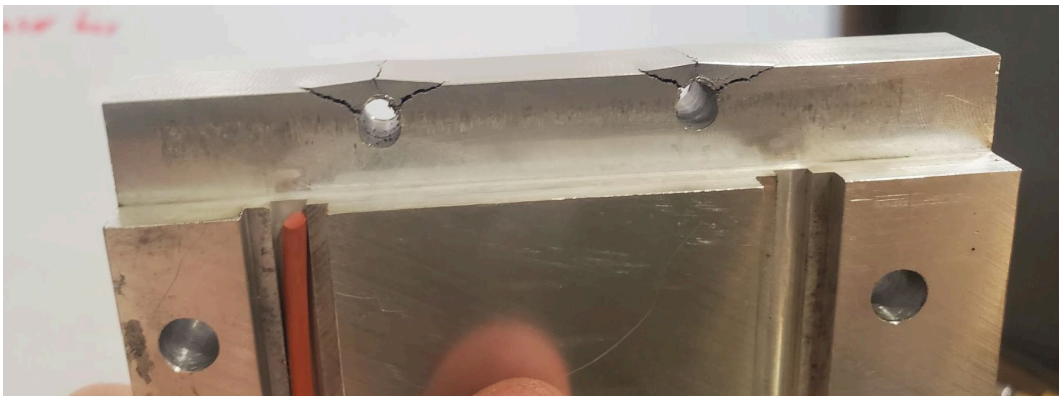

Figure 29: Damage to Redesigned Aluminum Top and Bottom Piece caused by end piece separation

With the result from this testing and the FEA simulation of the three redesigned test sections, it was decided to move forward simultaneously with the first and second redesigns. The second redesign was determined to be the best solution in terms of performance with it having the lowest stress concentration and window displacement in the FEA simulation and the end separation failure point being addressed with the reintroduction of the cross bolting in the end pieces. It was also decided to proceed with the first redesign since this provided a relatively cheap and quick way to manufacture a backup test section by reusing parts from the original design. The move from aluminum to carbon steel in the redesign would fix or at least mitigate the end separation failure point that showed up both in the testing and the FEA simulation of this section.

2.7-Optical Testing

For optical testing, the original plan to take more in-depth optical measurements was forced to be delayed due to scheduling conflicts and the failure of the first optical accessible test section and could not be included in this study. A less quantitative study however was able to be performed using the redesigned optical test section made out of aluminum. This involved using a Photron NOVA SA12 with a 45mm lens focused on the mid-plane of the expansion chamber. This frame side of the camera only allowed for a portion of the expansion chamber to be filmed during a single detonation. As a result, the camera would have to be moved multiple times to film the entirety of the expansion chamber, so the camera was mounted on a rail that fixed its movement to be parallel to the mid-plane to maintain focus on the mid-plane of the expansion chamber. It was identified that upon initial test fires that the luminosity of the detonation event would saturate the sensor in the S12 camera. To prevent this saturation, a neutral density (ND) filter was used to lower the transmission of light to the camera by absorbing a portion of light in the visible light spectrum. The filter that was used for this testing had a measured optical density of 2.0 at 633nm [10]. Using

Equation 5, the transmissibility of light through this filter was calculated to be 1%. This testing was however limited in its quantitative value since this light could not be tied to the emission of a particular reaction step and thus just represent the general chemiluminescence of combustion.

$$Tr = 10^{-\,Optical\ Density}$$

Equation 5: The relationship between the transmissibility of light through an ND filter and its Optical Density [10]

2.8-Exhaust System

For the exhaust system, it was desired to have a completely closed exhaust system as this would both cut down on the noise emission of the detonation as well as contain any hot exhaust product or uncombusted reactant. An exhaust tank shown in Figure 30 was used to allow the detonation to transition to deflagration and to dampen out the pressure impulse from the shockwave produced from the detonation. To quench the detonation reaction, a dilution flow is needed within this tank with this being provided by the Low-Pressure Air System (LPAS) in the Rhodes 300 lab. While air is not ideal as a dilutant due to the presence of oxygen, the amount of airflow that can be provided by the LPAS allows for a higher level of dilution to compensate for this. For the dilution system, the LPAS air is routed through a needle valve at the bottom of the exhaust tank with the exhaust being expelled through a stainless-steel line flex hose located at the top of the tank.

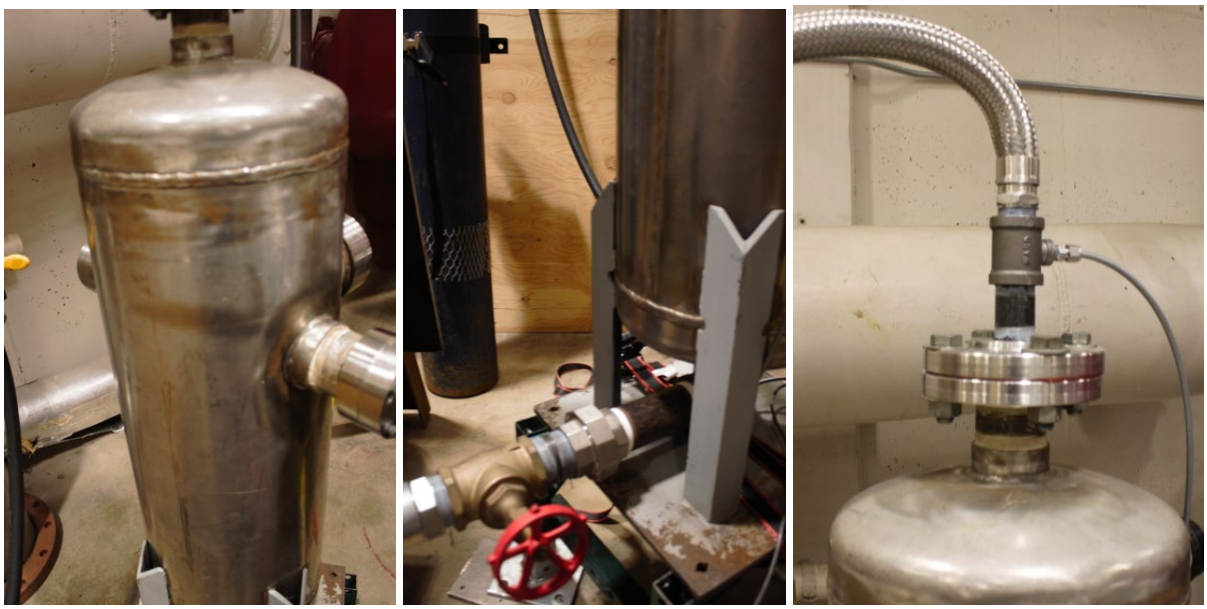

Figure 30: Exhaust Containment Tank with the Dilution Air Line shown in the middle and the stainless-steel line to the vacuum injector on the left

This system could just be driven by the pressure supplied by the LPAS, but this would result in a back pressure in the detonator being greater than ambient. This is problematic since a detonation already amplifies the initial pressure of the reaction mixture with a CJ detonation wave resulting in an approximately 40 times pressure amplification and the amplification phenomenon amplifying this even further. This means that a small increase in the back pressure results in a bigger change in the peak detonation pressure that could potentially blow out part of the system. As a result, the dilution flow would be pulled through the exhaust tank by a vacuum injector placed at the facility exhaust rather than letting the pressure of the LPAS drive the dilution flow. A Norgen NVDF-75 variable vacuum injector was selected for this purpose and shown in Figure 31. This injector works as a venturi pump such that when you supply a driving air flow to the ejector vacuum flow is forced through the injector until back pressure is stabilized. To achieve the highest dilution flow at any given condition, the NVDF-75 was driven at its maximum driving flow of 2700 SLPM of air which gives the maximum performance tradeoff between vacuum flow and

vacuum pressure as shown in Figure 32 [11]. To achieve the dilution flow, the needle valve is open such that the vacuum pressure is balanced with the dilution flow being pulled through the system. This allows for the back pressure of the pulse detonator to be controlled down to sub-ambient conditions while maintaining the high dilution flow at a given back pressure. However, it was found that the system was difficult to balance a particular back pressure due to this balance changing when flowing reactants and the needle valve for the dilution flow lacking fine adjustment. This resulted in the back pressure of the detonation having a ±0.5 psi variation on the desired back pressure setting during testing. This venturi injector system has the added benefit of further diluting the exhaust products before they are ejected into the facility exhaust system in the Rhodes 300 lab. This allows for the vacuum tank to be operated closer to the flammability limit of a given reaction since the vacuum system was built to tolerate a degree of combustion and heat release while diluting the exhaust gas to a further safe point before it was exhausted into the environment.

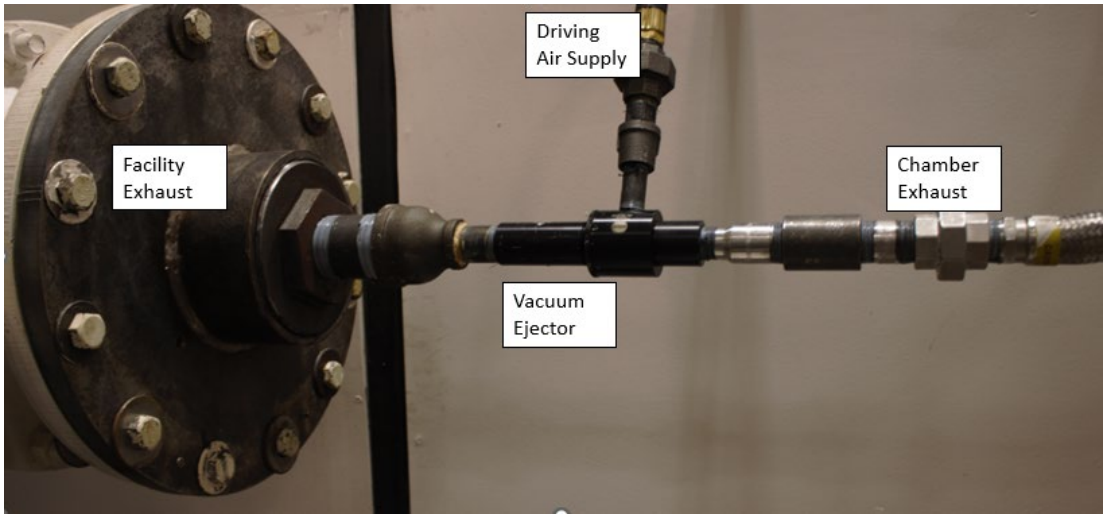

Figure 31: Exhaust Ejection System

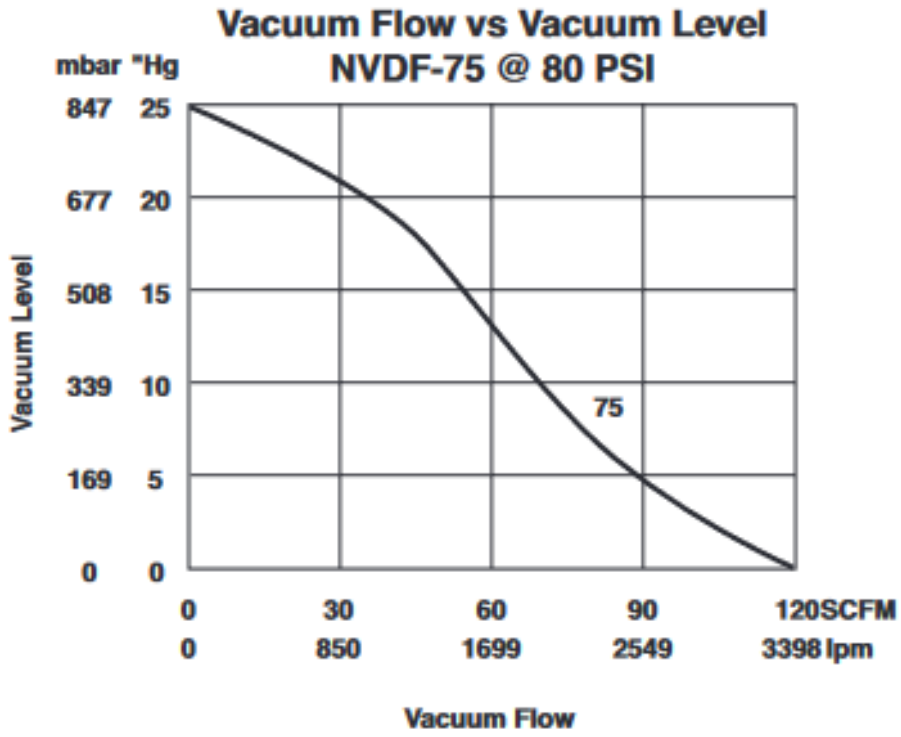

Figure 32: Norgen NVDF-75 Vacuum flow vs. Vacuum Level at max flow rate condition [11]

3-Experimental Methodology

3.1-Fuel-Oxidizer Mixture and Equivalence Ratios

$$CH_4 + 2O_2 \rightarrow 2H_2O + CO_2$$
$$CH_4 + 4N_2O \rightarrow 2H_2O + 2CO_2$$
$$C_2H_4 + 3O_2 \rightarrow 2H_2O + 2CO_2$$
$$C_2H_4 + 6N_2O \rightarrow 2H_2O + 2CO_2$$
$$C_3H_8 + 5O_2 \rightarrow 4H_2O + 3CO_2$$
$$C_3H_8 + 10N_2O \rightarrow 4H_2O + 2CO_2$$

Equation 6: Global Chemical Reaction for each fuel-oxidizer combination

For the control over λ required for this study, it was desired to use different fuel-oxidizer mixtures to observe the effect of large changes in λ and use changes in Φ to explore the effect of smaller changes in λ. It was decided to work with CH_4, C_2H_4, and C_3H_8 as the fuel gases due to a combination of ease of use with gaseous fuels, the availability of said fuel, and the expected

variation in λ between reactions. For the oxidizers, the two gases chosen were O_2 and N_2O. An O_2 reaction would be a good comparison point to the expected operation of a detonation ignitor but is a difficult gas to safely work with. N_2O is easier to work with and offers a similar λ behavior to O_2 but still has some distinct chemical kinetic differences. This results in six unique fuel oxidizer combinations with the global reactions for each shown in Equation 6. For the Φ's being tested, a Φ sweep from 0.5 to 2.0 was desired at an interval of 0.1 for the lean side of the range and an interval of 0.2 for the rich side.

3.1.1-Additional test conditions

Given the effect of area expansion ratio on the amplification behavior shown in Cuppoletti et al. [6], it was also necessary to characterize the effect of area expansion ratio with respect to change in λ. This will serve to validate the results in the previous work and help establish a correlation between λ, the area expansion ratio, and the amplification behavior. To this end, two different area ratio sections were tested, 6.25 A/A_o and 25.00 A/A_o. The 6.25 A/A_o test section served as the primary test section for this study with focused testing conducted using the larger 25.00 A/A_o.

With the variable back pressure afforded by the exhaust system, it was also desired to test the effect of sub-ambient back pressure on the detonation phenomenon. This sub-ambient back pressure testing was desired as it would be closer to the expected operating condition of a detonation ignitor. This also introduced a third way of changing λ with decreasing back pressure being shown to increase λ [8]. This change in λ occurs without significantly changing the reaction which allows for a clear look at changes in λ isolated from a change in reaction behavior. Operation at a lower pressure in the vacuum system does however limit the amount of fuel gas that the system can safely handle due to a lower dilution air flow. Due to this, testing at the sub-ambient

pressure of 0.5 atm was limited to Φ=0.5 to 1.0 as the fuel-rich conditions had a smaller safety margin. Lastly, this sub-atmospheric testing was only conducted with the 6.25 A/A_o test chamber. This results in the initially planned test matrix found in Table 1.

Test Group	A/Ao	Fuel Gas	Oxidizer	Back Pressure	Phi Sweep
1	6.25	CH4	N2O	1 atm	.5 to 2.0
2	6.25	C2H4	N2O	1 atm	.5 to 2.0
3	6.25	C3H8	N2O	1 atm	.5 to 2.0
4	6.25	CH4	O2	1 atm	.5 to 2.0
5	6.25	C2H4	O2	1 atm	.5 to 2.0
6	6.25	C3H8	O2	1 atm	.5 to 2.0
7	6.25	CH4	N2O	0.5 atm	.5 to 1.0
8	6.25	C2H4	N2O	0.5 atm	.5 to 1.0
9	6.25	C3H8	N2O	0.5 atm	.5 to 1.0
10	6.25	CH4	O2	0.5 atm	.5 to 1.0
11	6.25	C2H4	O2	0.5 atm	.5 to 1.0
12	6.25	C3H8	O2	0.5 atm	.5 to 1.0
13	25	CH4	N2O	1 atm	.5 to 2.0
14	25	C2H4	N2O	1 atm	.5 to 2.0
15	25	C3H8	N2O	1 atm	.5 to 2.0
16	25	CH4	O2	1 atm	.5 to 2.0
17	25	C2H4	O2	1 atm	.5 to 2.0
18	25	C3H8	O2	1 atm	.5 to 2.0

Table 1: Initially Planned Test Matrix

3.2-Mass Flow Calculations

With the test conditions set, the mass flow required for each condition was calculated. This begins with the stoichiometric mole ratios for each fuel-oxidizer pair that were calculated from the global combustion reactions shown in Equation 6. From this stoichiometric mole fraction, the relationship found in Equation 7 was used to calculate the mole ratio of the non-stoichiometric conditions. From this actual mole ratio, the mole fraction for each reactant was calculated using Equation 8. This mole fraction was then used to calculate the mass fraction of the reactants using Equation 9.

$$\frac{n_{ox}}{n_{fuel\ actual}} = \frac{\frac{n_{ox}}{n_{fuel\ Stoich}}}{\Phi}$$

Equation 7: Mole ratio Φ correction formula

$$X_i = \frac{n_i}{\sum n_{reactants}}$$

Equation 8: Mole fraction formula

$$Y_i = \frac{MW_i * X_i}{\sum MW_{reactants} * X_{reactants}}$$

Equation 9: Mass fraction formula

$$\dot{m}_i = \dot{V}_{rectants} * Y_i * \frac{P * R_u}{T * \sum MW_{reactants} * X_{reactants}}$$

Equation 10: Reactant Mass Flow Calculation

The pneumatic system was designed to deliver 200 LPM of reactants to the pulse detonator at a temperature of 300 K and 1 atm. Using Equation 10 and the desired volume flow point, the mass flow for each individual reactant was calculated. This mass flow was then converted into SLPM with Table 2 showing the necessary reactant flow for each expected test condition. Using the linear calibration curve produced for each MFC's, these SLPM valves are then converted into settings for the MFC control box shown in Table 3. These mass flow conditions will be used for both the atmospheric and sub-atmospheric since the ratio of reactants is the same for both conditions.

	C2H4- N2O		C2H4- O2		CH4- N2O		CH4- O2		C3H8- N2O		C3H8- O2	
Phi	Oxidizer (SLPM)	Fuel (SLPM)	Oxidizer (SLPM)	Fuel (SLPM)	Oxidizer (SLPM)	Fuel (SLPM)	Oxidizer (SLPM)	Fuel (SLPM)	Oxidizer (SLPM)	Fuel (SLPM)	Oxidizer (SLPM)	Fuel (SLPM)
2.0	49.7	149.1	79.5	119.3	66.3	132.5	99.4	99.4	33.1	165.6	56.8	142.0
1.8	45.9	152.9	74.5	124.2	61.7	137.1	94.2	104.6	30.3	168.4	52.6	146.2
1.6	41.8	156.9	69.1	129.6	56.8	142.0	88.3	110.4	27.4	171.4	48.2	150.6
1.4	37.6	161.2	63.2	135.5	51.5	147.2	81.8	116.9	24.4	174.4	43.5	155.3
1.2	33.1	165.6	56.8	142.0	45.9	152.9	74.5	124.2	21.3	177.5	38.5	160.3
1.0	28.4	170.4	49.7	149.1	39.8	159.0	66.3	132.5	18.1	180.7	33.1	165.6
0.9	25.9	172.8	45.9	152.9	36.5	162.3	61.7	137.1	16.4	182.4	30.3	168.4
0.8	23.4	175.4	41.8	156.9	33.1	165.6	56.8	142.0	14.7	184.0	27.4	171.4
0.7	20.8	178.0	37.6	161.2	29.6	169.2	51.5	147.2	13.0	185.8	24.4	174.4
0.6	18.1	180.7	33.1	165.6	25.9	172.8	45.9	152.9	11.3	187.5	21.3	177.5
0.5	15.3	183.5	28.4	170.4	22.1	176.7	39.8	159.0	9.5	189.3	18.1	180.7

Table 2: Calculated SLPM for Fuel and Oxidizer with respect to each fuel-oxidizer pair and Φ

	C2H4- N2O		C2H4- O2		CH4- N2O		CH4- O2		C3H8- N2O		C3H8- O2	
Phi	Oxidizer	Fuel	Oxidizer	Fuel	Oxidizer	Fuel	Oxidizer	Fuel	Oxidizer	Fuel	Oxidizer	Fuel
2.0	48.4	28.4	72.9	23	62	25.4	89.2	19.3	34.8	31.4	54.2	27.1
1.8	45.2	29.1	68.8	23.9	58.2	26.2	84.9	20.3	32.5	31.9	50.8	27.9
1.6	41.9	29.8	64.4	24.8	54.2	27.1	80.1	21.3	30.1	32.4	47.1	28.7
1.4	38.4	30.6	59.5	25.9	49.9	28.1	74.8	22.5	27.6	33	43.3	29.5
1.2	34.8	31.4	54.2	27.1	45.2	29.1	68.8	23.9	25.1	33.6	39.2	30.4
1.0	30.9	32.3	48.4	28.4	40.2	30.2	62	25.4	22.4	34.2	34.8	31.4
0.9	28.9	32.7	45.2	29.1	37.5	30.8	58.2	26.2	21	34.5	32.5	31.9
0.8	26.8	33.2	41.9	29.8	34.8	31.4	54.2	27.1	19.7	34.8	30.1	32.4
0.7	24.6	33.7	38.4	30.6	31.9	32.1	49.9	28.1	18.2	35.1	27.6	33
0.6	22.4	34.2	34.8	31.4	28.9	32.7	45.2	29.1	16.8	35.4	25.1	33.6
0.5	20.1	34.7	30.9	32.3	25.7	33.4	40.2	30.2	15.3	35.7	22.4	34.2

Table 3: MFC Control Box setting with respect to Fuel-Oxidizer Setting and Φ

3.3-Safety Calculations

With the mass flow calculation calculated, safety calculations for the exhaust system were performed to confirm all test cases will remain within safety limits. Due to the use of air as the diluent, two different dilution regimes form in the vacuum system. The first is the fuel-lean and stoichiometric conditions where air acts as a simple diluent and the second is the fuel-rich conditions where the excess fuel can react with the oxygen in the air changing the stoichiometry of the reaction. The actual air-fuel ratio was calculated in the vacuum chamber using an estimated dilution flow of 3100 LPM [11] and Equation 11. To calculate the Φ in the vacuum system, a new stoichiometric air-fuel ratio is first calculated. For the simple dilution regime, the Φ is calculated using Equation 12. The fuel volume percentage in the vacuum system is calculated after this to compare to the flammability limit of the reaction to determine if the reaction will quench. This was done using Equation 14 to calculate the molecular weight of the gas in the vacuum system and then using Equation 15 to calculate the fuel volume percent.

$$\frac{A}{F}_{actual} = \frac{\dot{m}_{fuel} + \dot{V}_{dilution} * \rho_{air}}{\dot{m}_{fuel}}$$

Equation 11: Actual Air-Fuel Ratio Formula for the Vacuum System

$$\frac{A}{F}_{stoich} = \frac{MW_{ox}}{MW_{fuel}} * \frac{n_{ox}}{n_{fuel}}$$

Equation 12:Stoichomeric Air-Fuel for the Simple Dilution Regime

$$\Phi = \frac{\frac{A}{F}_{actual}}{\frac{A}{F}_{stoich}}$$

Equation 13: Equivalence Ratio Formula

$$MW_{mixture} = \frac{\sum \dot{m}_i * MW_i}{\sum \dot{m}_i}$$

Equation 14: Molecular Weight Calculation

$$Fuel\ Volume\ \% = \frac{\dot{m}_{fuel}}{\sum \dot{m}_i} * \frac{MW_{mixture}}{MW_{fuel}} * 100\%$$

Equation 15: Percent Fuel Volume in Mixture

For the air reactive regime, Equation 14 and Equation 15 are still used to calculate the percent fuel volume, and Equation 11 is used to calculate the actual air-fuel ratio, but the stoichiometric air-fuel ratio has changed. Equation 16 shows the new unbalance global reaction for the reactive dilution flow with *a* being determined by Equation 7. *c* and *d* are determined by the global reactions found in Equations 6. *b* is then calculated using Equation 17. From these mole fractions, Equation 18 can be used to calculate the new reactive dilution flow stoichiometric air-fuel ratio. Equation 13 is then used to calculate the resultant equivalence ratio in the vacuum system in the reactive dilution flow regime. These calculations result in the safety graphs shown in Appendix 5. This shows that for the range of test conditions, the dilution flow should be sufficient to quench the reaction in the vacuum chamber. The higher Φ's for the C_2H_4-O_2 and C_3H_8-O_2 reactions are however close to the flammability limit in air of 2.75% and 2.1% respectively [12]. With these flammability limits being measured in air and the diluted mixture

having additional oxidizer present, it was a point of concern that these margins may not be sufficient. However, it was found that the real performance of the Norgen vacuum ejector was greater than that found in technical specifications. With this providing an increased safety margin, testing moved forward while monitoring the temperature in the vacuum system to avoid dangerous levels of heat release.

$$CH_4 + aO_2 + b(0.21\ O_2\ + 0.79\ N_2) \rightarrow cH_2O + dCO_2 + .79b\ N_2$$

$$CH_4 + aN_2O + b(0.21\ O_2\ + 0.79\ N_2) \rightarrow cH_2O + dCO_2 + .79b\ N_2$$

$$C_2H_4 + aO_2 + b(0.21\ O_2\ + 0.79\ N_2) \rightarrow cH_2O + dCO_2 + .79b\ N_2$$

$$C_2H_4 + aN_2O + b(0.21\ O_2\ + 0.79\ N_2) \rightarrow cH_2O + dCO_2 + .79b\ N_2$$

$$C_3H_8 + aO_2 + b(0.21\ O_2\ + 0.79\ N_2) \rightarrow cH_2O + dCO_2 + .79b\ N_2$$

$$C_3H_8 + aN_2O + b(0.21\ O_2\ + 0.79\ N_2) \rightarrow cH_2O + dCO_2 + .79b\ N_2$$

Equation 16: Modified Global reaction with reactive dilution air

$$b = \frac{c + 2d - a}{.21}$$

$$b = \frac{c + 2d - \frac{a}{2}}{.21}$$

Equation 17:Stoichiometric Dilution Mole Fraction Calculation for O_2 (top) and N_2O (bottom)

$$\frac{A}{F}_{Stoich} = \frac{a * MW_{ox} + b * MW_{air}}{MW_{Fuel}}$$

Equation 18: Stoichiometric Air Fuel Ratio Formula for Reactive Dilution Flow

With safety limits established in the vacuum system, the safety limit for the exhaust gas being ejected to ambient were calculated. It was decided to treat the ejector air supplied as a simple diluent for the final exhaust case since it was the second exhaust dilution step and Φ should be less than 1.0. The actual air-fuel ratio calculation for this step included the flow driving the vacuum ejector which was estimated to be 2500 LPM [11] and used Equation 19. Then Equation 12 and Equation 13 were used to calculate the Φ in the ejection exhaust. After this, the same calculation

for percent fuel volume was performed using Equation 14 and Equation 15. This results in the safety plots shown in Appendix 6. It was desired for the precent fuel volume at this final dilution step to be below 25% of the flammability limit. This however was not achieved with most of the lean reactions being under this safety limit but most of the rich reactions being over this safety limit. This is however mitigated by the overperformance of the ejection system leading to additional safety margin and the exhaust flowing into the facility exhaust system in the Rhodes 300 Lab which provides an unknown amount of additional dilution.

$$\frac{A}{F}_{actual} = \frac{\dot{m}_{fuel} + (\dot{V}_{dilution} + \dot{V}_{ejection}) * \rho_{air}}{\dot{m}_{fuel}}$$

Equation 19: Ejection Actual Air-Fuel Ratio Calculation

3.4-Testing Procedure

For the testing procedure, it was required to start up the pneumatic system. This is first done by letting the MFC's warm up and reach a stable temperature. The MFC's are then to a fuel-lean condition for the reaction being tested. The exhaust system is then started and balanced on a desired back pressure and the manual valves in the pneumatic system are opened. After this, the gas supply bottles are opened, and PLC pneumatic control is enabled. The prime program on the PLC is then triggered via the LabView interface with the ignition coil disarmed to done to prevent accidental discharge of the coil. With the system now primed and the indicator light on the front of the electrical box a solid red, the ignition coil can be armed, and the system is ready to fire.

When testing, a limitation in the number of data channels in the DAQ system made simultaneous measurements of the entire expansion chamber and inlet and outlet conditions impossible. As a result, testing could only be conducted using six ion probe points and three pressure probe points at a time with the remaining channels used to measure the inlet pressure and wave speed as shown in Figure 33. This inlet condition data was then used to normalize for the

variation in inlet detonation and served as a common sync point in the data so that data could be stitched together for the entire section from discontinuous tests. This forced testing to be repeated five times to capture the full extent of the expansion chamber and outlet. Referencing Figure 34, this was done by measuring at the probe points within four zones in the test section that corresponded to the four modular pieces that made up the test section. The outlet pressure and wave speed conditions as well as the ion probe points 1-6, 2-1, 2-6, and 3-1 were measured as a fifth test series to capture the outlet conditions and fill in the gaps in ion probe data between the zones.

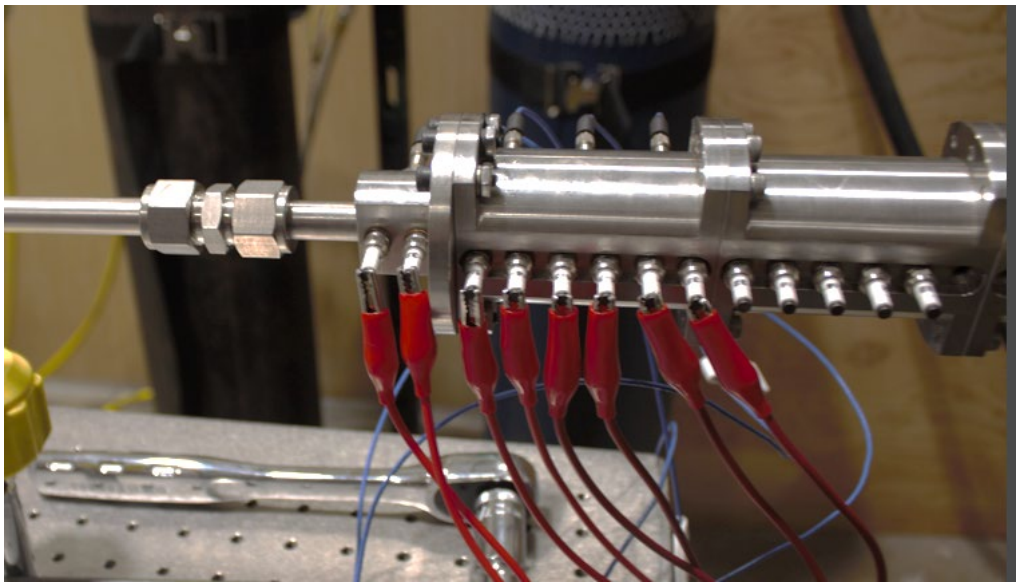

Figure 33: Ion and Pressure Probes mount in Zone 1

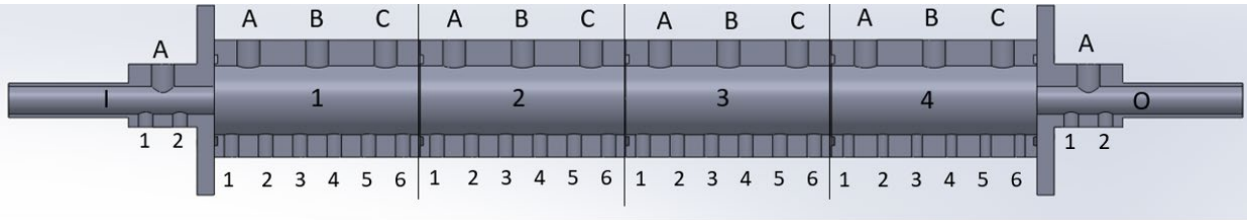

Figure 34: Modular Test Section Probe Point Convention

Testing would be conducted by mounting the probes in the desired measurement zone with the exhaust system turned off and the ignition coil disarmed for safety. The exhaust system is

restarted, the ignition coil armed and the MFC control box set to the point corresponding to a given reaction and Φ using Table 3. The system is then fired using the LabVIEW program and the probe measurements in the chamber are captured and saved by the DAQ system. The DAQ system is then reset, and the test is repeated for a total of three detonations for each Φ and measurement zone. After these three detonations, MFC settings on the MFC control box are changed to a new Φ and the testing is repeated for another three detonations. This is repeated until the full Φ sweep is complete in the measurement zone and then the probes are moved to the next zone. Testing is then repeated until the test section is fully mapped for all Φ for a given condition. After which the system is purged using the prime/purge button in the LabVIEW interface after which the pneumatic system is disabled. The system is then changed over to the test new condition, involving either a replacement of fuel, oxidizer or the test section.

3.5-Issues During Test

The testing plan originally envisaged in Table 1 quickly ran into issues. The first of these was unreliable ignition at a Φ of 1.2 for the CH_4-N_2O reaction with an increase in dwell time of the ignition coil to 10ms mitigating this to an extent. Above a Φ of 1.2, ignition was rarely achieved with the DDT process being incomplete in the inlet tube even when combustion did occur. As a result, testing using CH_4-N_2O was limited from a Φ of 0.5 to 1.2. The next issue was with the C_2H_4-N_2O reaction which operated the closest to the flammability limit of any of the fuels mixed with N_2O. During testing at fuel-rich conditions with these reactants, a worrying amount of heat release was observed in the vacuum system. As a result, testing using C_2H_4-N_2O was limited to a Φ of 1.4 and below to avoid the highest heat release cases.

The next issue was a breakdown in the LPAS that occurred in the middle of the test campaign. Due to this air system providing the dilution air for the exhaust system, this shutdown

testing until the system was repaired months later. This necessitated a reevaluation of the original testing plan as the timetable for the larger project, that this study was part of, changed. This resulted in the decision to cut the O_2 testing entirely. This was justified since the λ behavior of N_2O was expected to be similar enough to O_2 that the O_2 testing would not provide significantly more insight into the relationship between the amplification phenomenon and λ. This combined with the issues with consistent ignition and exhaust system heat release resulted in the final test matrix shown in Table 4.

Test Group	A/Ao	Fuel Gas	Oxidizer	Back Pressure	Phi Sweep
1	6.25	CH4	N2O	1 atm	.5 to 1.2
2	6.25	C2H4	N2O	1 atm	.5 to 1.4
3	6.25	C3H8	N2O	1 atm	.5 to 2.0
7	6.25	CH4	N2O	0.5 atm	.5 to 1.0
8	6.25	C2H4	N2O	0.5 atm	.5 to 1.0
9	6.25	C3H8	N2O	0.5 atm	.5 to 1.0
13	25	CH4	N2O	1 atm	.5 to 1.2
14	25	C2H4	N2O	1 atm	.5 to 1.4
15	25	C3H8	N2O	1 atm	.5 to 2.0

Table 4: Revised Test Matrix

3.6-Experimental Limitations

It was found that the experiment had limitations in its ability to fully and repeatably capture the amplification process. The first limitations were the ability of the DAQ system to resolve the detonation event. Looking at the time resolution, the 100Mhz sampling rate of the DAQ system gives 10ns between the samples. With the distance between the ion probe being 0.5 inches and the pressure probes of one inch, this gives the ability to measure events traveling between probes up to 1,270,000 m/s for the ion probes and 2,540,000 m/s for pressure probes. This is 3 to 4 orders of magnitude greater than the expected CJ wave speed which was approximated to be between 2000 m/s and 2500 m/s. For an event to pass over a sensor, it was estimated that the event would need to travel greater than 635,000 m/s to be missed entirely by the DAQ system. With this again being

3 orders of magnitude greater than the CJ wave speed, the detonation event would likely be time resolved by the DAQ system.

For the spatial resolution of the detonation event, the thickness of the shockwave and flame front is expected to be extremely thin. The diaphragm on the pressure probe however is 0.218" with this limiting the ability of the pressure probes to differentiate between a detonation that is decoupled less than 0.218" and a coupled detonation wave. When the detonation is closely decoupled the flame front and the shockwave pass over the sensor's diaphragm simultaneously resulting in the pressure reading being a combination of the two waves rather than distinct events. For the spatial resolution of the ion probes, the ion probes don't directly measure the wave speed of the detonation but instead tracks the time of flight between sensors. This means that only the average wave speed between sensors can be calculated from the ion probe data. The actual progression between the sensors is not observed by this probing method and remains unknown. These two limitations lead to the DAQ system being unable to completely spatial resolve the detonation event, especially the smaller scale events such as the exact point of reinitiation.

The next limitation was the design of the expansion chamber. The first limitation in the expansion chamber was the necessary spacing of the probes leaving gaps in the expansion chamber where events could occur without being captured. This likely causes the exact reinitiation event to be missed by the pressure probes with only the immediately pre-reinitiation and post-reinitiation behaviors being captured. The next limitation was the probe mounting locations on the side wall of the expansion chamber only allowing the propagation of the detonation event to be measured at the side wall and tracked in the axial direction. This means that the behavior of the amplification event in the middle of the chamber could only be speculated based on what was measured at the side walls. The inherently axial measurements of the probes also result in cosine error due to the

three-dimensional behavior of the detonation and the one-dimensional measurement. This is especially seen in the wave speed measurements near the inlet when the detonation behavior is mostly three-dimensional.

The last issue was mainly observed during the testing phase and was a lack of repeatability observed around the reinitiation event. This is theorized to be caused by the detonation amplification phenomenon being sensitive to the conditions at the point of area expansion, especially to the state of the shock mechanism that causes detonation cell formation. Slight variations in this shock mechanism are likely amplified by the area ratio expansion causing the reinitiation event to move in the expansion chamber. This is supported by a larger deviation at the point of reinitiation in 25.00 A/A_o results compared to the 6.25 A/A_o results. This led to cases where the reinitiation is captured during one test and then not captured in the next, despite no test conditions being changed. This is compounded by other factors such as a change in the heat transfer rate in a cold system versus a warm system, variation in the exact back pressure of the detonation, and changes in the exact Φ of reaction due to the limited accuracy of the MFC's. All of this manifests in the results as a large standard deviation seen at the reinitiation point of the detonation with the standard deviation decreasing further away from this point.

4-Results

4.1-Data Processing

The data recorded by the DAQ system was a voltage potential in of the sensors with this data need to be processed to be turned this voltage into quantitative values. This post-processing was done in batches that correspond to individual Φ sweeps using two MATLAB scripts, one for the pressure probe data and the other for the ion probe data.

Starting with the pressure probe script which operates by batch processing data from a Φ sweep in each zone of the test section. This script imports the four data files corresponding to the four pressure probes used during testing into MATLAB. Then the calibration factor for each probe provided by the manufacturer was applied to the voltage data converting it into a pressure measurement. The script then looks for the first point for which each pressure trace crosses a threshold valve corresponding to detonation first passing the probe with this threshold varying depending on the test condition. The peak of this first pressure spike was calculated using the maximum value of the two thousand data points or 20 μs of data after this threshold was crossed. This was done since the peak of the first pressure wave of the main point of interest and it was found in certain cases that the reflection of the detonation had a stronger pressure impulse that the initial way. The script then offsets the time axis such that when the inlet pressure impulse first crosses the threshold, t=0. This was done to sync the pressure traces for discontinuous tests to a single relatively repeatable event. This produces a plot similar to that shown in Figure 35. While the data has had some noise removed by the preprocessing algorithm on the LeCroy oscilloscope, the data remains very noisy and difficult to read in places, especially around the first pressure spike for each trace. As a result, it was desired to filter this data further to produce clearer pressure trace graphs.

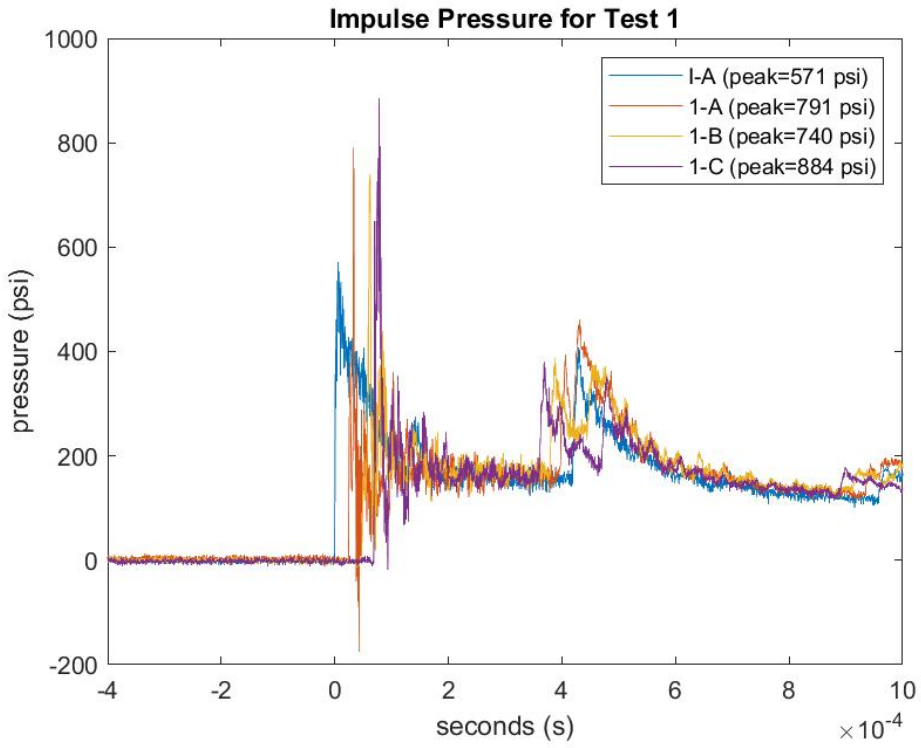

Figure 35: Raw Data Pressure Plot for the C_2H_4 and N_2O reaction in the 6.25 A/A_o section for Zone 1 at 1 atm and a Φ= 0.5

In Cuppoletti et al. [6], a third-order Savitzky–Golay (SG) filter with a frame width of 1001 was applied to their pressure traces to address this noise issue. This however causes issues around the peaks of the pressure traces where the SG filter would change the overall shape of the pressure spike as well as significantly decreasing the maximum pressure seen in this. To solve this problem, a variable width SG filter was added to the MATLAB script. This operated in tandem with the threshold crossing code with the pressure data being split into three sections. The first section corresponds to every data point before the threshold is crossed. The next section corresponding to the 2000 data points or 20 µs of data after the threshold is crossed, corresponding to the first pressure wave. The third section corresponds to all the data points after the first pressure wave has passed. A coarse third-order SG filter with a frame width of 1001 was applied to the first and third sections using the in-built *sgolayfilt* function in MATLAB. A second finer third-order SG filter was applied to the second section with a frame width of 51. This smaller frame width was chosen

such that the majority of the peak structure is maintained while still smoothing out some of the noise in the data. The filtered data produced for the second section is then used to calculate a new maximum pressure peak for the first wave with it being found that this peak was at most a few psi lower than the unfiltered peak. The three sections are then stitched back together and plotted to produce a graph similar to that shown in Figure 36.

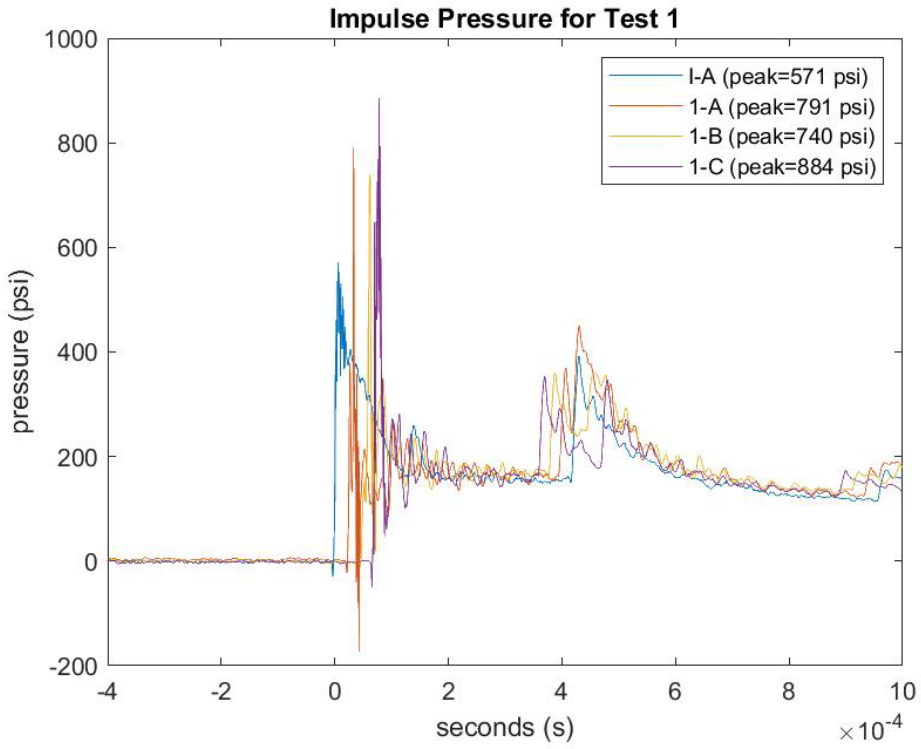

Figure 36: Variable Width SG Filter Pressure Plot for the C_2H_4 and N_2O reaction in the 6.25 A/Ao section for Zone 1 at 1 atm and a Φ= 0.5

With the filtered pressure traced produced for each test zone for any given test case, these traces are combined into a single graph similar to that shown in Figure 37, using the inlet detonation wave as the point of reference. The repeatability of the detonation progression was found to be varied resulting in cases where the progression of the pressure wave between the zone appeared inconsistent with the global progression. The worst cases of this desync show a detonation propagating backward between zone before continuing with a more normal

progression. As explained in the Experimental Limitation section, this is due to the detonation amplification process being sensitive to the changes in the inlet condition. This results in a small variation in the inlet condition being magnified during the amplification process resulting in noticeable changes in detonation progression between tests under the same condition. With the three detonations being measured for each test condition and zone, the data in the off-sync zone is replaced with data from another test that had a closer sync to the rest of the zones to develop a pressure trace graph with a more consistent progression. While this doesn't represent a true progression of the detonation, it does give a better idea of how the detonation progresses with respect to time compared to only looking at individual pressure traces or certain aspects of the pressure traces such as peak amplitude.

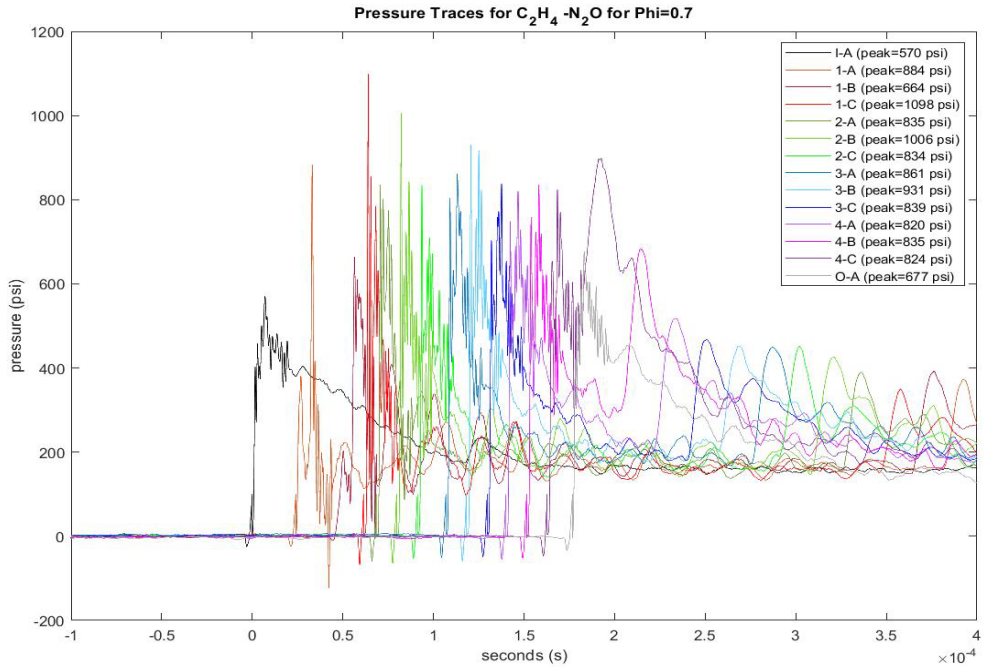

Figure 37: Variable Width SG Filter Pressure Plot for the C_2H_4 and N_2O reaction in the full 6.25 A/A_o section at 1 atm and a Φ= 0.7

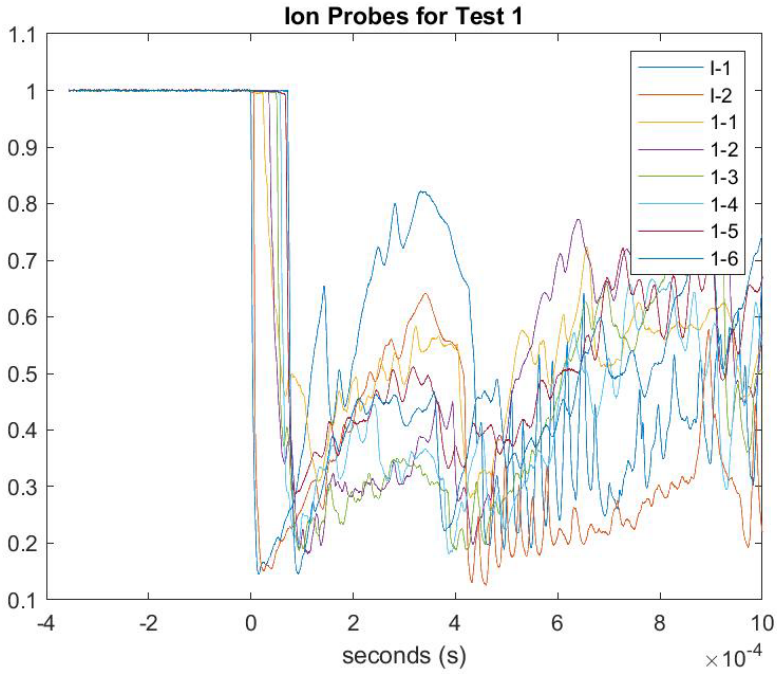

Figure 38: Flame Front Progression Plot for the C_2H_4 and N_2O reaction in the 6.25 A/A_o section for Zone 1 at 1 atm and a Φ= 0.5

For the ion probe measurements, the raw voltage data doesn't have a simple calibration factor with the timing of the voltage drop representing the measurement. The MATLAB script for the ion probe data first imports the data from the output files of the two Keysight oscilloscopes and normalizes for the steady-state voltage found by averaging the first 1000 data points. This gives the data in percent of steady-steady voltage to account for slight variations in the steady-state voltage seen between each probe. A third-order SG filter with a frame width of 101 is applied to this data with the main purpose of removing noise in the signal caused by the ignition coil firing. The MATLAB script then finds the first point for each probe where the percentage of steady-state voltage drops below a threshold value of 98%. This is used to indicate when the ionized gas from the flame front is passing over the ion probe. This gives a time of flight for the flame front in the expansion chamber. With each of these ion probes being mounted at a fixed interval of 0.5 inches, the average wave speed between the ion probes is calculated using Equation 20. This is done for the inlet probes and then for the probes located in the particular data zone. To graph the time

progression of the flame front, the same time axis offsetting technique used for the pressure traces is used with t=0 corresponding to the first inlet probe crossing the threshold. This result in a graph similar to that shown in Figure 38. For the overall time progression of the flame front, it was found that syncing using the inlet detonation wave was even less reliable than the pressure trace with most graphs produced showing a clear discontinuity when transitioning between zones. This results in a graph, similar to that shown in Figure 39, showing a rough progression of the flame front through the entire section.

$$\text{Wave Speed} = \frac{\Delta x_{probes}}{t_{trigger\ i+1} - t_{trigger\ i}}$$

Equation 20: Wave Speed Calculation between Two Ion Probes using the threshold trigger times

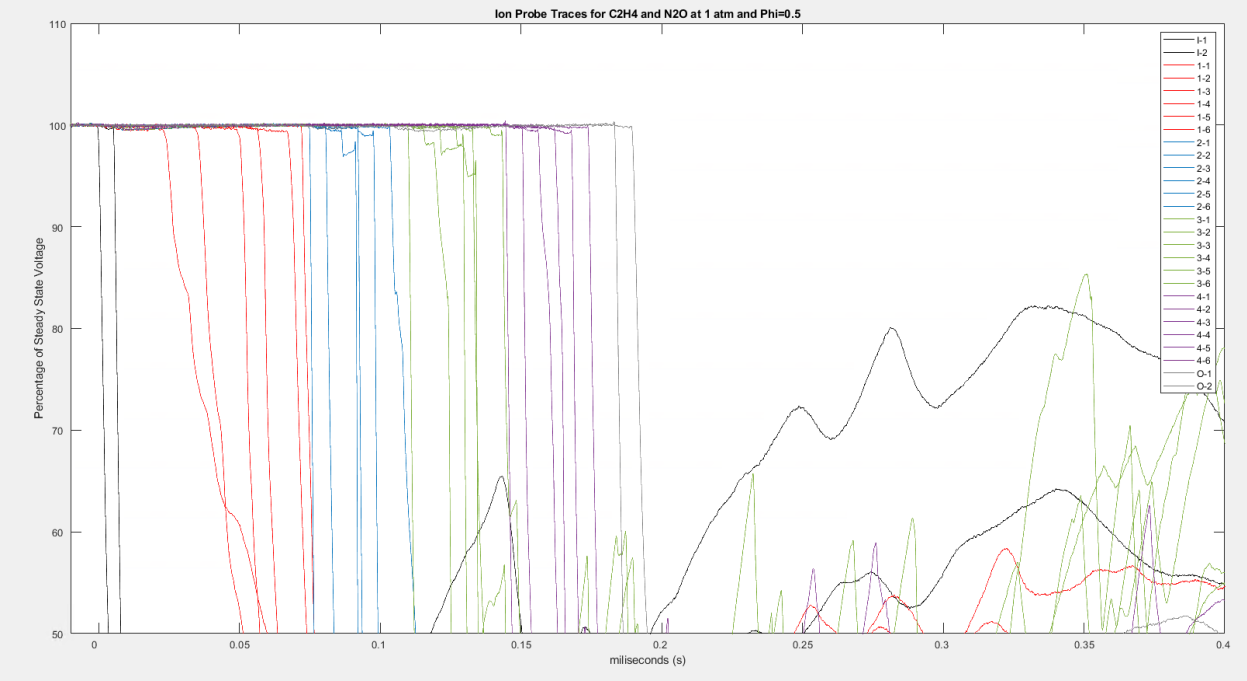

Figure 39: Flame Front Progression Plot for the C_2H_4 and N_2O reaction in the full 6.25 A/Ao section at 1 atm and a Φ= 0.5

4.2-6.25 A/A_o Results

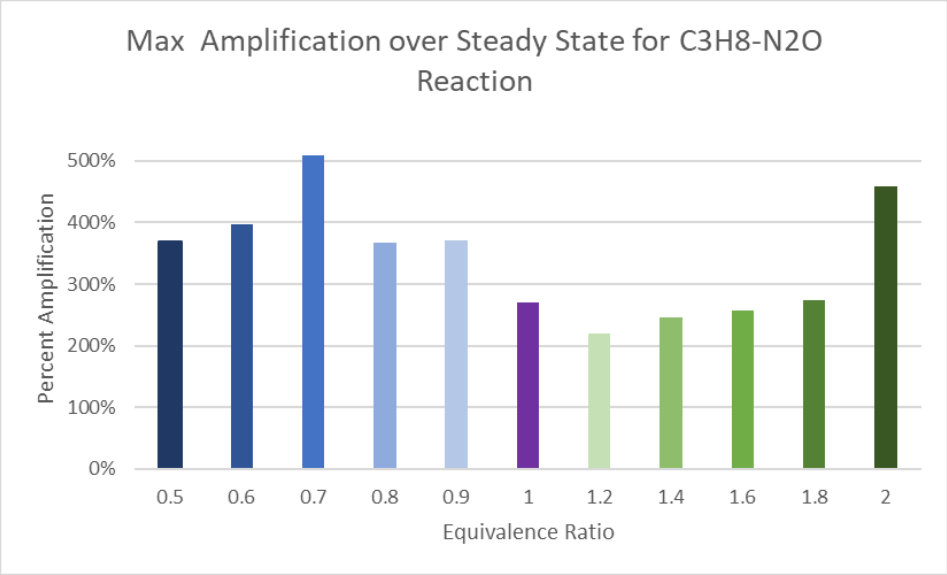

Figure 40: Max Pressure Amplification in Expansion Chamber vs. Φ for the C_3H_8-N_2O reaction at 1atm

To capture the general changes in behavior between the reaction mixtures and Φ's, the maximum pressure impulse at each probe point was plotted versus to the axial distance in the expansion chamber. To correct for the variation observed in the incoming detonation wave, the peak pressure impulse for each probe point was normalized using the peak pressure impulse measured in the incoming detonation wave to give a percent amplification over the incoming pressure impulse using Equation 21. The plot produced does not provide insight into the time progression of the detonation just the general behavior of the pressure impulse with respect to position in the expansion chamber. With the C_3H_8 and N_2O reaction being the point of comparison to the previous work by Cuppoletti et al. [6] and Chin et al. [7], this reaction will serve as the baseline case with Figure 41 showing the results for the 6.25 A/A_o atmospheric testing. The denotations are observed to show two distinct behaviors at this test case. One behavior shows a large spike in the pressure impulse that quickly is attenuated, and the other behavior displays a steadier amplification where the detonation doesn't have a spike in pressure impulse but is still

generally amplified. Both these behaviors were observed to attenuate down to broadly similar conditions at the outlet. The transition between these two cases is more clearly shown in Figure 40. When Φ=1.0 to 1.8, a lower peak amplification of 2 to 3 times steady-state impulse is observed with this corresponding to the steadier amplification behavior. The detonation at the other Φ's shows a larger peak amplification of 3 to 5 times the steady-state pressure impulse that corresponds to the spike amplification behavior. The location of this peak amplification for either behavior was observed in the axial position of 6 to 9 cm with this location not appearing to be a function of behavior.

$$\%\ Pressure\ Amplifcation_i = \frac{\max(P_i)}{\max(P_{inlet})} * 100\%$$

Equation 21:Precent Pressure Amplification Calculation

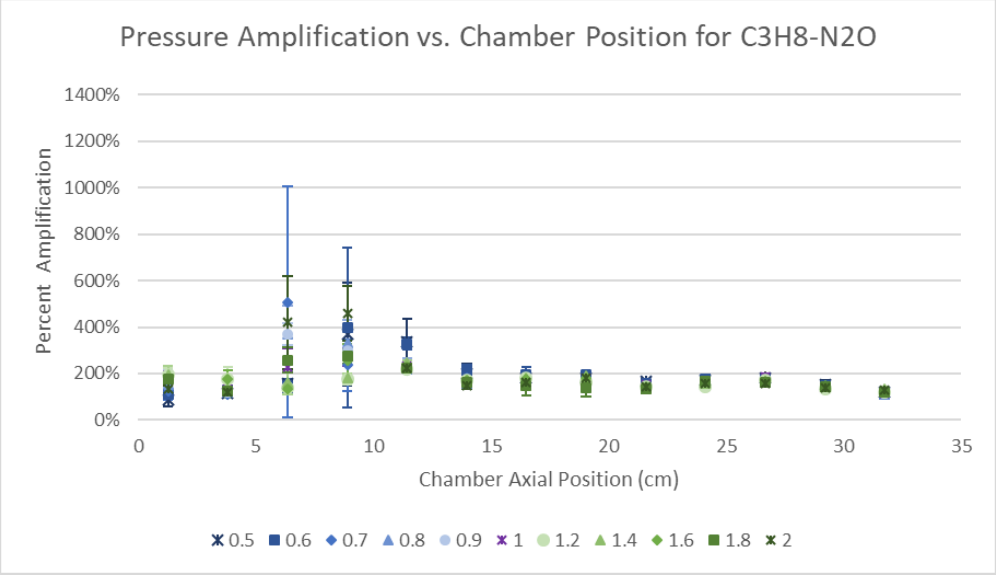

Figure 41: Pressure Amplification vs. Expansion Chamber Position for the 6.25 A/A_o section and the C_3H_8-N_2O reaction at 1atm

Graphing the pressure trace for cases displaying the two distinct behaviors produced in Figure 42 and Figure 43 for the steady amplification and spike amplification behavior respectively. The initial decoupling behavior of the detonation appears to be similar for both behaviors with a

noticeable double spike in the pressure trace forming. The first spike is caused by the initial decoupled shock wave and the second by a localized reinitiation caused by the side wall of the chamber. As the detonation accelerates to recouple the time between these two spikes is observed to decrease. When these two spikes merge into a single pressure spike, the detonation is then theorized to be close to recoupling or has already recoupled with the localized reinitiation, and the initial pressure spike being no longer distinguishable in the pressure traces. This reinitiation event is not fully resolved by the pressure sensors due to the size of the sensor diaphragm at 0.212" which can cause the flame front and pressure wave to be measured simultaneously while still being decoupled. This is the point where the two detonation behaviors diverge, with a large spike present at this reinitiation point in the spike amplification case. This spike was then observed to rapidly attenuates back down to a lower but still amplified state leaving the expansion chamber at approximately 120% of the incoming pressure impulse. For the steady amplification behavior, the peak amplification still occurs at this reinitiation point but lacks the dramatic spike in impulse pressure seen in the spike amplification case. It is also noted that the rapid attenuation of the detonation is not observed for this case and instead a slower attenuation is observed. The detonation is also noted to have a similarly amplified state at the outlet to that seen in the spike amplification behavior.

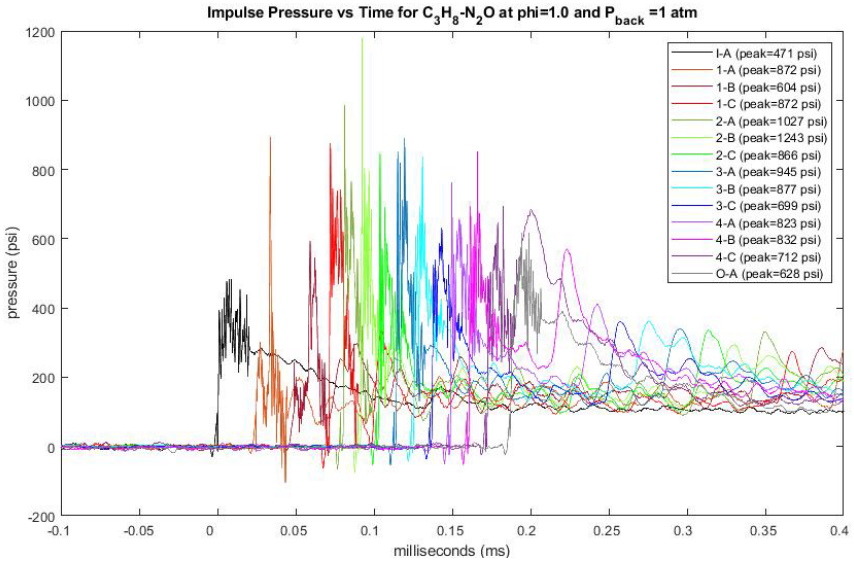

Figure 42: Pressure Traces for the Steady Amplification Behavior for a C_3H_8-N_2O reaction at Φ=1.0 and a back pressure of 1 atm in the 6.25 A/A_o section

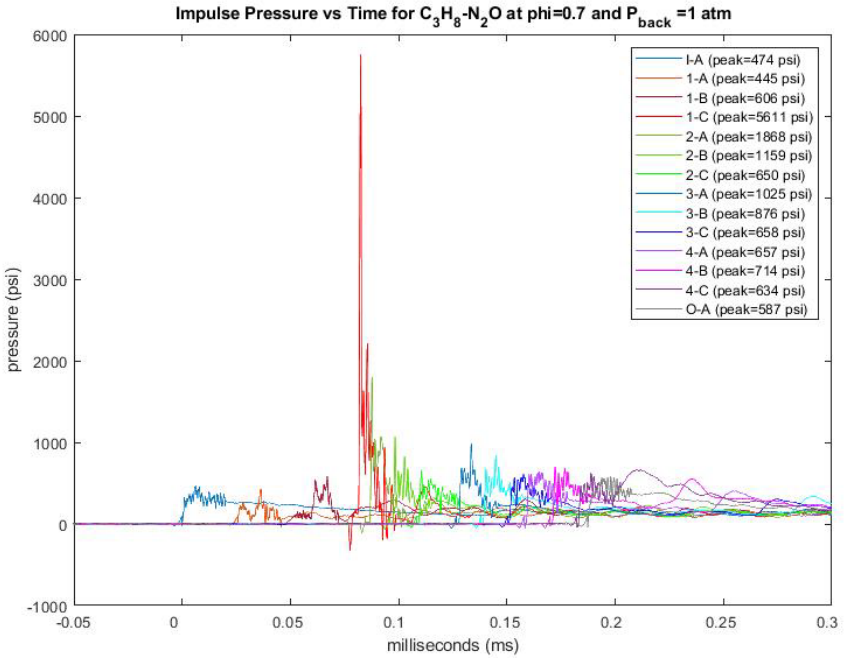

Figure 43: Pressure Traces for the Spike Amplification Behavior for a C_3H_8-N_2O reaction at Φ=0.7 and a back pressure of 1 atm in the 6.25 A/A_o section

For the wave speed results, the wave speed was similarly normalized to the inlet condition measurement using Equation 22 to account for a similar variation seen in the inlet wave speed. This results in the graph shown in Figure 40. This graph confirms the initial decoupling of the detonation with the wave speed initially being lower than the steady-state inlet condition. The

detonation then appears to accelerate to recouple at an axial position of 4 to 5 cm. This acceleration overdrives the flame front past the inlet wave speed, which is theorized to be the rapidly recoupling of the detonation. Comparing Figure 41 and Figure 44, this rapidly recoupling is followed by a brief deceleration of the flame front to a non-overdriven state with this corresponding to the peak pressure amplification point seen in the pressure traces. This flame speed then attenuates back down to a lower than inlet speed that is similar regardless of the Φ.

$$\%\, Wave\ Speed Amplification_i = \frac{Wave\ Speed_i}{Wave\ Speed_{inlet}} * 100\%$$

Equation 22: Percent Wave Speed Amplification Calculation

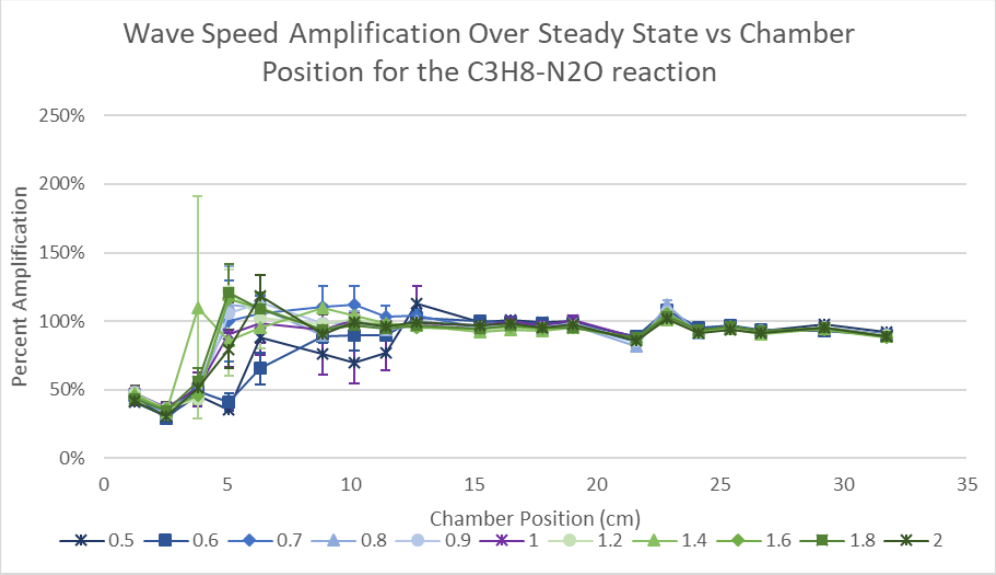

Figure 44: Wave speed Amplification vs. Expansion Chamber Position for the 6.25 A/A_o section and the C_3H_8-N_2O reaction at 1atm

Moving on to the C_2H_4-N_2O reaction, the normalized pressure results are shown in Figure 45. This shows a much more consistent amplification behavior than that found in the C_3H_8-N_2O cases at the same conditions with the peak amplification occurring consistently at an axial position of 6 cm. Peak amplification for every Φ tested fell in the 2 to 2.5 times the steady-state pressure impulse range with this maximum pressure slowly attenuating after this peak. This matches the steady amplification behavior observed in the rich C_3H_8-N_2O cases at the same condition. Looking

at the wave speed plot shown in Figure 46, a similar decoupling behavior to that seen in the C_3H_8-N_2O cases is observed. When the flame front accelerates to recouple with the shockwave, it is seen to do so over a longer distance compared to the baseline C_3H_8-N_2O reaction. This could be a result of detonation not being as decoupled as in the C_3H_8-N_2O cases, so the flame front doesn't have a large slug of shocked but uncombusted gas to drive the rapid recouple event. This could also explain why the detonations with C_2H_4-N_2O were generally less amplified than the C_3H_8-N_2O detonations that exhibit the same steady amplification behavior. This is theorized to be the result of a smaller slug of uncombusted gas creating less thrust impulse at reinitiation which reduced the peak amplification of the detonation pressure.

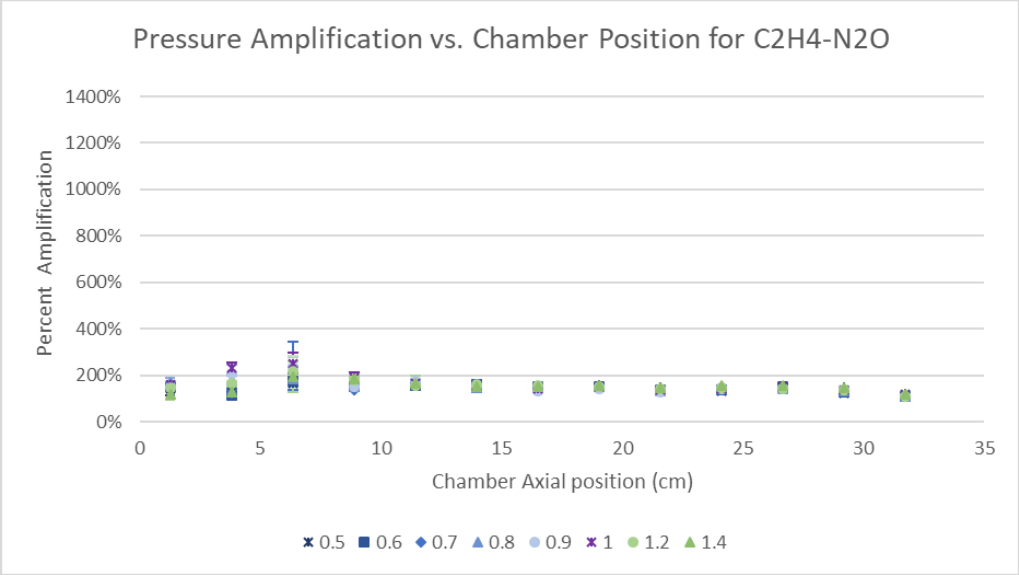

Figure 45:Pressure Amplification vs. Expansion Chamber Position for the 6.25 A/A_o section and the C_2H_4-N_2O reaction at 1atm

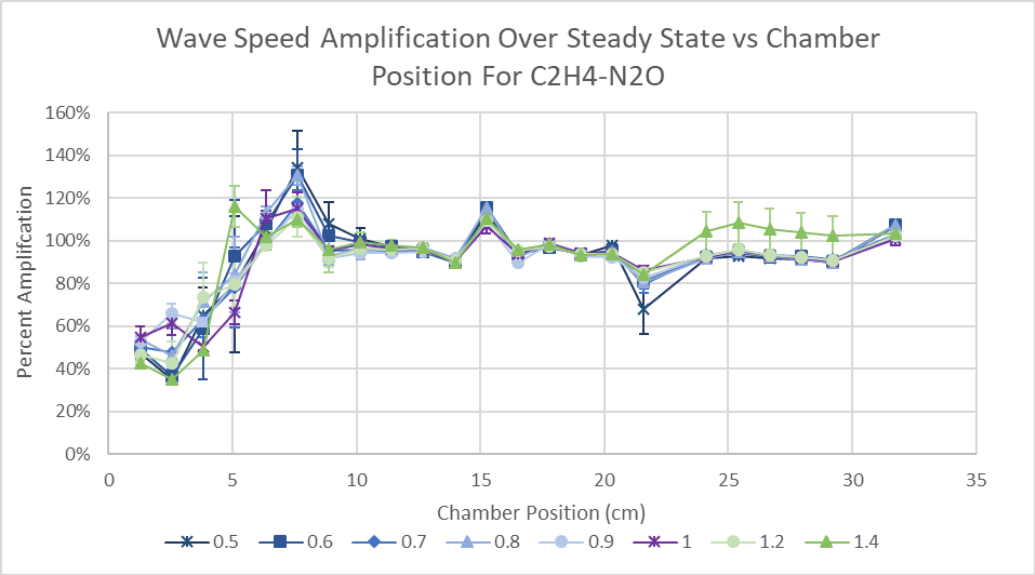

Figure 46:Wave speed Amplification vs. Expansion Chamber Position for the 6.25 A/A_o section and the C_2H_4-N_2O reaction at 1atm

For the CH_4-N_2O pressure impulse results shown in Figure 47, the results appeared to match that of the spike amplification case observed in the lean C_3H_8-N_2O reactions at the same conditions for Φ=0.5 to 1.0. The peak pressure amplification was observed to be 2.5 to 4 times the inlet condition with this peak occurring noticeable later in the chamber at an axial position between 9 cm and 14 cm. It is however observed that this peak amplification drops off at the sociometric and fuel-rich condition with these being amplified to only 1.5 to 2 times the inlet condition. A unique behavior is observed for the Φ=1.2 test case, with the detonation initially appearing to undergo the detonation amplification phenomenon. However, the reinitiation event appears to be insufficient to fully DDT combustion resulting in the pressure attenuating to a lower than steady-state condition afterward, signifying deflagration. Looking at the pressure traces in the first zone of the chamber shown in Figure 48, it appears that the incoming detonation is still decoupled with the greater energy requirement to recouple the detonation explaining why the combustion doesn't completely DDT after initial amplification.

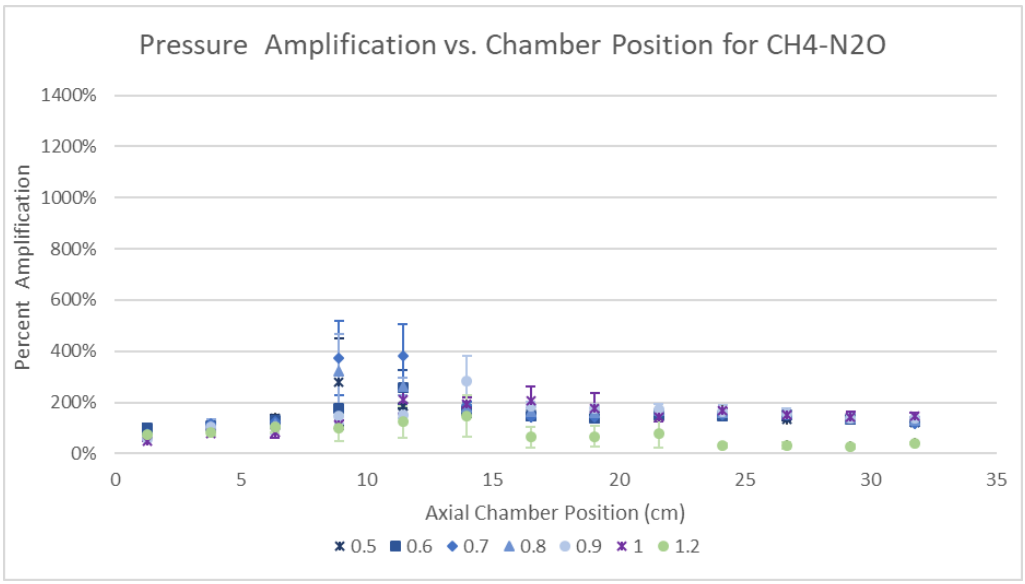

Figure 47:Pressure Amplification vs. Expansion Chamber Position for the 6.25 A/A_o section and the CH_4-N_2O reaction at 1atm

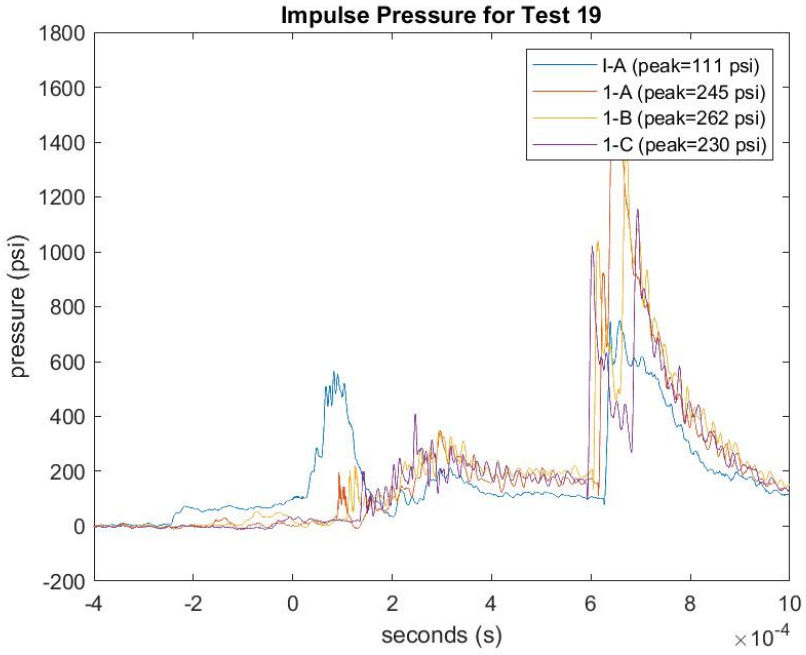

Figure 48: Pressure Traces for the CH_4-N_2O reaction at Φ=1.2 and a back pressure of 1 atm in Zone 1 of the 6.25 A/A_o section

For the wave speed behavior shown in Figure 49, it was found that the triggering of the ion probe in the Φ=1.2 test case was too unreliable to show any meaningful results. This was due to the incomplete DDT of the combustion before reaching the inlet of the chamber resulting in a lower concentration of ionized gases in the flame front. The wave speed behaviors in this reaction

show more variation in the decoupling and recoupling events than in the previous two cases. For Φ from 0.5 to 0.8, the recoupling event appears to occur at an axial position of 6 cm. The Φ=0.9 and 1.0 detonations remain decoupled longer, recoupling at a chamber position of approximately 13 cm. This indicates a weaker reinitiation event that needs more reflected transverse shocks to increase the heat release behind the flame front to recouple the detonation. This also could explain why the peak pressure amplification what observed to be lower for the Φ=0.9 and 1.0 cases since the energetic recoupling of the detonation is noticeably less energetic.

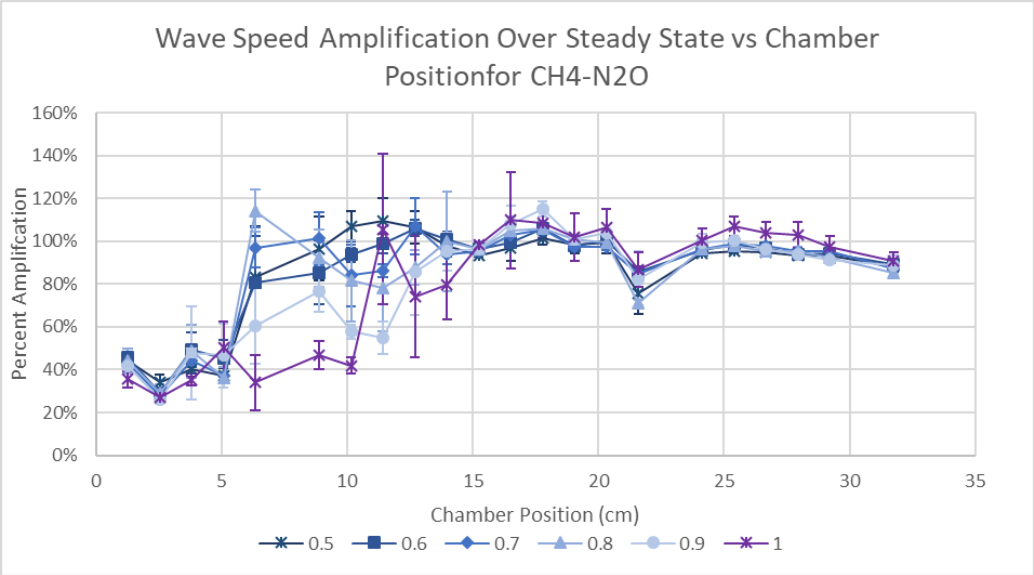

Figure 49:Wave speed Amplification vs. Expansion Chamber Position for the 6.25 A/A_o section and the CH_4-N_2O reaction at 1atm

4.3-Sub-Atmospheric Results

For the sub-atmospheric testing, it was found that the variation of ±0.5 psi that was inherent in the vacuum system had much more of an effect on incoming detonation wave than in the atmospheric testing. Normalizing the pressure peak data like that done for the atmospheric 6.25 A/A_o testing was conducted. This normalization however had to be extended to the pressure trace data with variation in the inlet condition being carried through the pressure traces resulting in the pressure appearing to drop or increase between zones in an inconsistent manner.

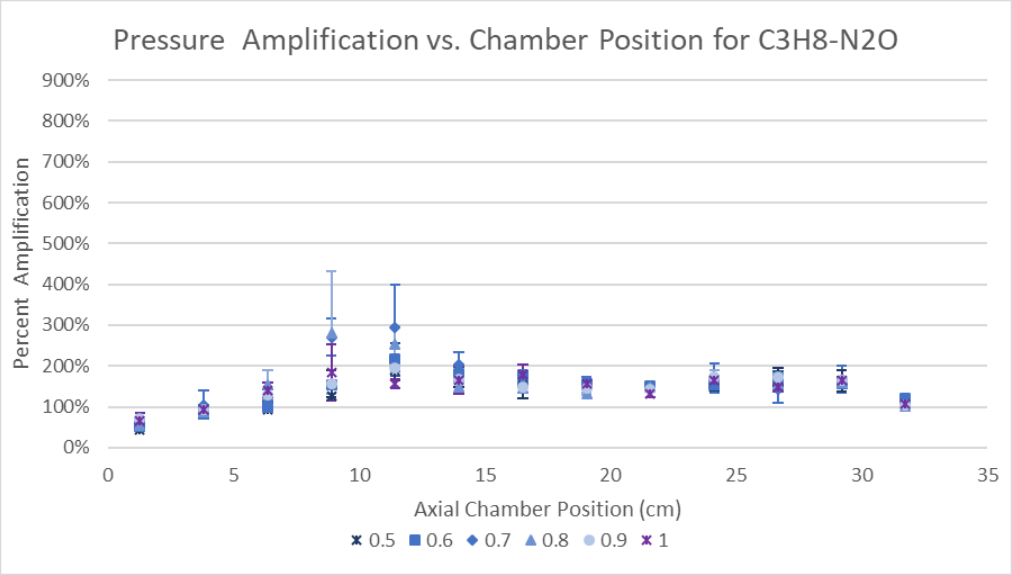

Figure 50:Pressure Amplification vs. Expansion Chamber Position for the 6.25 A/A_o section and the C_3H_8-N_2O reactions at 0.5 atm

Starting with the baseline C_3H_8-N_2O reaction at 0.5 atm shown in Figure 50, the amplification behavior that is observed is distinctly different from that of the 1 atm. Firstly, the detonation appears to recouple further into the chamber at an axial position of 9 cm to 13 cm rather than the 6 cm to 9 cm in the atmospheric case. This additional decoupling can be more readily seen when comparing the progression of the amplification phenomenon at the two different back pressures at Φ=0.7 shown in Figure 51. The wave speed graph, shown in Figure 52, also shows this increased decoupling behavior with the acceleration of the flame front beginning at a chamber position of approximately 8 cm. The reinitiation of the flame front also appears to happen less cleanly with wave speed fluctuating when the flame front accelerates to recouple with the shockwave.

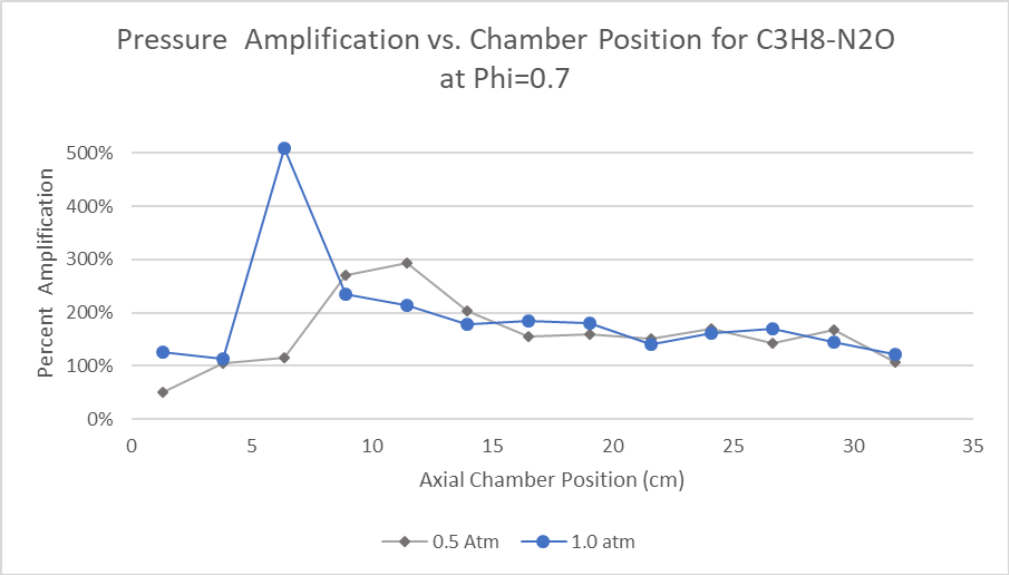

Figure 51: Pressure Amplification vs. Expansion Chamber Position for the 6.25 A/A_o section and the C_3H_8-N_2O reactions at Φ=0.7

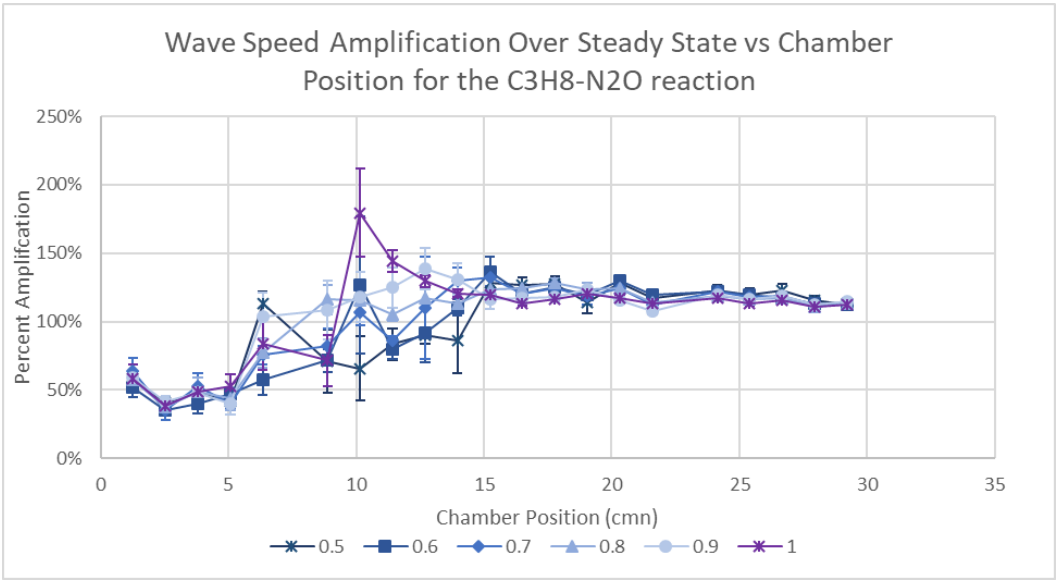

Figure 52: Wave speed Amplification vs. Expansion Chamber Position for the 6.25 A/A_o section and the C_3H_8-N_2O reactions at 0.5 atm

Additionally, the amplification behavior of the detonation at Φ=0.7 appears at first glance to match that of the steady amplification behavior compared to the spike amplification seen in the atmospheric testing. However, the behavior when looking at the pressure traces of the detonation is actual the spike amplification behavior with spike behavior being observed for all Φ's tested

using C_3H_8-N_2O at the subatmospheric condition. This reason for this discrepancy can be seen in Figure 53 where the three different detonation progressions at Φ=0.7 are graphed individually. This shows that two of the progressions have a consistent spike amplification behavior with the third showing a very inconsistent detonation progression. This results in the average progression of the detonation appearing to be a steady amplification case but with the pressure traces showing a different spike behavior. This ties back to the issues laid out in the Experimental Limitations section where the deviation between tests was observed to be high around the reinitiation event and it being expected that the exact point of this reinitiation may not be captured by the pressure probes.

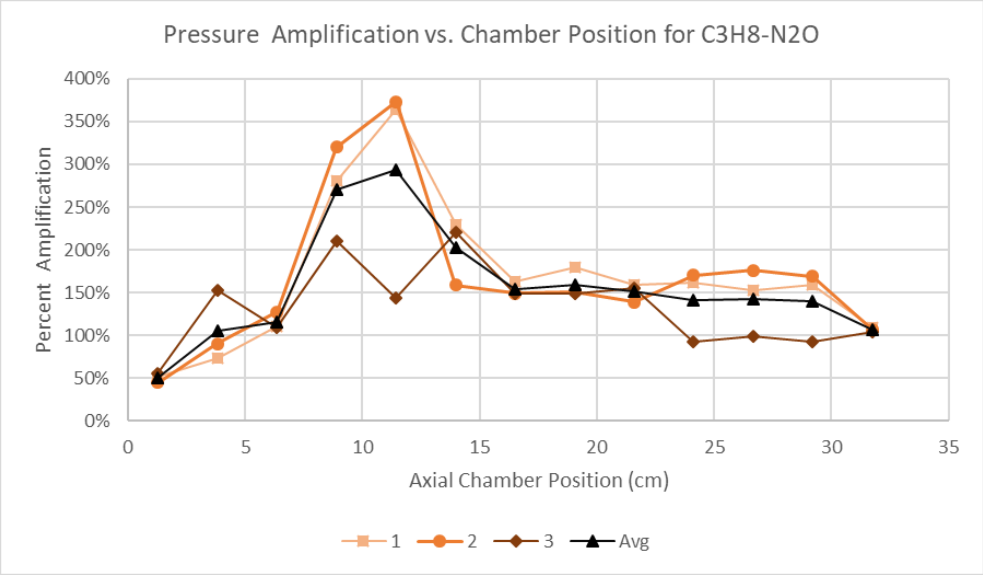

Figure 53: Individual Plots of Pressure Amplification vs. Expansion Chamber Position for three C_3H_8-N_2O detonation progressions at Φ=0.7 and a back pressure of 0.5 atm

Moving on to the CH_4-N_2O reactions at 0.5 atm, the general pressure peak behavior of the detonation with respect to Φ is shown in Figure 54. The first noticeable behavioral difference is the increased decoupling of the detonation with the comparison between the progression of the atmospheric and sub-atmospheric cases at Φ=0.7 shown in Figure 55. Looking at the Φ=0.5, 0.6, and 0.7 cases, the detonation appears to recouple around an axial position of 17 cm compared to

the 9 cm to 13cm of the atmospheric case. For the other three Φ's, the detonation appears to recouple even later in the chamber at 22cm for the Φ=0.8 and 0.9 cases with the stochiometric test case appearing to recouple very close to the end wall of the chamber. Overall, two different amplification behavior were observed in these cases with the first matching a heavily decoupled spike amplification case observed when Φ=0.5 to Φ=0.8. The second and completely new behavior observed in the Φ=0.9 and 1.0 conditions displayed an even more decoupled behavior to the point that the end wall of the chamber affects the amplification process resulting in peak amplification occurring in the outlet. Looking at the pressure traces for the end wall amplification behavior, shown in Figure 56, the double spike of a decoupled detonation is observed for every pressure probe point in the expansion chamber. It is noted that the detonation is accelerating to recouple in the final few probe points in the expansions chamber and there is the possibility that detonation reinitiates in the distance between the end wall and the last probe point. Regardless if the end wall forces the detonation to recouple or recoupling occurs immediately before the end wall, the proximity of detonation recoupling to the end wall and the narrowing of area geometry at the end wall causes an even higher amplification of the detonation in the outlet to the chamber. This is a result of the detonation being confined by the end wall with the pressure only able to escape through the smaller area of the outlet tube. creating an extremely amplified detonation in the outlet tube.

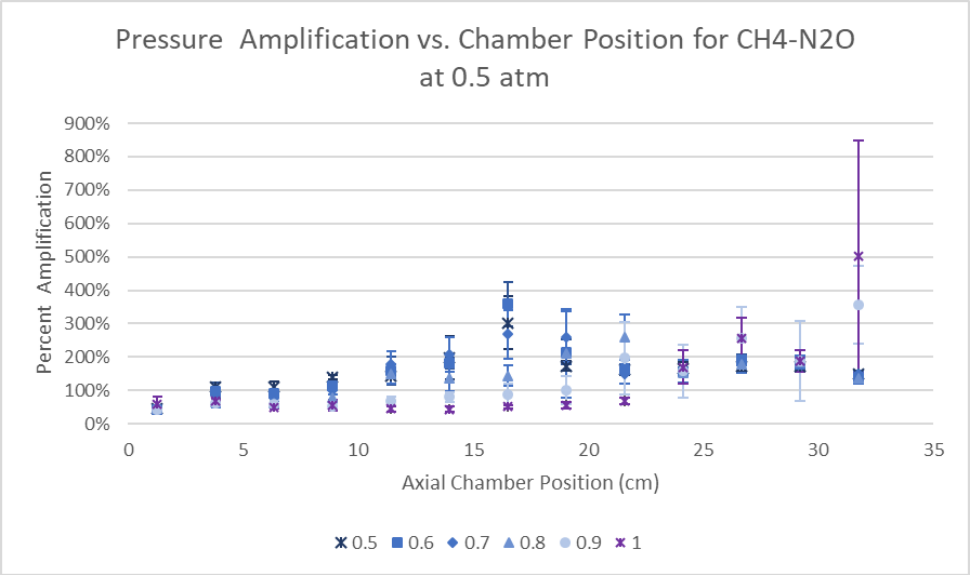

Figure 54: Pressure Amplification vs. Expansion Chamber Position for the 6.25 A/A_o section and the CH_4-N_2O reactions at 0.5 atm

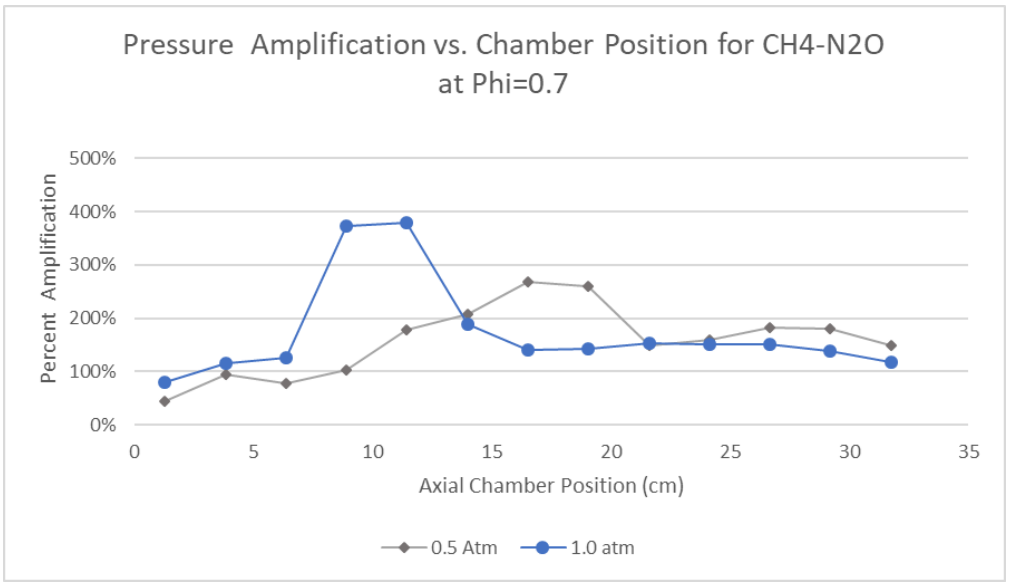

Figure 55: Pressure Amplification vs. Expansion Chamber Position for the 6.25 A/A_o section and the CH_4-N_2O reactions at Φ=0.7

For the wave speed measurements, the triggering of the ion probes was largely inconsistent with this being attributed to the larger decoupling observed for the majority of the expansion chamber resulting in a change in the triggering behavior of the ion probes. The graph for the subatmospheric CH_4-N_2O wave speed data is shown in Figure *57*. For the Φ=0.5 to 0.8 reactions, the detonation acceleration past the steady-state condition at a chamber position of 12 cm to 14

cm. With the peak pressure impulse around 17 cm, the delay between these two events signifies that the detonation is more decoupled with the flame front needing to cover a larger distance. Looking at the remaining two cases where Φ=0.9 and 1.0, the effect of the end wall of the chamber is clearly present. The detonation remains decoupled further into the chamber, only accelerating to recouple at an axial position of approximately 27cm. When it does accelerate to recouple, it appears to do so even more rapidly than the other two observed behaviors with the wave speed being overdriven to between 150% and 190% of the steady-state wave speed compared to the typical 120% peak. This like contributes to the increased pressure seen in the outlet of the chamber as the greater inertia of the detonation combined with the confinement of the detonation by the end wall creates a large pressure spike at the end wall that can only be relieved by escaping out the outlet.

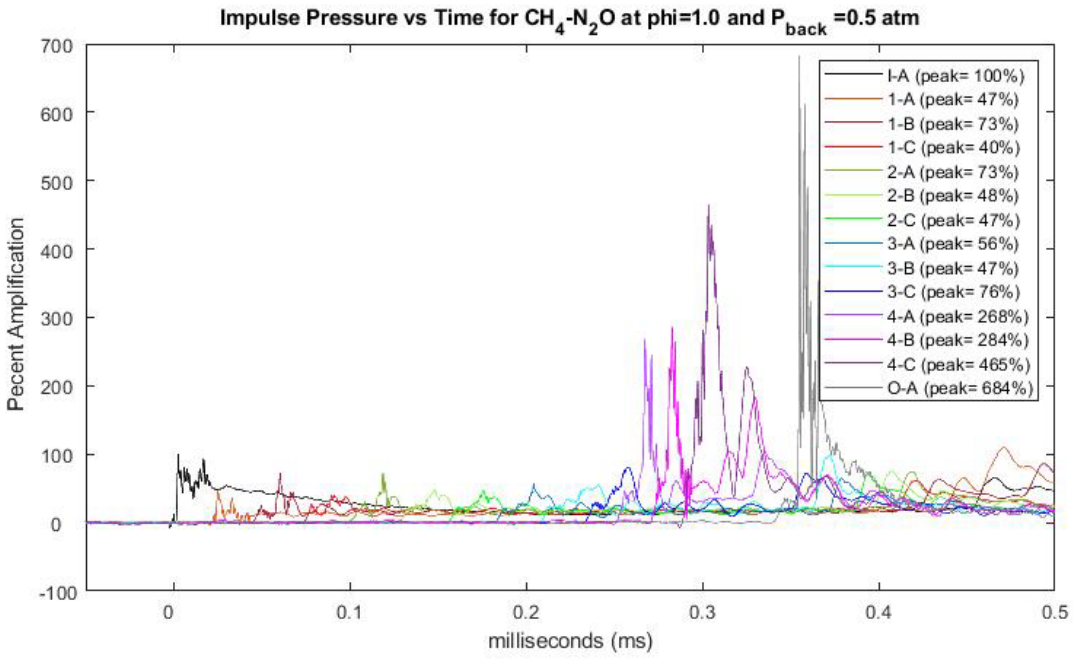

Figure 56: Pressure Traces for the End Wall Amplification Behavior for a CH_4-N_2O reaction at Φ=1.0 and a back pressure of 0.5 atm in the 6.25 A/A_o section

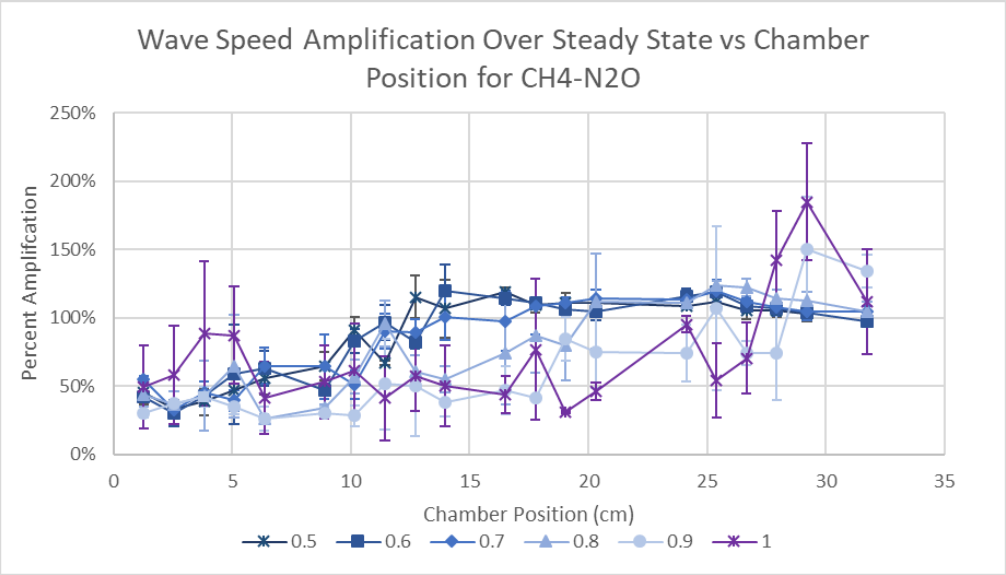

Figure 57: Wave speed Amplification vs. Expansion Chamber Position for the 6.25 A/A_o section and the CH_4-N_2O reactions at 0.5 atm

Moving on to the subatmospheric C_2H_4-N_2O testing, the peak pressure graph shown in Figure 58 was produced for the Φ's tested. This shows that C_2H_4-N_2O had the most consistent subatmospheric behavior with all of the detonations having a peak amplification at an axial position of approximately 7 cm to 9 cm. This was the same axial position for the peak amplification observed in the atmospheric case. The more noticeable change between the subatmospheric and the atmospheric result is a change in amplification behavior. The atmospheric C_2H_4-N_2O results exclusively showed the steady amplification behavior while the subatmospheric C_2H_4-N_2O results shows the spike amplification behavior. The peak of this spike was observed between 2.75 and 4.5 times the steady-state pressure impulse matching the peaks observed in the atmospheric spike amplification behavior. This difference in amplification behaviors can clearly be seen when graphing the detonation progression for the same Φ at the two different back pressure tested with the graph in Figure 59 showing this at Φ=0.7.

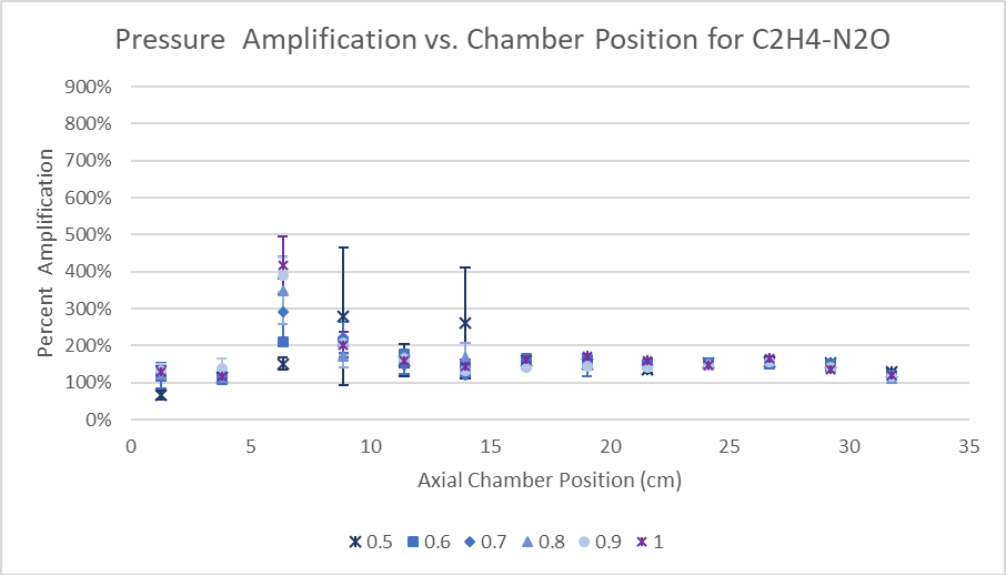

Figure 58: Pressure Amplification vs. Expansion Chamber Position for the 6.25 A/A_o section and the C_2H_4-N_2O reactions at 0.5 atm

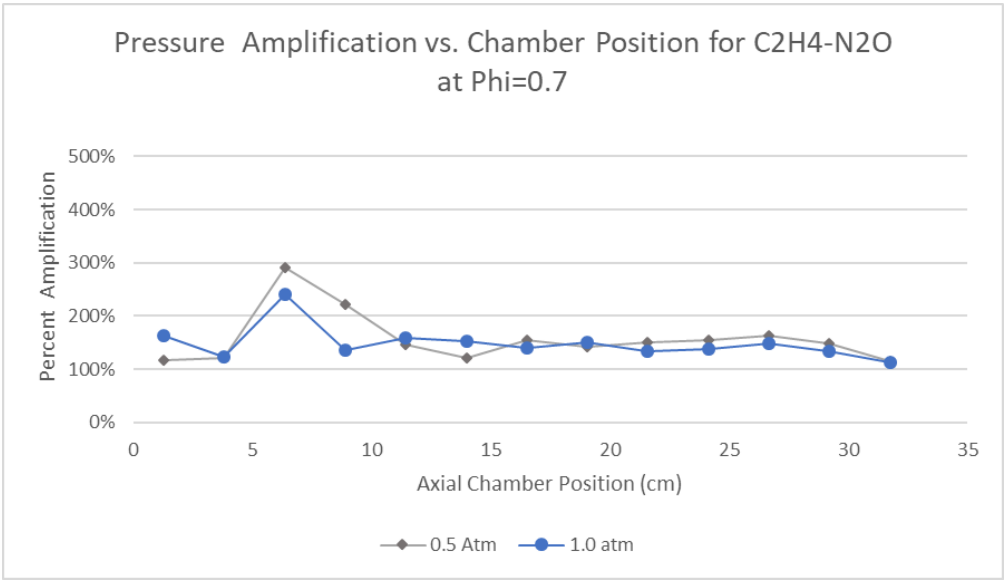

Figure 59: Pressure Amplification vs. Expansion Chamber Position for the 6.25 A/A_o section and the C_2H_4-N_2O reactions at Φ=0.7

For the wave speed measurements, the ion probe measurement for the C_2H_4-N_2O had the same consistent triggering behavior as observed in the atmospheric cases and unlike the other two subatmospheric cases. With C_2H_4-N_2O detonation being the least decoupled for either pressure case, this is potentially caused by the dispersion of the ionized gas in the flame front increasing when decoupling is increased, resulting in a change in ion probe behavior. Plotting the wave speed

results for the subatmospheric C_2H_4-N_2O testing produces Figure 60. This figure shows a slightly different reinitiation behavior than in the atmospheric case with the detonation accelerating to recouple more rapidly. This closely matches the recoupling wave speed behavior observed in the atmospheric C_3H_8-N_2O results.

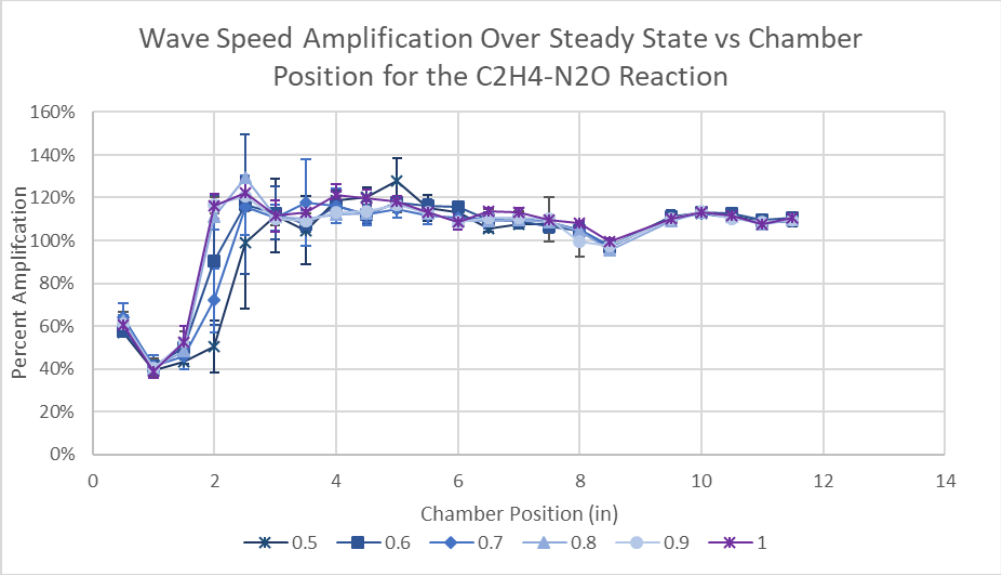

Figure 60: Wave speed Amplification vs. Expansion Chamber Position for the 6.25 A/A_o section and the C_2H_4-N_2O reactions at 0.5 atm

4.4-25.00 A/A_o Results

To test the effect of the area expansion on the detonation amplification process observed in the previous study [6] with respect to the change in area ratio, the 6.25 A/A_o test section was replaced with the 25.00 A/A_o test section. The diameter of this section is twice that of the 6.25 A/A_o, but the probe point remains in the same axial position and the overall length of the chamber remains the same. As a result, the same graphs can be produced using the results from the 25.00 A/A_o test section.

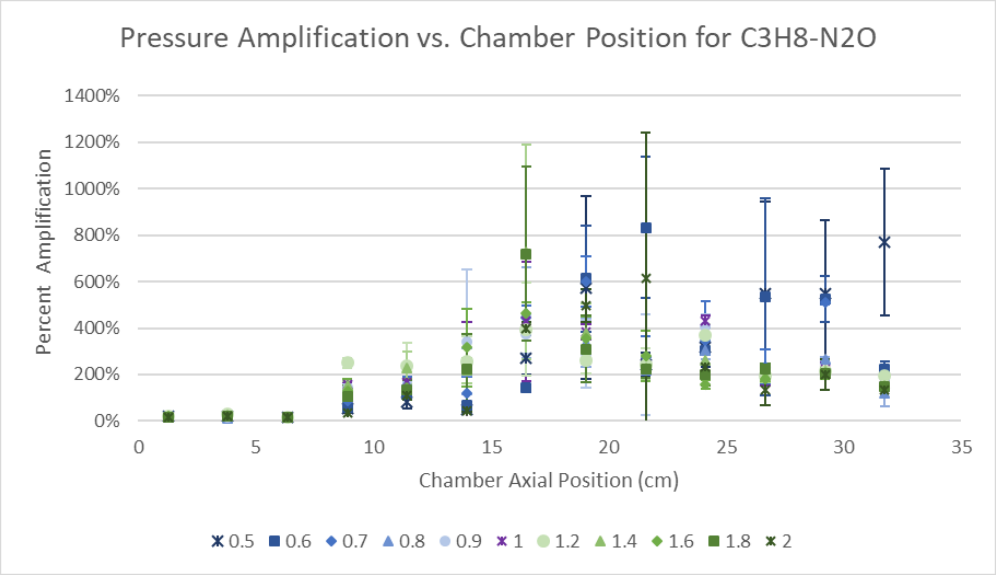

Figure 61: Pressure Amplification vs. Expansion Chamber Position for the 25.00 A/A_o section and the C_3H_8-N_2O reactions at 1 atm

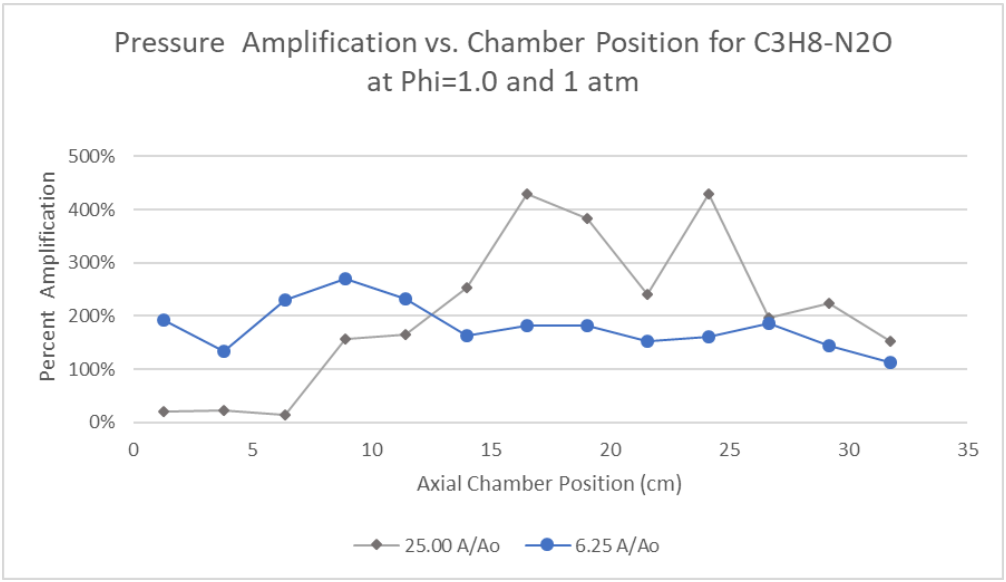

Figure 62:Pressure Amplification vs. Expansion Chamber Position for the C_3H_8-N_2O reactions at Φ=1.0 and a back pressure of 1 atm

For the baseline C_3H_8-N_2O reactions, the 25.00 A/A_o results are shown in Figure 61 with the behavior varying dramatically compared to the 6.25 A/A_o results. The first noticeable behavior change is an increased initial decoupling that was expected to be due to the increased distance to the side walls. The peak pressure impulse that is theorized to occur at the initiation point is

observed to occur between an axial position of 17 cm and 23 cm in the 25.00 A/A_o section compared to 6 cm to 9 cm in the 6.25 A/A_o testing. Graphing the different detonation propagation through the two different area expansion chambers in Figure 62 highlights this difference in the two recoupling points. Additionally, the increased decoupling also seemed to affect the overall amplification behavior with the spike amplification behavior observed in the lean C_3H_8-N_2O reactions in the 6.25 A/A_o expansion chamber now observed from Φ=0.8 to 2.0. Looking at the pressure traces for this case, shown in Figure 63, the initial decoupled is observed to significantly weaken the decoupled shockwave as seen in the first few pressure probe points. The double peak behavior that signifies that a detonation is decoupled is still observed with the initial distance between peaks being increased. The second peak is also observed to increase in peak pressure over a longer distance before recoupling into a single peak. The extremely lean reactions from Φ=0.5 to 0.7 appears to show a different behavior than the other Φ's. Looking at the pressure traces observed for this case, shown in Figure 64, it appears that the behavior closely matches that of the end wall reflection behavior that was observed in the subatmospheric CH_4-N_2O results with the same double peak decoupling observed through the entirety of the expansion chamber before amplifying at the outlet.

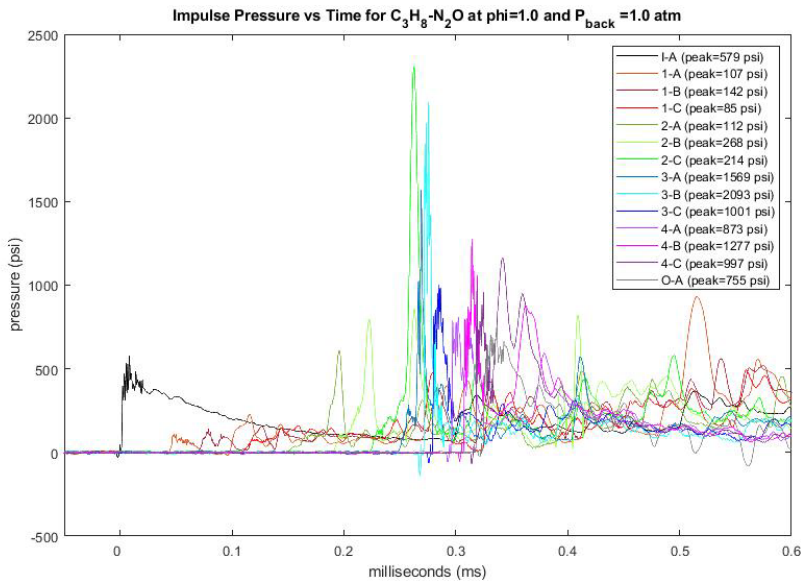

Figure 63: Pressure Traces for the Spike Amplification Behavior for a C_3H_8-N_2O reaction at Φ=1.0 and a back pressure of 1.0 atm in the 25.00 A/A_o section

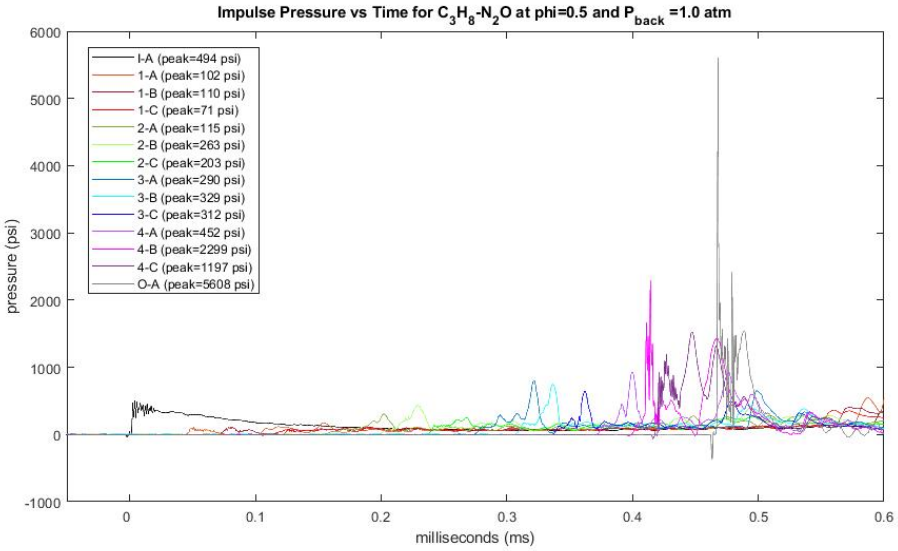

Figure 64: Pressure Traces for the End Wall Amplification Behavior for a C_3H_8-N_2O reaction at Φ=1.0 and a back pressure of 1.0 atm in the 25.00 A/A_o section

For the wave speed, it was observed that the triggering of the ion probes was significantly more inconsistent in the 25.00 A/A_o section than the testing in any of the previous cases. This is due to a combination of factors the first being the axial nature of the probe measurement and the three-dimensional behavior of the detonation making the trigger time of the first few probes not

characteristic of the actual detonation progression. The next factor is the generally increased decoupling observed for all testing in the larger 25.00 A/A_o section further dispersing the ionized gas present in the flame front and changing the triggering behavior of the detonation. The last factor was the higher amplification and more violent detonation event seen in the testing with the large area expansion with this causing damage to the ion probe over time. This damage affected the triggering behavior of the detonation making it difficult to accurately determine the wave speed. These ion probes would be replaced as the damage was noticed, but it was difficult to notice changes in the ion probe behavior caused by this damage while testing so the data was often affected by the damaged probes. The attempts to eliminate outliers cause by these various issues resulted in the wave speed plot shown in Figure 65, where various wave speed measurements had to be omitted due to the ion probe data creating nonsensical wave speed values such as negative wave speed measurements. This graph remains consistent enough to see some clear behavior in wave speed progression, but the data is still generally incomplete and slightly inconsistent. The reinitiation behaviors can be fit into 3 groups. The first group consists of the reactions from Φ=0.9 to a Φ=1.8 and is characterized by a recouple at an axial position of 13 cm to 15 cm with this behavior closely matching the more decoupled spike amplification cases. The second group consists of the Φ's equal to 0.6, 0.7, 0.8, and 2.0, where the detonation appears to be further decoupled, recoupling at an axial position of 20 cm before attenuating afterward back down to a similar point to that of the first group. The last group is consistent exclusively of Φ=0.5, where the wave speed behavior shows a large decoupling for most of the expansion chamber before being very overdriven during the last few centimeters of the expansion chamber with this matching other end wall amplification cases

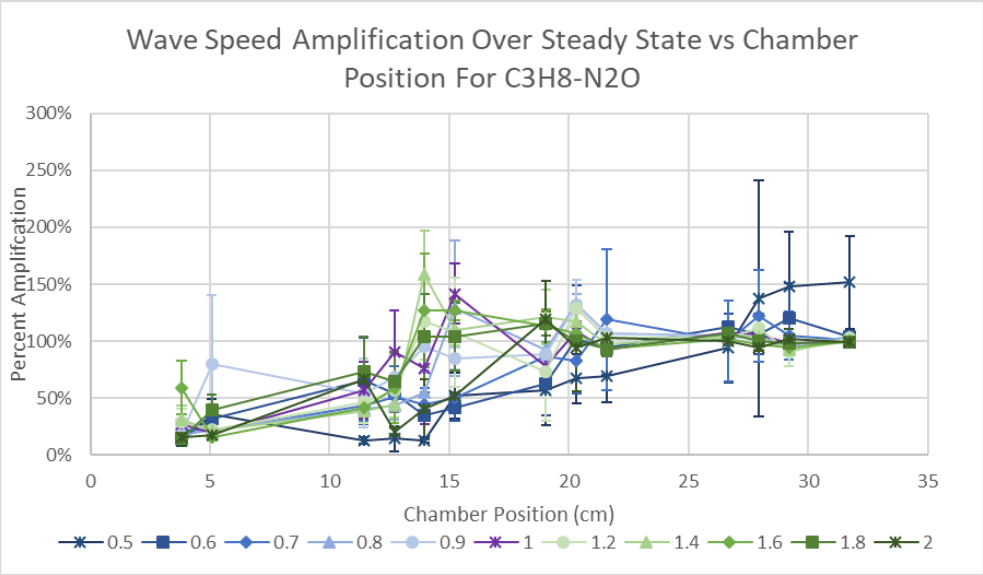

Figure 65: Wave speed Amplification vs. Expansion Chamber Position for the 25.00 A/A_o section and the C_3H_8-N_2O reactions at 1.0 atm

Moving on to the CH_4-N_2O testing, the incomplete DDT of the incoming detonation was found to occur again during this round of testing in the Φ=1.2 case. As a result, it was decided to not proceed further with the Φ=1.2 case as this would not behave normally due to this decoupled inlet detonation. This results in Figure 66 being produced from the pressure impulse traces for the remaining Φ's. It is immediately noticeable that the increased decoupling seen for this reaction in the smaller area expansion was amplified by the larger area expansion in this test case. This appears to decouple the detonation for the entire expansion chamber with a few cases that appear to have the characteristic pressure ramp of a detonation accelerating to recouple that contacted the end wall first. As a result, the amplification behavior appears to be dominated by the end wall reinitiation behavior that was first observed in the subatmospheric testing with this reaction. This is resulting in a noticeably amplified outlet for all Φ's tested with this peak amplification being measured at 2.5 to 4.5 times the inlet pressure impulse.

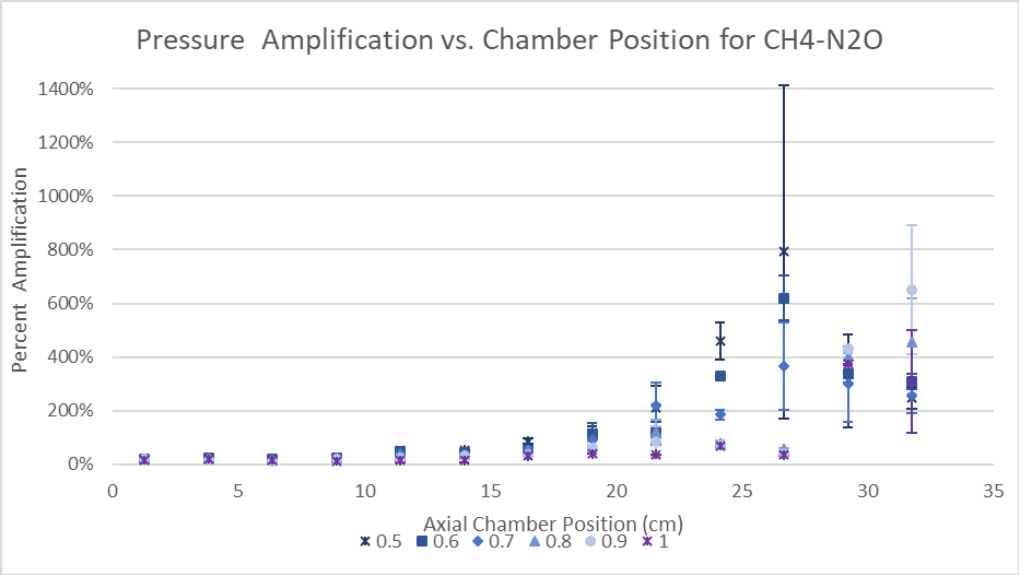

Figure 66: Pressure Amplification vs. Expansion Chamber Position for the 25.00 A/A_o section and the CH_4-N_2O reactions at 1 atm

For the wave speed measurement for the CH_4-N_2O reactions in the larger expansion chamber, the problems with the ion probe measurement were even more prevalent with the detonation being decoupled for most of the expansion chamber. This resulted in even more nonsensical data in the wave speed plot that had to be removed to establish a coherent plot. This results in the graph shown in Figure 67 with more data points removed than in the other results in the larger area expansion section. General behavior trends are still able to be discerned with the graph showing every detonation case remaining decoupled for most of the expansion chamber. The detonation does appear to have the characteristic dramatic overdriving of the detonation near the end wall of the chamber that has been seen in other cases of end wall amplification behavior.

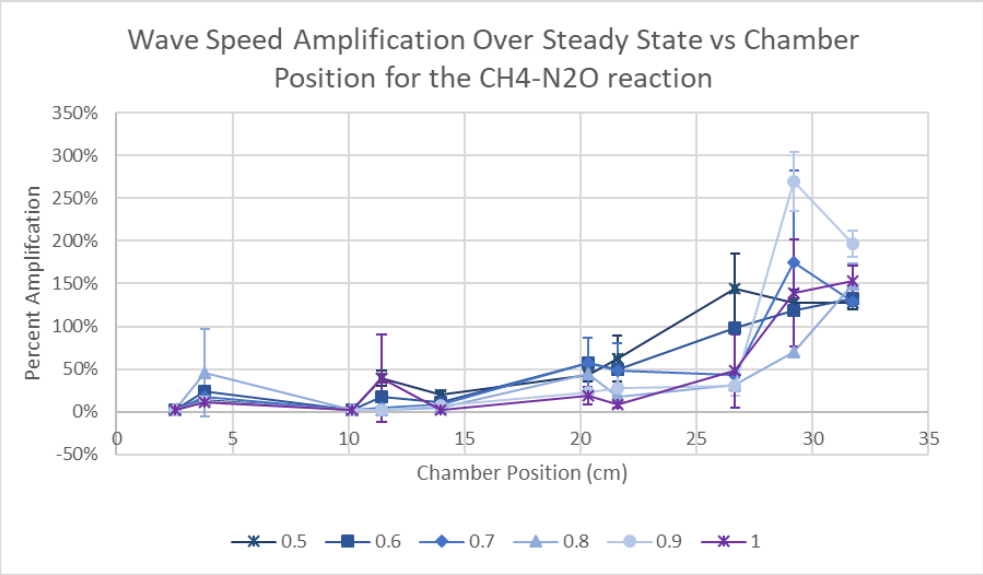

Figure 67: Wave speed Amplification vs. Expansion Chamber Position for the 25.00 A/A_o section and the CH_4-N_2O reactions at 1.0 atm

Moving to the C_2H_4-N_2O reaction, the peak pressure impulse results from these tests are plotted in Figure 68. Like the other reactions in the larger area expansion chamber, the detonation is observed to be initially more decoupled than in the smaller area expansion chamber. This decoupling difference can be seen in Figure 69 where the detonation in the 6.25 A/A_o section was observed to recouple at an axial position of approximately 7 cm while the 25.00 A/A_o detonation recoupled at an axial position of 12.5 cm. This recoupling point is largely consistent across the range of Φ tested except when Φ=0.5 where recoupled occurred at an axial position of 17 cm. The increase in decoupling of the detonation in the large area expansion seems to have changed the detonation behavior with detonations in the larger expansion chamber exclusively undergoing the spike amplification behavior for the C_2H_4-N_2O reaction compared to the exclusively steady behavior seen in the smaller expansion chamber.

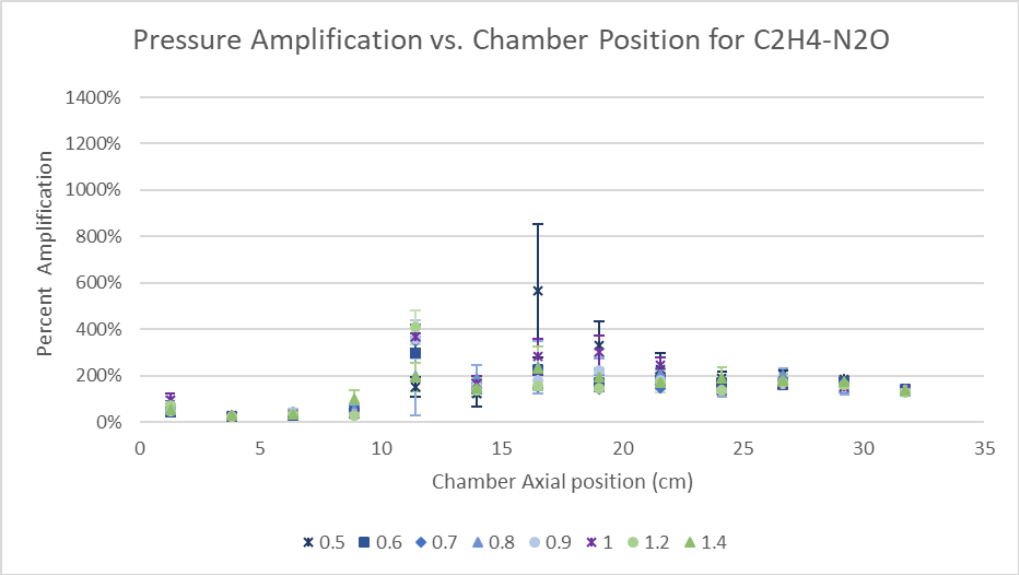

Figure 68: Pressure Amplification vs. Expansion Chamber Position for the 25.00 A/A_o section and the C_2H_4-N_2O reactions at 1 atm

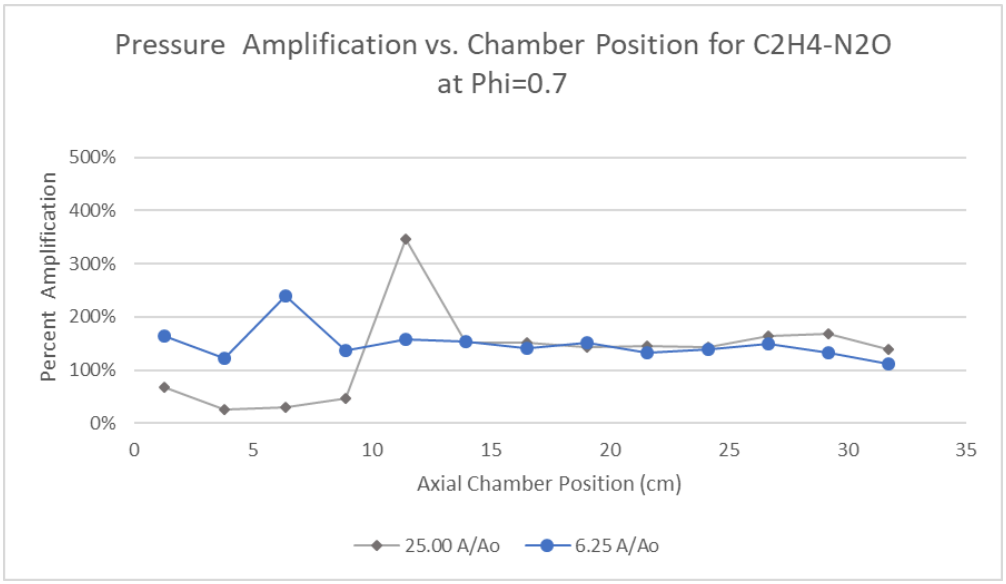

Figure 69: Pressure Amplification vs. Expansion Chamber Position for the C_2H_4-N_2O reactions at Φ=0.7 and a back pressure of 1 atm

For the wave speed result, Figure 70 was produced from the testing for the C_2H_4-N_2O reaction in the 25.00 A/A_o test section. Again, issues with the ion probe triggering behavior resulted in bad wave speed data that was removed from the graph. Look at the wave speed propagation, the detonation appears to accelerate to recouple for most of the Φ's at 12.5 cm which is the approximate reinitiation point observed in the pressure graphs. The exception to this behavior

was the Φ=0.5 case which accelerated to recouple at an axial position of 15 cm which is also mirrored in the peak pressure graph. It is also noted that the detonation appears to be overdriven to around 150% of the steady-state wave speed compared to the 120% peak seen in the smaller expansion chamber testing. This overdriven state also exists for a period after the detonation is believed to be recoupled. What is causing this overdriven behavior to persist is generally unknown, with this behavior potentially just being another artifact from the issues found with the ion probe behavior.

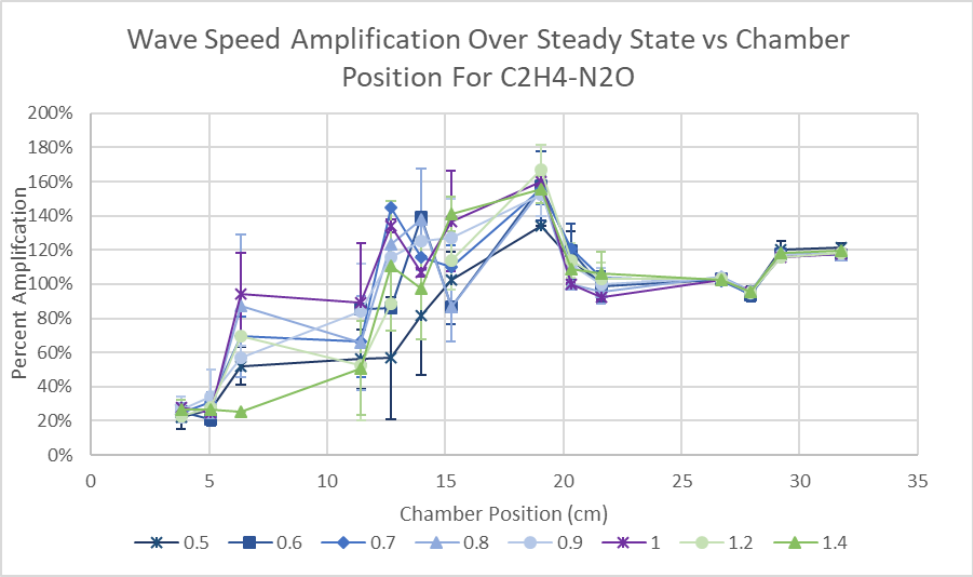

Figure 70: Wave speed Amplification vs. Expansion Chamber Position for the 25.00 A/A_o section and the C_2H_4-N_2O reactions at 1.0 atm

4.5-Detonation Amplification Behaviors

4.5.1-Cell size dependency

The lack of optical access in the modular test section made it impossible to directly observe the number of detonation cells or cell size for the detonation being tested. However, approximations and trends taken from literature can be used to correlate observation in this study to changes in λ. The previous study by Chin et al. [7] showed that the C_3H_8 and N_2O mixture used during their tests had a $\lambda = 1.3 \pm 0.14$ mm. It should be noted that the reaction mixture was believed

to be slightly fuel-lean for this study, so this value is not expected to be minimum λ but will be used as such in this analysis due to this being the closest approximation of minimum λ that could be found in literature. CH_4 and O_2 mixtures have been shown λ = 2.3 mm at an Φ =1.0 and C_2H_4 and O_2 mixture has shown λ = 0.8 mm at an Φ = 1.0 [8]. Due to the similar λ behavior between N_2O and O_2 reactions, these numbers will be used as an approximation of the minimum cell size for the respective reactions with N_2O. For the dependence of λ on Φ, only the behavior in air was found in literature for C_3H_8 and C_2H_4 shown in Figure 71 and in O_2 for CH_4 shown in Figure 72 [8], but these general trends are largely held to be similar between air, O_2, and N_2O reactions. These plots show a minimum λ occurring around the stochiometric condition and increasing exponentially when Φ approaches either extremum. The rate at which λ increases also is observed to be larger for fuel-lean reactions with a lower increase in λ seen for fuel-rich reactions for the same change in Φ.

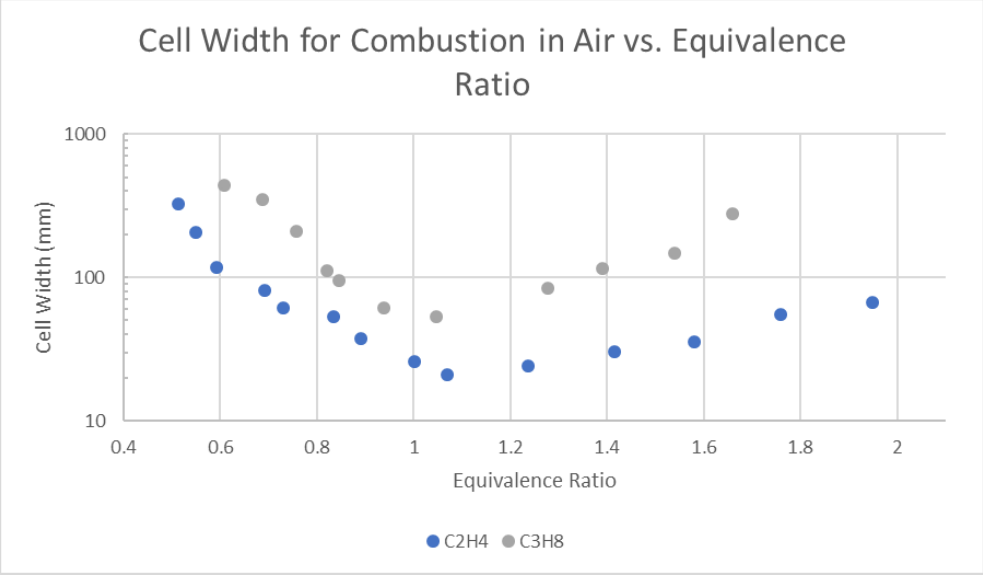

Figure 71: Cell Width vs Equivalence Ratio for C_2H_4 and C_3H_8 reaction in air [8]

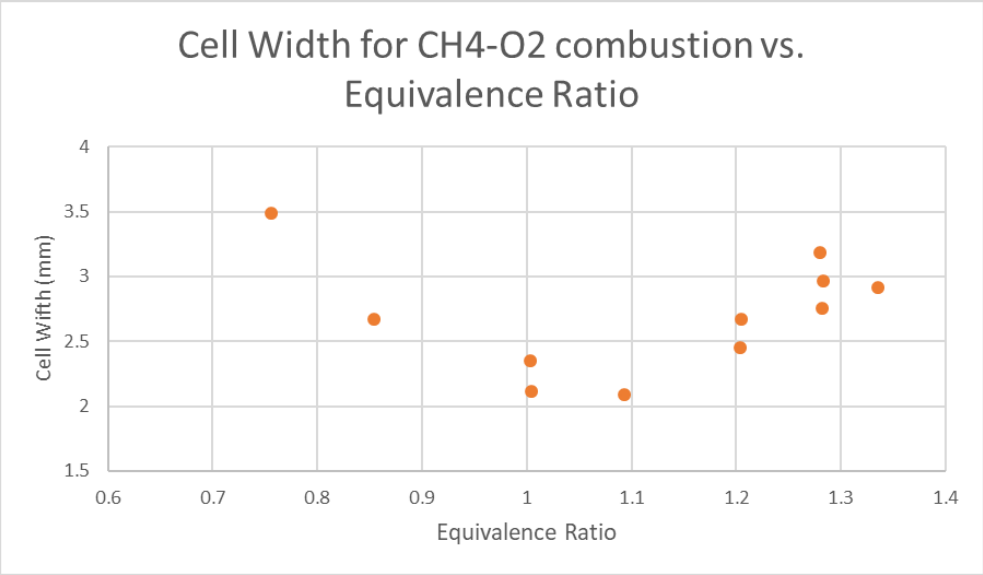

Figure 72: Cell Width vs Equivalence Ratio for CH_4 in O_2 [8]

Based on the estimates of the minimum λ for each reaction, this gives a maximum number of cells in the initial detonation of 12 cells for the C_2H_4-N_2O reaction, 5 cells for the CH_4-N_2O reaction, and 8 cells for the C_3H_8-N_2O reaction. Looking at the atmospheric results in the 6.25 A/A_o section for the three reactions at the stoichiometric condition, Figure 73 is produced to show the changes in detonation amplification behavior. Looking at the peak amplification point that coincides with the reinitiation point, there is a clear correlation between location and the number of detonation cells. A lower number of initial detonation cells in the inlet tube corresponded to the detonation reinitiating further down the expansion chamber with the number of cells increasing towards the critical number moving the reinitiation point closer to the inlet. Additionally, the C_2H_4-N_2O reaction and the C_3H_8-N_2O reaction appear to display a characteristic steady amplification behavior with the detonation being only slightly decoupled entering the area expansion. For the CH_4-N_2O reaction, based on the average pressure peaks plotted in Figure 73, it would appear that the behavior is that of a more decoupled steady amplification behavior but looking at the actual

pressure traces shown in Figure 74 the CH_4-N_2O reaction appears to display more of the spike amplification behavior.

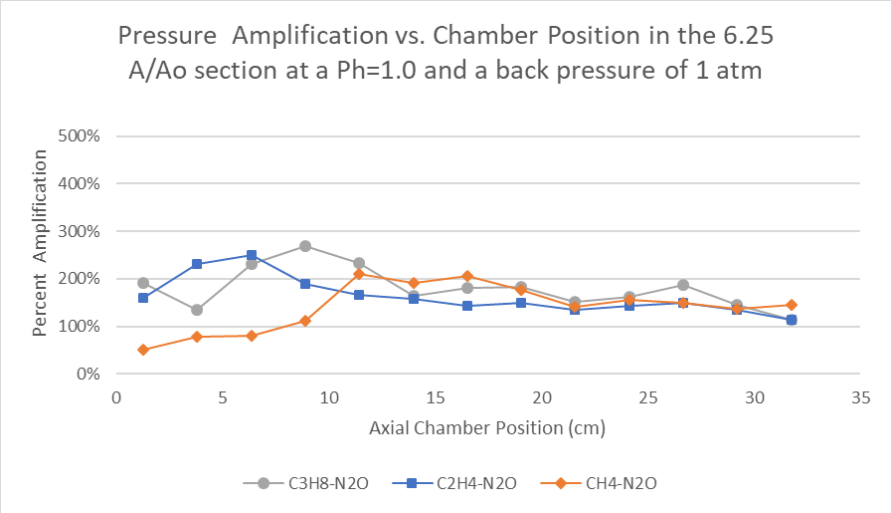

Figure 73: Pressure Amplification vs. Expansion Chamber Position for various reactions in the 6.25 A/A_o at Φ=1.0 and a back pressure of 1 atm

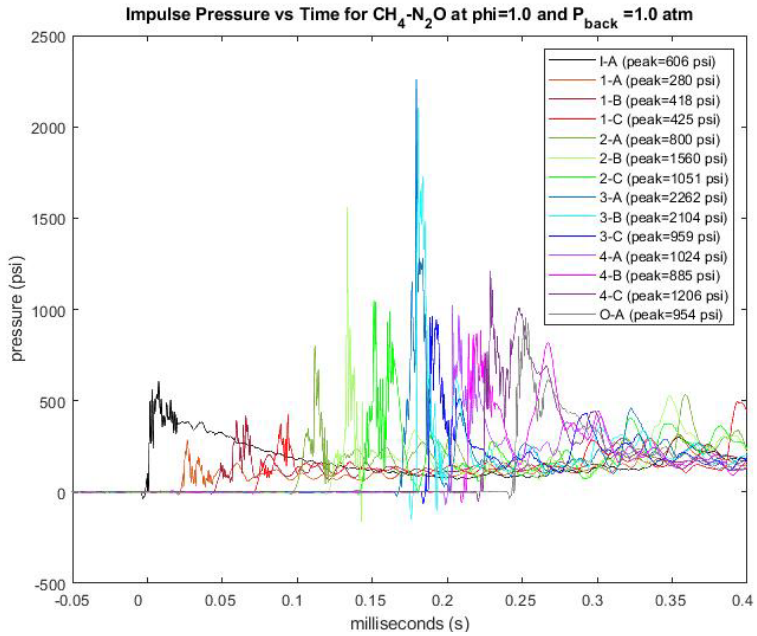

Figure 74: Pressure Traces for the Spike Amplification Behavior for a CH_4-N_2O reaction at Φ=1.0 and a back pressure of 1.0 atm in the 6.25 A/A_o section

With this spike behavior being observed in the CH_4-N_2O reaction with approximately 5 detonation cells in the incoming detonation and steady amplification seen in the C_3H_8-N_2O reaction

with an estimated 8 cells, a critical cell number in the 6.25 A/A_o section where a detonation will transition from steady amplification behavior to spike amplification behavior was identified and narrowed to between 5 and 8 cells. This predicted transition point appears to be present in the general behavior of the C_3H_8-N_2O reaction pressure peak data shown in Figure 41. The steady behavior was observed in the reactions from Φ=1.0 to 1.8 and transitioned to spike amplification when Φ=0.5 to 0.9 and Φ=2.0. This match indicated that an increase in λ crosses a threshold causing a critical cell number in inlet condition. Two transition points observed in the C_3H_8-N_2O reaction for Φ=0.9 to Φ=1.0 and Φ=1.8 to Φ=2.0 also seem to be predicted by the λ behavior with respect to Φ shown in Figure 71. With the λ increasing rapidly as the reaction become more fuel-lean, this threshold λ is quickly crossed by the fuel-lean reaction but the slower increase in λ as the reaction becomes more fuel rich meaning the fuel-rich reactions do not cross the threshold until Φ=2.0.

Looking at the back pressure effects on detonation amplification behavior, the λ is expected to increase with a decrease in back pressure based on general trends seen in literature and shown in Figure 75 [8]. This back pressure change allows for the effect of λ to be isolated from the changes to the chemical kinetic that occur when changing the fuel gas or Φ. The C_2H_4-N_2O reaction saw the clearest effect of this change in λ with the atmospheric testing exclusively displaying steady amplification with a completely transitioning to spike amplification behavior at the subatmospheric condition. This indicates a strong correlation between the λ which determines the number of detonation cells in the inlet tube and the detonation amplification behavior. A detonation close to the critical number of detonation cells was seen to display a steady amplification behavior with a threshold in the number of inlet cells eventually being crossed as the number of cells decreased until spike amplification behavior was observed. This was cell number

dependence was seen in the transition from atmospheric to subatmospheric for the C_3H_8-N_2O reaction where the detonation was observed to display a mix of steady and spike amplification behaviors in the atmospheric case and then completely transition to the spike amplification behavior in the subatmospheric case. For the CH_4-N_2O reaction behavior only at the stoichiometric condition, the change from the atmospheric condition to the subatmospheric condition showed a similar transition in detention behavior, this time from spike amplification to end wall amplification. However, the subatmospheric testing with the CH_4-N_2O reaction showed a change in detonation behavior with respect to Φ that appears to contradict that predicted from the Φ-λ relationship. This behavior, highlighted in Figure 76, showed a detonation closer to the sociometric condition when λ should be close to the minimum displaying, the end wall amplification behavior with the detonation behavior transitioning to spike amplification behavior as the reaction became increasingly fuel lean and the λ increasing. The behavior is theorized to be caused by the activation energy of the detonation preventing the reinitiation of the detonation and not by the λ or number of cells in the inlet tube. The effect of the activation energy on the reinitiation behavior will be discussed further in section 4.5.2.

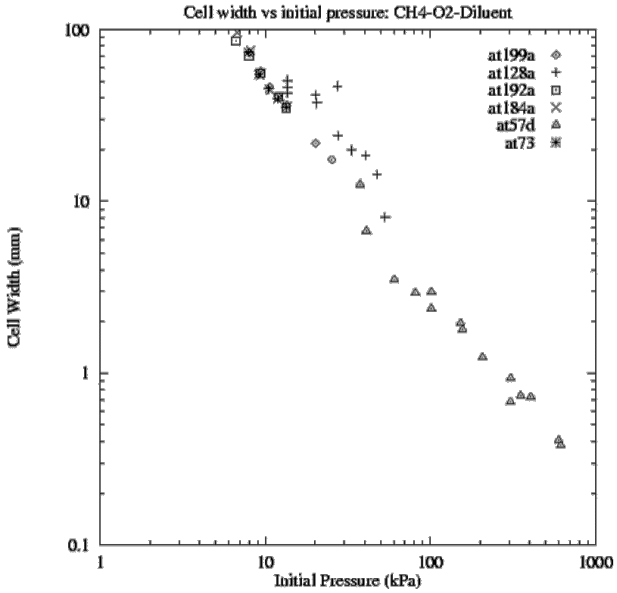

Figure 75: Cell width vs. Initial Pressure for the CH_4-O_2 reaction [8]

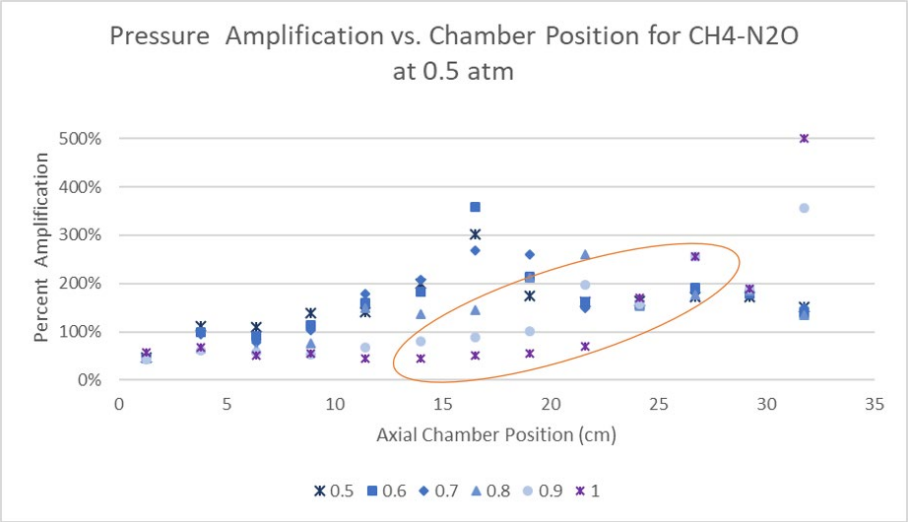

Figure 76: Pressure Amplification vs. Expansion Chamber Position for the 6.25 A/A_o section and the CH_4-N_2O reactions at 0.5 atm with anomalous behavior

With the testing of the larger 25.00 A/A_o, it was shown that the decoupling behavior is affected by this area expansion. This effect is theorized to be fundamentally linked to the behavior of the detonation diffraction. Conceptually, this can be justified by looking at the expected effect on a detonation the area ratio at the theoretical extremes would have. With an area ratio of 1, there is no area transition so the detonation is unaffected and will continue to propagate as a CJ detonation. On the other hand, a detonation with an infinite area expansion is essentially propagating into an unconfined space and thus would complete DDT due to the sub-critical nature of the detonation. This would also predict a critical area expansion below which a detonation will successfully transition into the larger area expansions with studies such as Pantow et al.[5] showing this behavior. The criticality of the detonation determined by dividing the actual number of cells in the inlet tube by the critical tube number of cells is also theorized to affect the reinitiation behavior beyond determining if the detonation is subcritical.

Compiling pressure peak plots for which the number of inlet cells can be estimated in both the 6.25 A/A_o and the 25.00 A/A_o section produces Figure 77. This graph shows the slightly

subcritical C_2H_4-N_2O reaction, with an estimated number of detonation cells of 12 compared to the critical number of 13, recoupling the closest to the inlet in either expansion chamber. Additionally, the move from the smaller area expansion to the large expansion transition the C_2H_4-N_2O reaction from displaying the steady amplification behavior to the spike amplification behavior. Moving on to the C_3H_8-N_2O reaction, which was estimated to have 8 cells, decoupling was observed further down both expansion chambers compared to the C_2H_4-N_2O reaction cases with the same transition from steady to spike amplification observed when moving to the larger area expansion. Moving on to the CH_4-N_2O reaction, the detonation in the 6.25 A/A_o section reinitiated further into the expansion chamber than the other two reactions with the detonation showing the spike amplification behavior. When looking at the transition from the smaller area expansion to the larger area expansion, the detonation was observed to be decoupled up until the end wall with the detonation displaying the end wall amplification behavior.

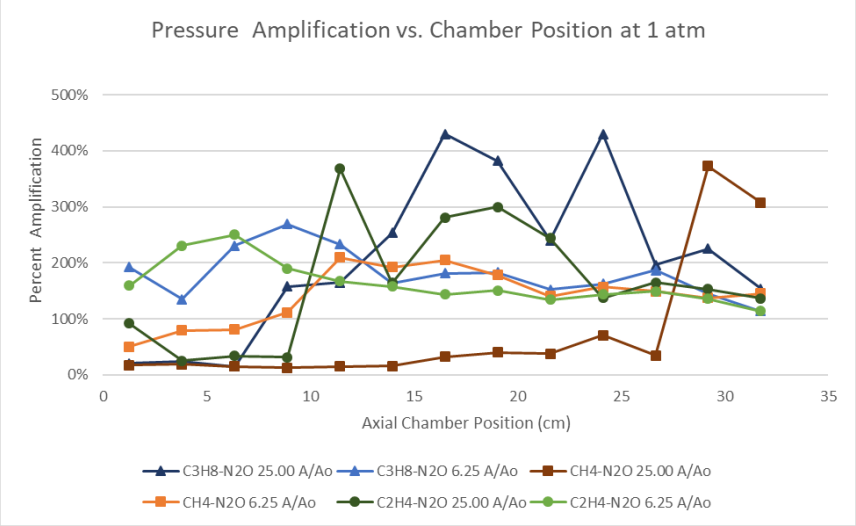

Figure 77: Pressure Amplification versus Chamber Position for Various Reaction Mixture and Area Expansion at Φ=1 and a Back Pressure at 1atm

All this indicates that the trend observed in the λ is compounded by the effect of the area expansion ratio with a slightly subcritical detonation readily transitioning into a relatively small area expansion and displaying a relatively steady amplification behavior. This steadier

amplification is attributed to the decoupling of the detonation not being complete across the entire shock front with the axial portion of the detonation wave remaining closely coupled. The transverse portion of the detonation wave, however, does decouple as the wave travels through the area expansion with this behavior being shown in the transverse detonation reinitiation case shown in Figure 5. This transverse decoupling creates the shock reflection mechanism that overdrives the detonation, but without the large slug of shocked but uncombusted gas in the axial portion of the detonation, there is no pressure spike at the reinitiation point.

By increasing the area into which the detonation is expanded or by decreasing the criticality of the inlet detonation, the detonation will decouple further with this theorized to be a complete decoupling across the entire flame front. This creates a condition similar to that shown in the Mach stem reinitiation shown in Figure *5*. With the detonation fully decoupled, the shock reflects off the side wall and coalesces in the middle of the chamber, reinitiating the detonation and consuming the shocked but uncombusted gas in the diffracted induction zone. The heat released from the consumption of this shocked gas creates a large thrust impulse on the shock front. This creates the large characteristic spike in the pressure as the thrust impulse attempts to rapidly accelerate detonation with the initial inertia of the shockwave limiting its ability to do so with this compressing the induction zone. With the shocked but uncombusted gas fully consumed, the detonation rapidly attenuates back down to a more typical overdriven state similar to that seen in the steady amplification case.

Compounding both the effects of the lower detonation criticality and increasing the area expansion ratio results in a dramatic increase in decoupling with the transverse shock reflections no longer adding enough energy back into the reaction to reverse the DDT process. This results in the detonation completely decoupling and the induction zone of the detonation continuing to

diffract with this being shown by the complete decoupling case in Figure 5. Given enough chamber length, the detonation may either completely DDT or may reinitiate if the shock pumping is given enough time to reverse the DDT process, but the end wall of the expansion chamber is contacted by the shockwave first. The shockwave is then reflected off the end wall and contacts the flame front. The detonation is then reinitiated by this shock reflection with the reactants in the induction zone being rapidly consumed similar to that of the spike amplification case. This peak pressure impulse is expected to be significantly higher directly at the end wall than in the spike amplification case as a result of better confinement of the reinitiation event by the end wall of the expansion chamber. This creates a heavily amplified outlet as the pressure is only allowed to escape through the narrow outlet tube. It is also of note that it theorized that this complete decoupling behavior exists on a spectrum of area expansions and detonation criticalities such that a slightly subcritical detonation may not be reinitiated by the transverse shocks in a large enough area expansion, or a very subcritical detonation may still display this end amplification behavior in a relatively small area expansion.

4.5.2-Reinitiation Behavior and Activation Energy

The decoupling behavior predicted by the changes in λ wasn't however consistent with all the behaviors observed. This was noticed in the CH_4-N_2O reaction at the subatmospheric condition and in the testing in the larger 25.00 A/A_o section with the cases near the stoichiometric condition being observed to be more decoupled than the lean conditions. The increased decoupling was sufficient that, in the subatmospheric case, the detonation transition from displaying the spike amplification behavior at fuel-lean conditions to displaying the end wall amplification behavior at the stoichiometric condition. For the 25.00 A/A_o section results, the behavior was entirely end wall amplification, but only the lean cases appeared to have been in the process of reinitiating before

the end wall. With this anomalous behavior exclusively seen in the end wall amplification behavior, it is theorized the initial detonation diffraction behavior remained that which was predicted by the change in λ, but the energy reintroduced by the initial transverse shock reflection was insufficient to reinitiate the detonation. This allows the detonation to propagate through the entire chamber in a decoupled state before the end wall reflection forces reinitiation. The theorized mechanism driving this is the activation energy of the reaction stalling the initial reinitiation mechanism and keeping the detonation in a decoupled state until the end wall forced reinitiation.

In an attempt to quantify the change in activation energy with respect to Φ, a simulation of the detonation reaction using the Cantera toolbox [13] was attempted and used to calculate an approximate activation energy for the global reaction. This reaction was simulated at CJ conditions that were calculated using a separated detonation toolbox developed for Cantera [14]. This simulation involved a volume reactor at the CJ pressure and temperature with the reaction mixture corresponding to the reactants and Φ's tested. The ignition delay time was then calculated for this reactor using the point of the maximum rate of change in temperature. The temperature of the reactor was then increased by 0.1% with this new reactor being simulated having a different ignition delay. The activation energy was then calculated using the change in temperature and the difference in the ignition delays. This results in the graph shown in Figure 78. This shows a clear increase in activation energy as Φ increases for the CH_4 case, but the increase is only around 5% from Φ=0.5 to 1.0. This increase seems too low to fully explain the observed behavior, but the actual conditions are likely significantly different than the CJ conditions simulated. Additionally, while the activation energy might be higher at the stoichiometric condition, the ignition energy should be the lowest due to the feedback loop caused by the heat release of combustion. This might

indicate that this behavior is more a product of when energy is released by the reaction than how much energy is released with the additional activation energy causing a larger ignition delay.

With the complex shock and expansion behavior of the initial decoupling, it is also unknown how accurate the assumption of constant volume is. Part of the amplification process likely being confined by the shockwave and thus mostly a constant volume reaction while other portions of the phenomenon expanded transversely to fill the expanded area and closer to a constant pressure reaction. The full chemical kinetic mechanism that drives this anomalous behavior is potential too complex to have a simple analogous reactor model such as the one attempted fully explain the behavior seen. A full exploration of this mechanism by simulating the entire diffraction and amplification phenomenon in detail or taking direct measurements of the phenomenon using high-speed chemiluminescence imagery is likely necessary to provide any further insight into this behavior.

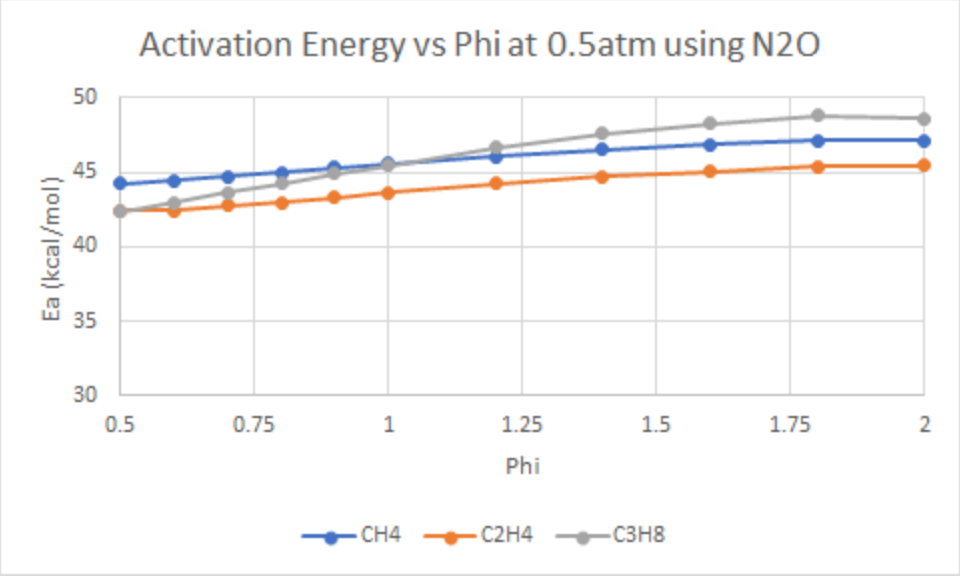

Figure 78: Activation Energy (Ea) versus Φ for reactions in N_2O for various fuels at CJ conditions for a detonation at an initial condition of 0.5 atm

5-Optical Study

To attempt to further investigate some of these reinitiation behaviors, an optical study was attempted just looking at the general luminescence of combustion. This study was delayed by the initial shutdown of the LPAS in the 300 lab and then by the first optical test section design failing during the first test firing which necessitated a redesign. With the manufacturing of the redesigned test section taking longer than the time allotted for this study, a temporary fix to the original design was manufactured out of aluminum and used to perform a limited optical study of the amplification phenomenon. This study was limited to using the C_2H_4 -N_2O reaction as it was found that in the larger 25.00 A/A_o section that this reaction had the lowest peak amplification and thus would be the least likely to blow out the windows. Due to the limited time available for optical testing, the settings for the high-speed camera were finalized in the middle of testing. This resulted in settings such as the frame rate and frame size varying over the test campaign with the setting of 225,000 frames per second (FPS) and a window size of 256 pixels by 128 pixels being finalized late in testing. When performing the initial tests, it was found that the luminescence of the detonation during the reinitiation would often saturate the sensor in the Phorton S12, even at the quickest shutter speed of the camera at 0.2 μs. As a result, it was necessary to filter the light intensity using an ND filter to cut down on visible light transmission to the sensor. It was eventually found that during general amplification behavior an ND filter with an optical density of 2.0 would clearly show the detonation progression. This ultimately resulted in the detonation progression for the C_2H_4-N_2O reaction, at a Φ=0.7 and 1.0 and a back pressure of 1 atm, being fully mapped across the entire optical test section at 225,000 FPS, at an individual window size of 256 by 128 pixel using a 2.0 ND filter and a shutter speed of 0.2 μs. Additional measurements were taken more ad hoc at other detonation conditions as the camera settings were dialed in with the initial testing

being conducted at a Φ=0.5 and a back pressure of approximately 0.75 atm as a weaker detonation case to slowly test the capability of the new test section to contain stronger detonation and stronger detonation. These results showed some interesting behavior not found during the recording of detonation progression at the other two test conditions and will be brought into the discussion as necessary.

During testing, three different reinitiation behavior are observed, the first was side wall reinitiation behavior seen at Φ=1.0 and a back pressure of 1atm, where a localized detonation event was observed to occur at one of the sidewalls with this behavior shown in Figure 79. The detonation is observed to have a very ill-defined flame front with weaker luminescence from the combustion indicating the detonation is decoupled. A localized detonation event is then seen in the 13.3μs frame at one of the side walls, which then travels across the decoupled wavefront shown in frames 17.8 μs to 26.6 μs recoupling the detonation as it progresses. Rapid heat release behind the shockwave is observed as the localized reinitiation event traveling transversely through the induction zone consuming the shock but combusted gas with the luminescence from this heat release saturating the camera sensor even with the ND filter present. The detonation then progresses out of frame but is seen to establish a clearly defined flame front indicating that the detonation has recoupled with this wave observed to continue to propagate down the chamber as a coupled detonation during observation downstream of this reinitiation event. Given the observed behavior for this reaction in the 25.00 A/A_o chamber and the larger area expansion of the optical section, this case likely sits close to the transition point of the detonation from the spike amplification behavior to the steady amplification behavior. This reinitiation behavior also seems to match that of the Mach stem reinitiation simulated in Pantow et al. [5] but with only one Mach stem being formed unlike the two seen in the 2D simulations.

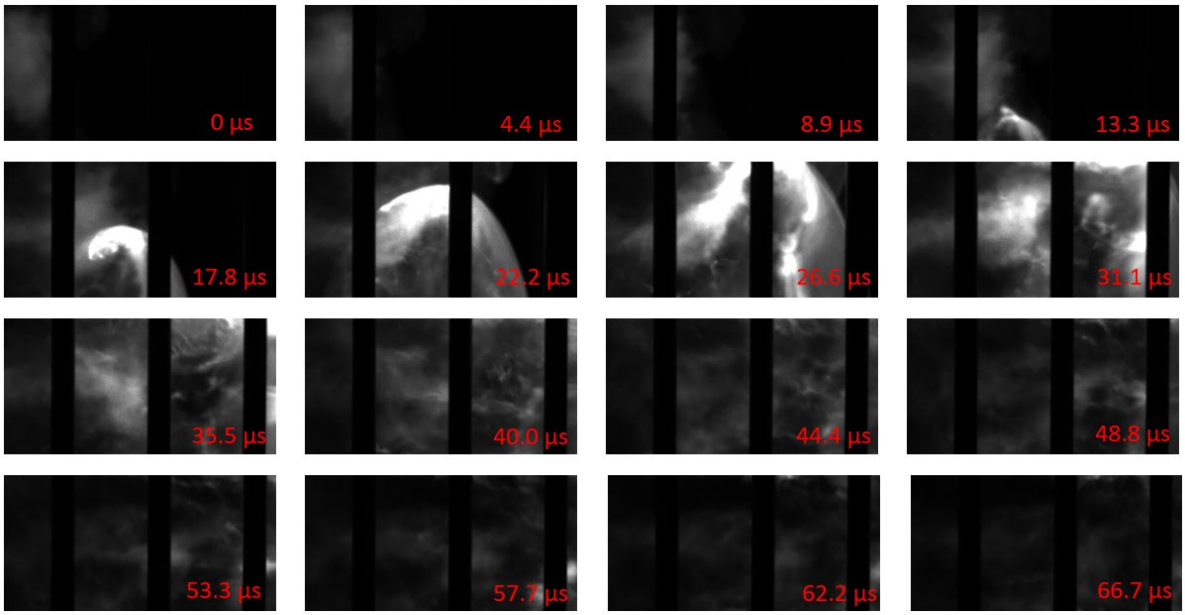

Figure 79: Side Wall Detonation Progression Imagery at Φ=1.0 and a Back Pressure of 1 atm with a 2.0 ND filter

For the next reinitiation behavior, the Φ=0.7 atmospheric test case saw a different reinitiation behavior with the localized reinitiation being observed to occur away from the side wall and the event occurring further down in the chamber. The detonation is observed to be similarly decoupled coming into frame and then in 13.3 µs frame with an increase in luminescence is observed in the middle of the chamber but the event is partial obscured by the bolts running in front of the window. The area of luminescence then increases in size at the top of the channel but doesn't seem to immediately form a clear wavefront indicative of a recoupled detonation in the 17.8 µs frame. An additional and separate reinitiation event is also seen in the 17.8 µs frame with the event being observed to propagate as a wave backward in the flow between the 17.8 µs frame and 22.2 µs. All this indicates a chaotic reinitiation behavior that doesn't match any of the previously observed reinitiation behaviors, but this chaotic event was sufficient to reestablish the detonation and allow it to propagate through the rest of the chamber. This reinitiation behavior is generally believed to be caused by complex shockwave reflections off the side wall but without observing the shock interactions directly, further insight into the reinitiation mechanism that

cannot be gained from this study. Comparing the expected behavior seen in the 25.00 A/A_o section, it would be expected this test condition would sit in the middle of the spike amplification behavior range with the even larger area expansion in the optical test section potentially shifting this case towards the transition point to the end wall behavior. This indicated that the spike amplification behavior observed during the testing with the modular test section may encompass more than one reinitiation behavior as the detonation becomes more decoupled. This results in reinitiation requiring more energy addition from the transverse shocks and the reinitiation behavior being generally more chaotic.

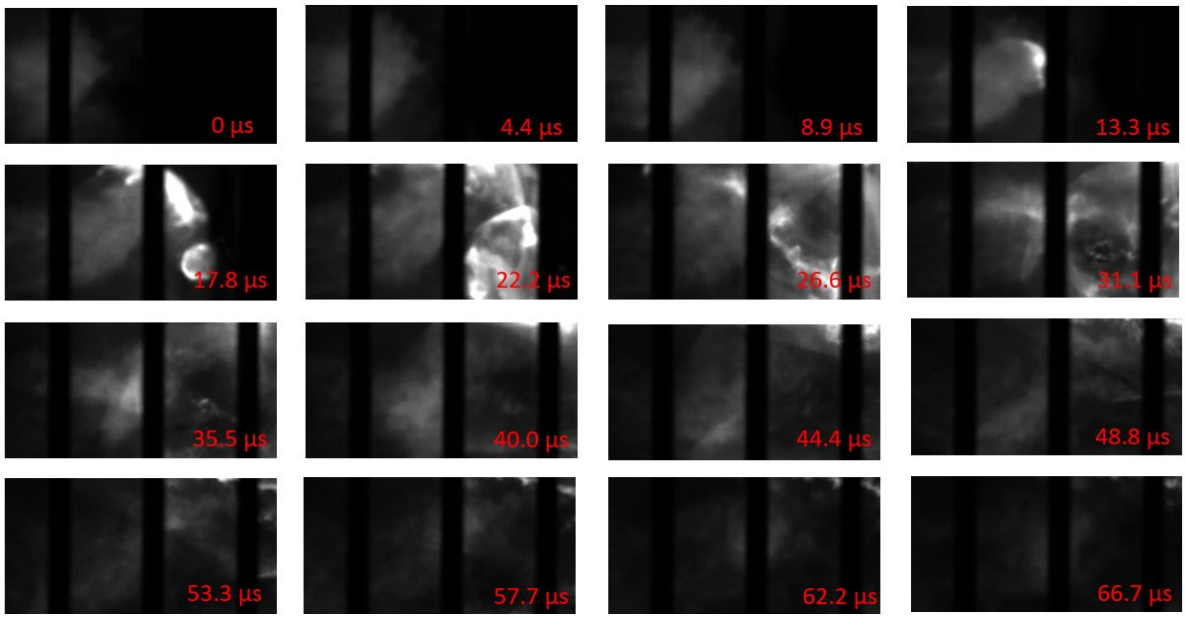

Figure 80: Middle Reflection Reinitiation Detonation Progression Imagery at Φ=0.7 and a Back Pressure of 1 atm with a 2.0 ND filter

For the last reinitiation behavior observed during the initial testing at a Φ=0.5 and a back pressure of 0.75 atm, the detonation was observed to be entirely decoupled up until the end wall of the chamber with the reinitiation being caused by the shockwave reflection at said end wall. Due to the weaker luminescence of the decoupled detonation, in this case, an ND filter was not used to allow for the incoming decoupled detonation to be seen with this resulting in the reinitiated detonation being saturated. Additionally, the high-speed camera setting for this case was still being dialed in, so the FPS was only at 125,000 FPS to facilitate a larger 256 by 140 pixel frame with the shutter speed remaining the same at 0.2 µs. This resulted in the wave speed progression seen in Figure 81. This detonation is initially seen to display the characteristic decoupled detonation with a hazy and ill-defined flame front. At the 56 µs frame, an increase in the luminescence of combustion is seen along the frame front. The subsequent frames seem to show the formation of a well-defined shock front traveling in the opposite direction of the initial flame front with the flame front continuing to travel down the chamber to consume the uncombusted gas between it and the end wall that is just out of frame. This indicates that when the shockwave reflects off the end wall

and recontacts the flame front causing increase in heat release related to the dramatic increase in luminescence. This is dramatic enough to not only force the flame front to accelerate to consume the shock but uncombusted gas between the flame front and the end wall, but the heat release is sufficient to send a shock wave back through the expansion chamber at an estimated speed of 1587.5 m/s compared to the calculated CJ speed of sound for this mixture of 1348.9 m/s [14]. Assuming the reflected wave is traveling at Mach 1, the difference between the CJ speed of sound and the observed speed of sound gives an estimated temperature that is 1.4 times the CJ condition. This indicated that the reinitiation event at the end wall is amplified well past the expected CJ condition. Due to the changes in detonation criticality from the increase in λ caused by both the fuel-lean Φ and the lower back pressure as well as the larger area expansion in the optical test section, this reinitiation behavior is expected to match the end wall reinitiation behavior see mainly during the CH_4-N_2O testing at the subatmospheric condition and in the 25.00 A/A_o test section.

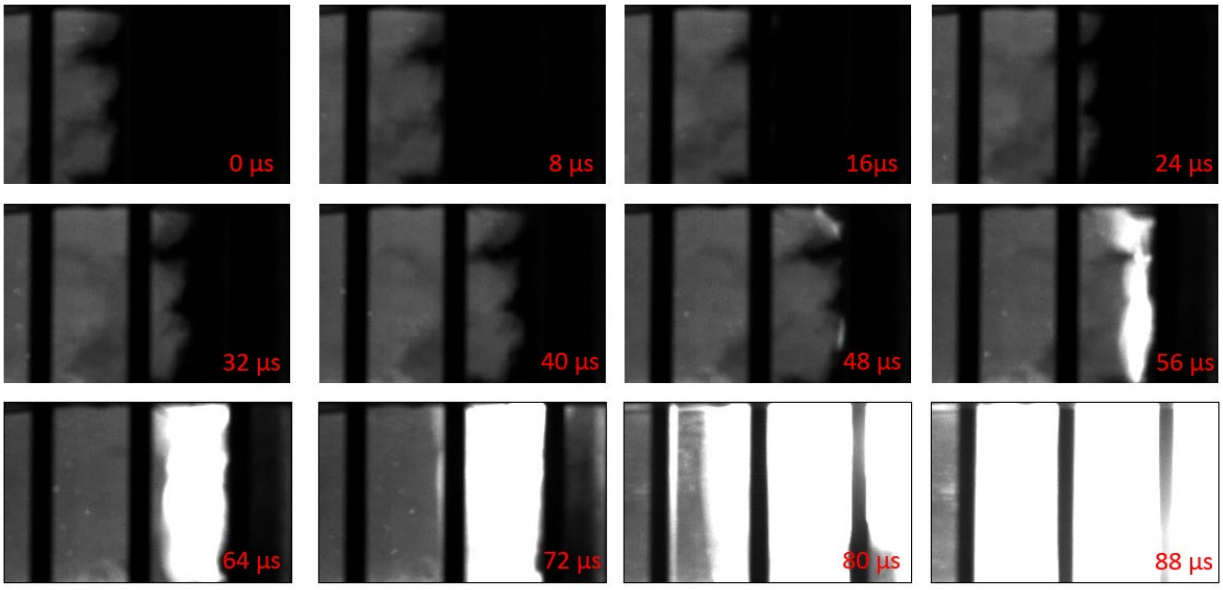

Figure 81: End Wall Detonation Reflection Initiation Detonation Progression Imagery at Φ=0.5 and a Back Pressure of 0.75 atm with no ND filter

6-Conclusion

In conclusion, a further exploration of the detonation amplification phenomenon originally characterized in Cuppoletti et al. [6] was performed to characterize the effect of the reaction mixture, equivalence ratio (Φ), and the effect of cell size (λ) and detonation criticality in the inlet tube on the amplification behavior. This was done by creating a new pneumatic control system that was able to accurately control the mass flow ratio of the fuel and oxidizer individually to create a reactant mixture at a consistent and controllable Φ. The detonation at this Φ could then be initiated and passed through the 6.25 A/A_o modular test section that Cuppoletti et al. [6] had used to observe this phenomenon. The progression of the detonation was then captured through the use of ion probes to track the progression of the flame front and piezoelectric pressure probes to capture the progression and pressure impulse of the shockwave in the expansion chamber. Testing was conducted using CH_4, C_2H_4, and C_3H_8 as the fuel gases with the oxidizer planned to be N_2O and O_2 to produce large changes in the λ of a detonation but was only performed with the N_2O due to a delay caused by a breakdown in the dilution air supply system. Variation in the Φ was used to achieve a smaller change in λ with a Φ sweep being performed from Φ=0.5 to 2.0 for each reaction The upper limit was determined by the detonation limit of the reaction and flammability limit in the exhaust system. Additional testing was performed to characterize the effect of a larger 25.00 A/A_o expansion to follow up on the observations made in the previous testing of the phenomenon and to explore the effect of moving to subatmospheric back pressure that is closer to the expected operating conditions of an ignition device using this amplification phenomenon.

These test results showed three different reinitiation behaviors, with the first behavior being a fairly steady amplification of where the detonation appears to only slightly decouple. This is due to the local decoupling in the transverse portion of the expanding detonation. As a result, the detonation doesn't have a large slug of shocked but combusted gas to significantly amplify the

detonation but the “shock pumping” behind the flame front is still enough to overdrive the detonation and amplify it. This case was mainly seen when the incoming detonation was close to criticality and the area expansion was relatively small.

For the second amplification behavior observed, the detonation appears to be more decoupled with a noticeable spike in pressure impulse at the reinitiation point. The detonation is completely decoupled across the detonation front for this behavior, a large slug of shocked but uncombusted gas is created in the diffracted induction zone. When the detonation is reinitiated, the slug of shocked but uncombusted gas is consumed, creating the characteristic pressure spike observed in the pressure traces. During the optical study, two different reinitiation behavior were observed for cases believed to experience this spike amplification behavior. The first reinitiation behavior shows a Mach stem formation at the side wall of the chamber reinitiating the detonation as it traveled transversely through the diffracted induction zone. The second reinitiation behavior showed a much more chaotic event with multiple reinitiation events being observed along the flame front with one of these reinitiation events being seen to create a shock in the upstream direction. When the slug of gas is fully consumed, the dramatic amplification of the detonation is curtailed, and the detonation returns to a more traditionally overdriven state similar to that of the steady amplification behavior. Cases that displayed this type of behavior tended to be either more sub-critical at the inlet condition or are expanded into a larger area expansion.

For the last amplification behavior, the detonation was observed to be decoupled for the majority of the expansion chamber with a spike in impulse pressure being observed near the outlet of the expansion chamber. The reflected shock off the end wall is theorized to contact the flame front, increasing the local pressure and temperature and thus the heat release. This creates a large pressure spike seen at the end of the chamber and the outlet condition. This was shown in the

optical study where the reflected shock is seen to increase the broadband chemiluminescence when intersecting the flame front. The flame front is then rapidly recoupled with this recoupling creating an amplified condition. This case was seen at the extremes of the test conditions where the inlet detonation was both very subcritical and expanded into a much larger area with the detonation having to be sufficiently decoupled such that the initial traverse reflected shock are unable to reinitiate the detonation. As a result, the detonation remains largely decoupled for the entire test section only to be reinitiated by the end wall reflection.

Looking at the effects of individual parameters, the criticality of the incoming detonation appears to be an important factor in determining the amplification behavior. Changes in λ, achieved through changes in the reactants, the Φ of the reaction, and the back pressure of the detonation, are observed to correspond to changes in the detonation behavior once crossing some threshold λ. The effect of this detonation criticality is then compounded by the effect of area expansion of the detonation tube to determine which amplification behavior occurs. A detonation that is close to the critical point but is still sub-critical and is expanded into a relatively small area expansion displays the steady amplification behavior. If this detonation is then passed into a larger area expansion or if the λ of the detonation was increased to give a more sub-critical detonation, the detonation is then observed to display the spike amplification behavior. If the effect of a decrease in detonation criticality through an increase in λ and the effect of an increase in the area expansion ratio are compounded, the detonation reaches a threshold where the transverse shock reflections are no longer able to be reinitiated the detonation. The axial shock is then reflected at the end wall creating the end wall amplification event.

A final observation was made that was not able to be explained by the effect of the detonation criticality. A detonation using CH_4-N_2O was observed to display the end wall

amplification behavior when at Φ=1.0 which should be the closest to the critical point but would display spike amplification behavior when the reactant mixture was more fuel-lean which would make the λ larger and thus the detonation more subcritical. This behavior is theorized to be caused by an activation energy mechanism that stalls the reinitiation event with the activation energy being shown to vary with respect to Φ and the fuel gas using simulated constant volume reactor. The simulation however did not adequately explain the full mechanism driving this anomalous behavior, thus warranting a further detailed exploration of the chemical kinetics behind the behavior.

6.1-Potential Applications

For the potential application, this study had the goal of looking at the fundamental dynamics of this amplification process rather than seeking to advance a particular application con. However, this research branched off work seeking to explore the use of a detonator as an ignition device. These devices have shown promise in producing a more reliable ignition event than traditional ignition methods but introduced a disruptive shockwave that tended to dramatically interfere with the operation of a given combustor or engine. This makes designing a detonation ignitor very difficult as the size of the disruptive shockwave and the energy depositing of the detonation are linked to the area of the initial detonation front. This means if you make a detonator ignitor too small the detonation would not release energy quickly enough to achieve ignition while making the detonator larger will produce a reliable ignition event, the initial shock will in turn be more detrimental to the general operation of the combustor. The amplification phenomenon presents an opportunity to modify the heat release rate of a detonation to design around this paradigm. For example, a detonation that is amplified using the end wall amplification behavior shifts the energy release that would normally occur in the middle of the expansion chamber to the

end wall of the chamber which can then be exhausted through a narrower outlet tube and into the combustor. This gives a smaller detonation front that is less disruptive but gives a greater heat release rate at the initial ignition event that is needed to achieve a reliable ignition.

Applications of the amplification phenomenon are not however limited to detonation ignitors. Given the ability of this amplification phenomenon to shift the heat release in the detonation to a different location, this could potentially see use in detonation combustors as an example with this shifting in heat release assisting in thermal management. Knowledge of this amplification phenomenon could also provide insight into the propagation behavior of accidental explosion events in confined spaces such as fire within closed fuel systems or mine explosions and allow for exploration of potential ways to mitigate these explosive events.

6.2-Future Work

Further exploration of this amplification phenomenon is still warranted with the theory to explain this phenomenon still being a work in progress. The reinitiation mechanisms behind each of the three behaviors observed in this study are still largely uncharacterized with these reinitiation mechanism shown some correlation to the pressure amplification behavior. To this end, a more in-depth optical study of the amplification phenomenon using the new optical test section design is planned with the inclusion of Schlieren imagery, along with more focused chemiluminescence imagery to look at specific reaction steps. This testing is also planned to be more holistic than the optical testing conducted in this study with more test conditions being explored and done so at a higher frame rate to better time resolve the reinitiation event. This should hopefully provide more insight into the reinitiation process by observing the shock interaction as well as the heat release of the reaction. The Schlieren imagery also allows for a closer estimation of detonation criticality at the inlet condition based on the detonation cells observed during the initiation detonation

diffraction behavior. This should help narrow down the location of behavior transitions in the detonation amplification process that were observed to correspond to changes in detonation criticality.

Additionally, a further study of the anomalous behavior observed in the CH_4-N_2O reaction is likely warranted. The activation energy mechanism theorized to cause the change in behavior that contradicts that predicted by cell size needs to be explored further as it is likely that the mechanism is more complicated than the analogous reactor model developed in this study. This could likely be explored in the chemiluminescence imaging in the planned optical study but might not be sufficient depending on which reaction step the reinitiation stalls at and the reaction step being captured by the chemiluminescence imaging in the planned study.

References

[1] T. M. Ombrello, C. D. Carter, C. Tam, K. Hsu, Cavity ignition in supersonic flow by spark discharge and pulse detonation, Proceedings of the Combustion Institute 35 (2015)2101-2108. doi: 10.1016/j.proci.2014.07.068.

[2] D.R. Cuppoletti, T. Ombrello, Cavity Ignition Dependence on Pulse Detonation Impulse Parameters, 56th AIAA Aerospace Sciences Meeting, 2018 Paper No. AIAA 2018-1358.

[3] S. R. Turns, and D. C Haworth, "Detonations," An Introduction to Combustion: Concepts and Applications, 4th ed., New York, New York, 2022, pg. 610-631

[4] V. Mitrofanov, R. Soloukhin, On the instantaneous diffraction of detonation, Sov. Phys. Dokl (1964) 1003–1006.

[5] E. Pantow, M. Fischer, T. Kratzel, Decoupling and recoupling of detonation waves associated with sudden expansion, Shock Waves 6 (1996) 131–137.

[6] D.R. Cuppoletti, T. Ombrello, K.D. Rein, Detonation Amplification and Attenuation Through Geometric Area Expansion, AIAA Scitech Forum, 2019 Paper No. AIAA 2019-1012.

[7] H. M. Chin, D. R. Cuppoletti, T. M. Ombrello, K. A. Ahmed, K. D. Rein, Energy deposition characteristics of a pulsed detonation igniter through geometric manipulation, Combustion and Flame 229 (2021), doi: 10.1016/j.combustflame.2021.02.030

[8] M. Kaneshige, J.E. Shepherd, Detonation database, GALCIT, 1997 Tech. Rep. FM97-8.

[9] Gas Correction Formula, King Instrument Company, [Online]. Available: https://kinginstrumentco.com/sizing-calculator-2/#:~:text=GAS%20CORRECTION%20FORMULA%201%20Convert%20Customer%20Gas%20Flow,the%20Air%20Equivalent%20Flow%20Rate.%20More%20items...%20. [Accessed 07 01 2022].

[10] Optical Density and Transmission, Thorlabs, Inc., [Online]. Available: https://www.thorlabs.com/newgrouppage9.cfm?objectgroup_id=266. [Accessed 07 01 2022].

[11] Variable Vacuum Generators, Norgren Ltd., [Online]. Available: https://cdn.norgren.com/pdf/IMI-Norgren-NVDF-Variable-Vacuum-Pump.pdf. [Accessed 07 01 2022].

[12] Engineering ToolBox, (2003). Gases - Explosion and Flammability Concentration Limits. [online] Available at: https://www.engineeringtoolbox.com/explosive-concentration-limits-d_423.html [Accessed 07 01 2022].

[13] D.G. Goodwin, H. K. Moffat, I. Schoegl, R. L. Speth, and B.W. Weber. Cantera: An object-oriented software toolkit for chemical kinetics, thermodynamics, and transport processes.

[Online] Available at: https://www.cantera.org, 2022. Version 2.6.0. doi:10.5281/zenodo.6387882 [Accessed 07 01 2022].

[14] J.E. Shepherd. Shock and Detonation Toolbox. [Online] Available at: https://shepherd.caltech.edu/EDL/PublicResources/sdt/, 2021 [Accessed 07 01 2022].

[15] TUFFAK GP Polycarbonate Sheet Typical Properties, Plaskolite, [Online]. Available: https://plaskolite.com/docs/default-source/tuffak-assets/product-data-sheets/pds004_gp.pdf [Accessed 07 01 2022].

Appendices

Appendix 1: P&I Diagram of the pneumatics control system

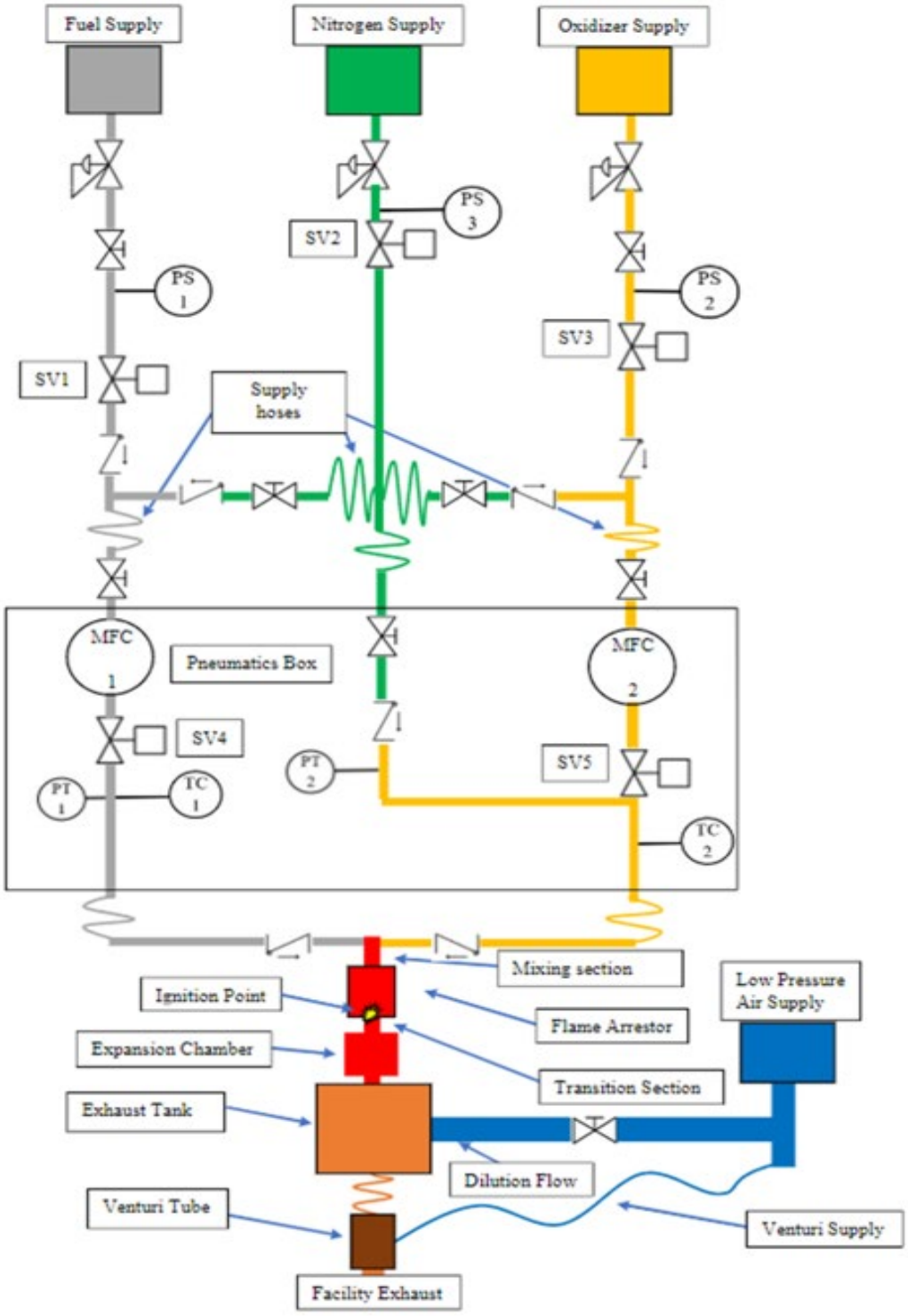

Appendix 2: PLC Program Block Diagram

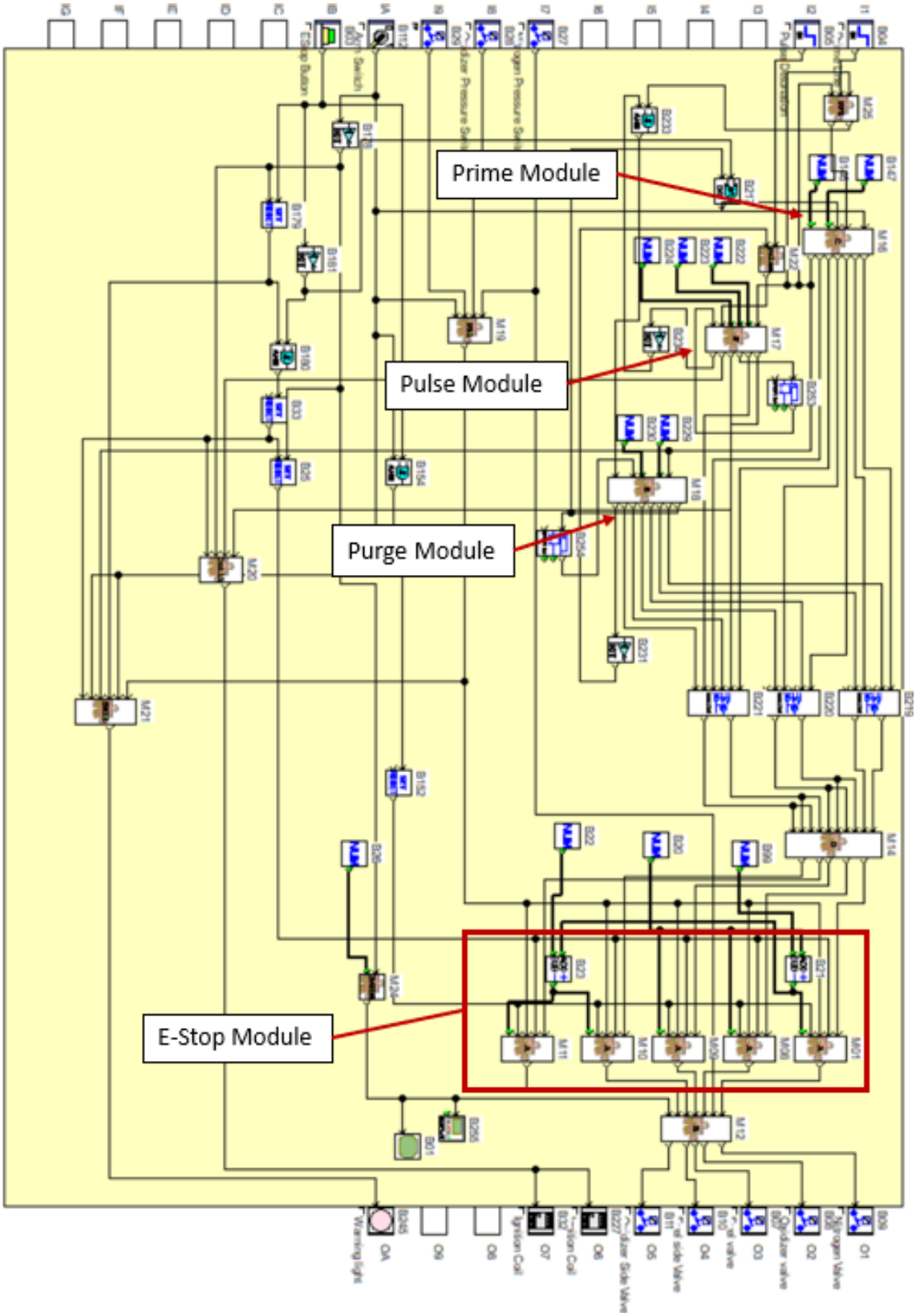

Appendix 3: LabVIEW Control Panel

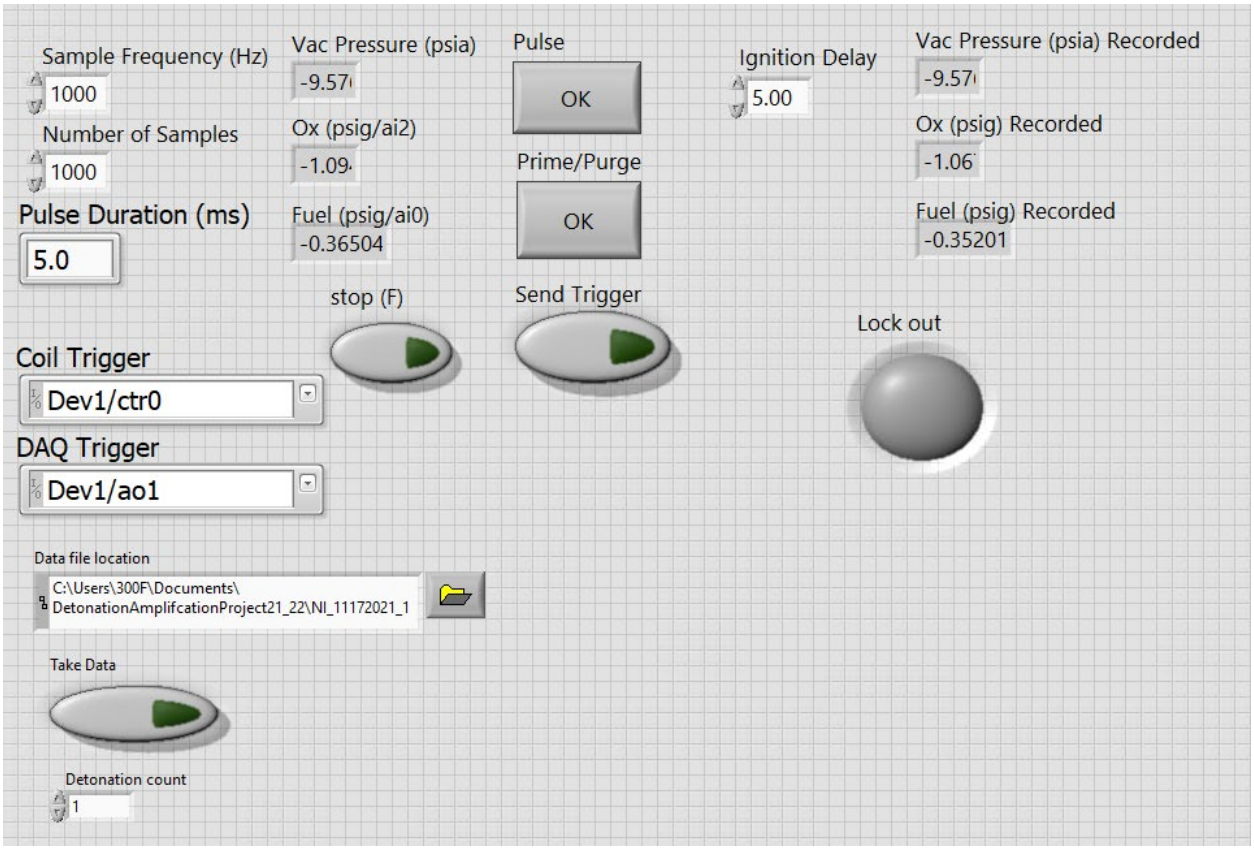

Appendix 4: FEA Simulations for the Optical Test Section Redesigns

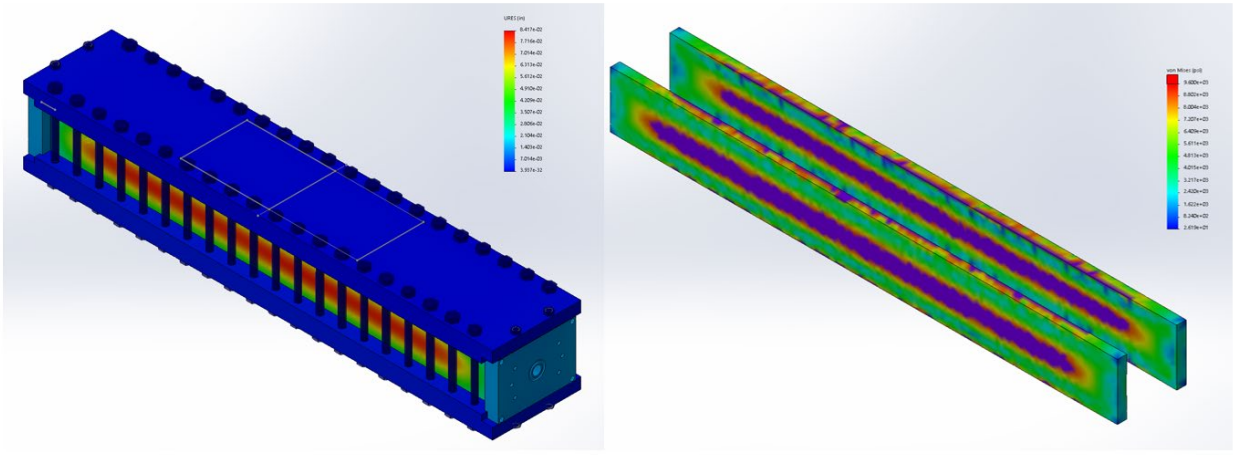

3.1: Redesign 1: Displacement (left) shows a maximum displacement of .08417” and the stress in the window (right) with purple showing the stress is above the ultimate yield strength of polycarbonate at 9600 psi [15]

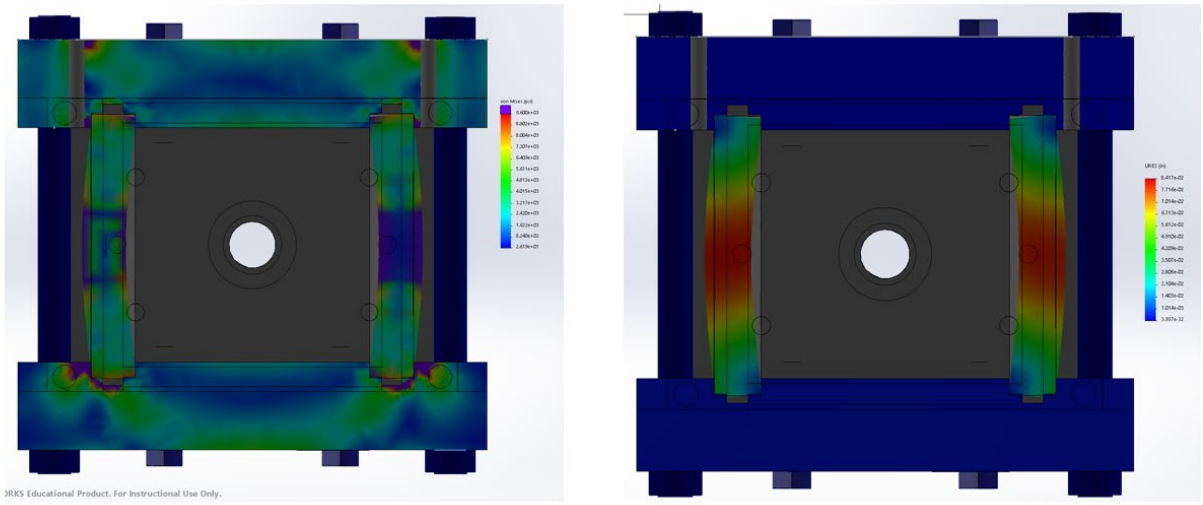

3.2: Redesign 1: Cross-sectional stress (left) and displacement (right) at the mid-point of the chamber with a max displacement of 0.08417” and the purple showing the ultimate yield strength of polycarbonate

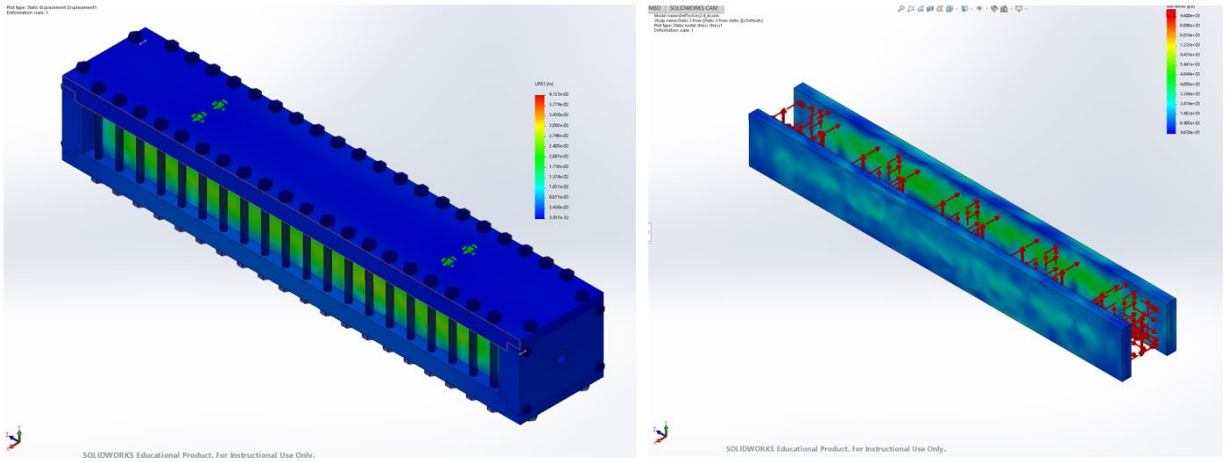

3.3: Redesign 2: Displacement (left) shows a maximum displacement of 0.04123” and the stress in the window (right) with the maximum of the stress scale being the yield strength of polycarbonate

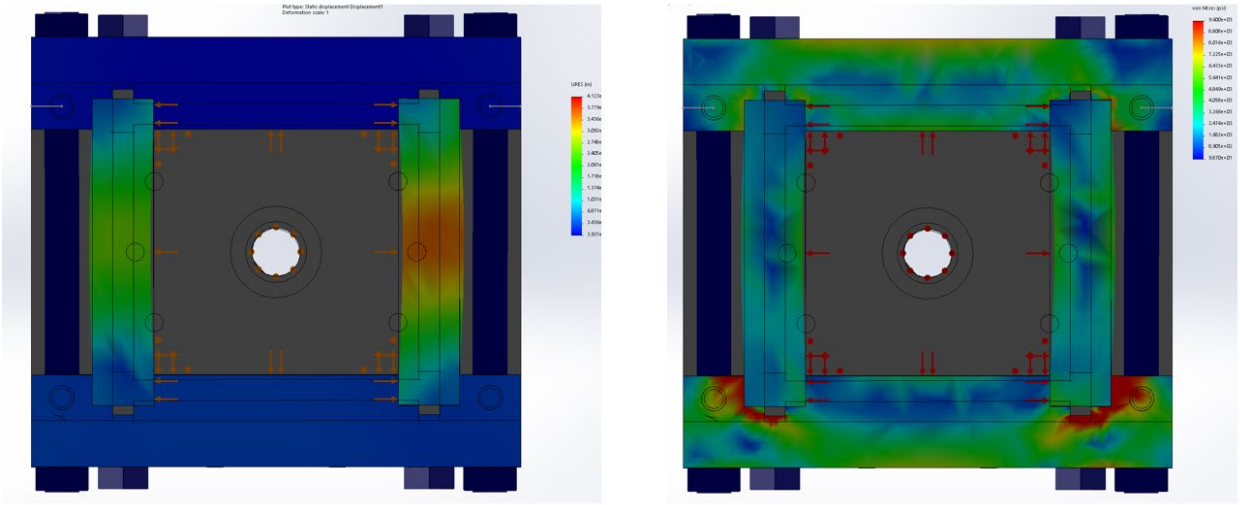

3.4: Redesign 2: Cross-sectional stress (left) and displacement (right) at the mid-point of the chamber with a max displacement of 0.04123” and the maximum of the stress scale being the yield strength of polycarbonate

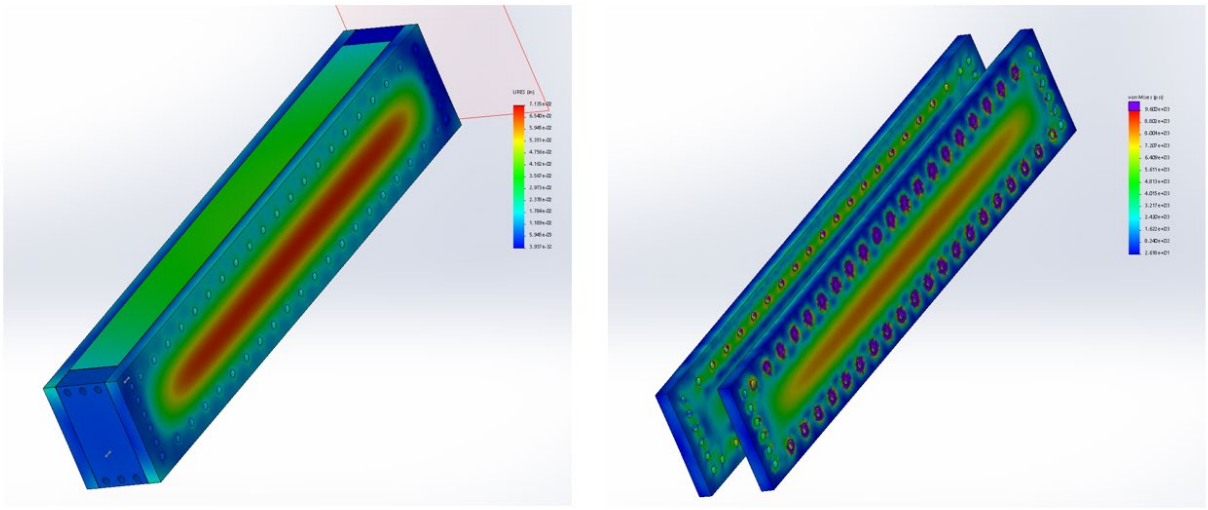

3.5: Redesign 3: Displacement (left) shows a maximum displacement of .07135” and the stress in the window (right) with purple showing the stress is above the ultimate yield strength of polycarbonate

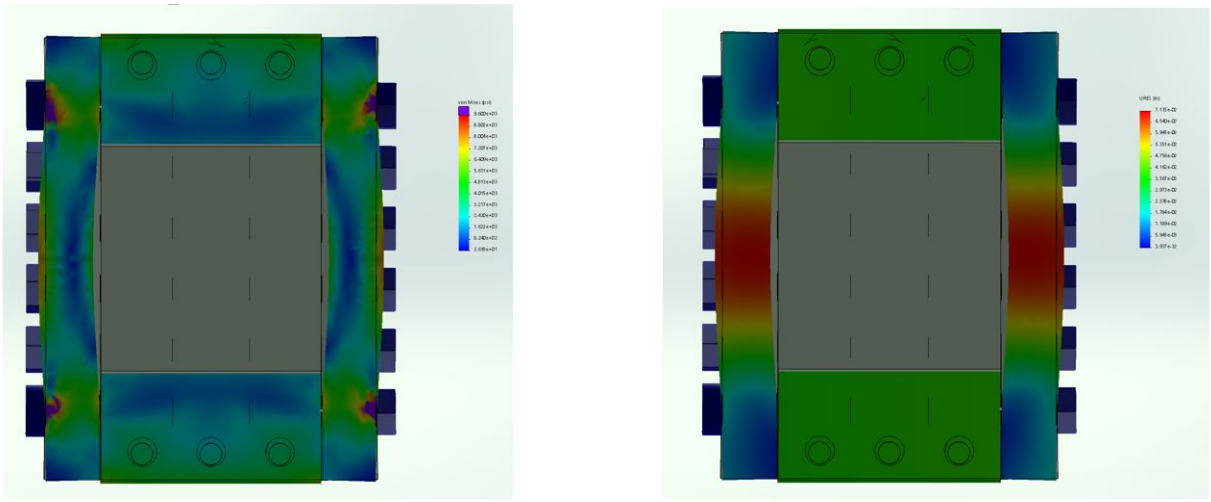

3.6: Redesign 3: Cross-sectional stress (left) and displacement (right) at the mid-point of the chamber with a max displacement of 0.07135” and the purple showing the ultimate yield strength of polycarbonate

Appendix 5: Vacuum System Flow Safety Plots for Fuel Volume Percentage and Mixture Φ

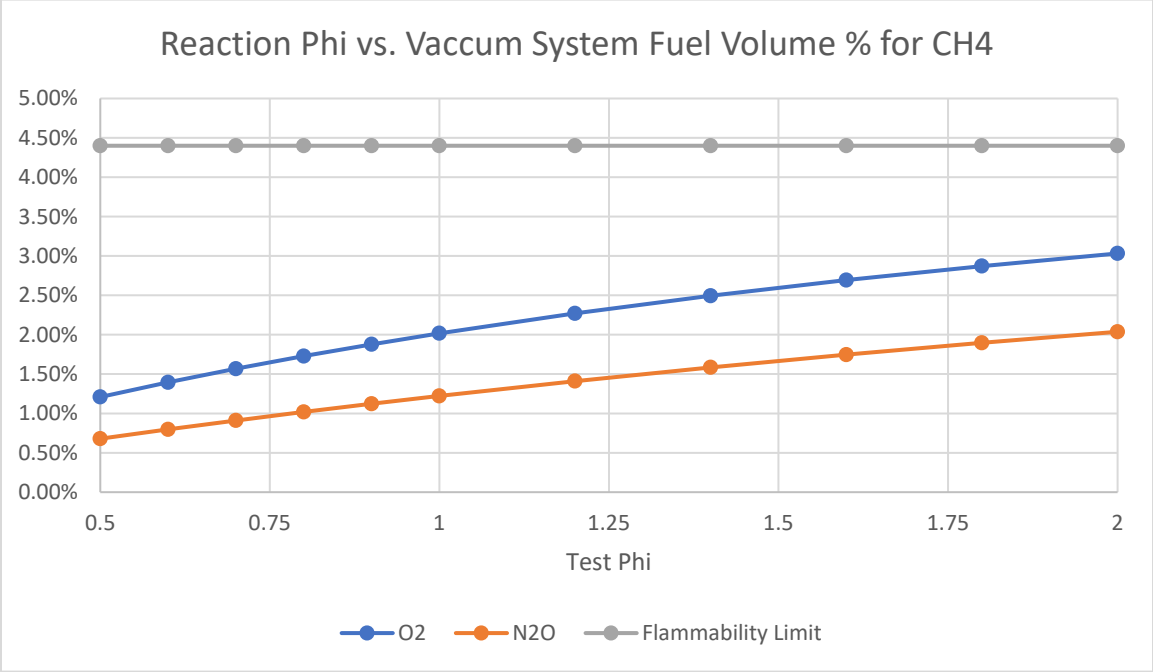

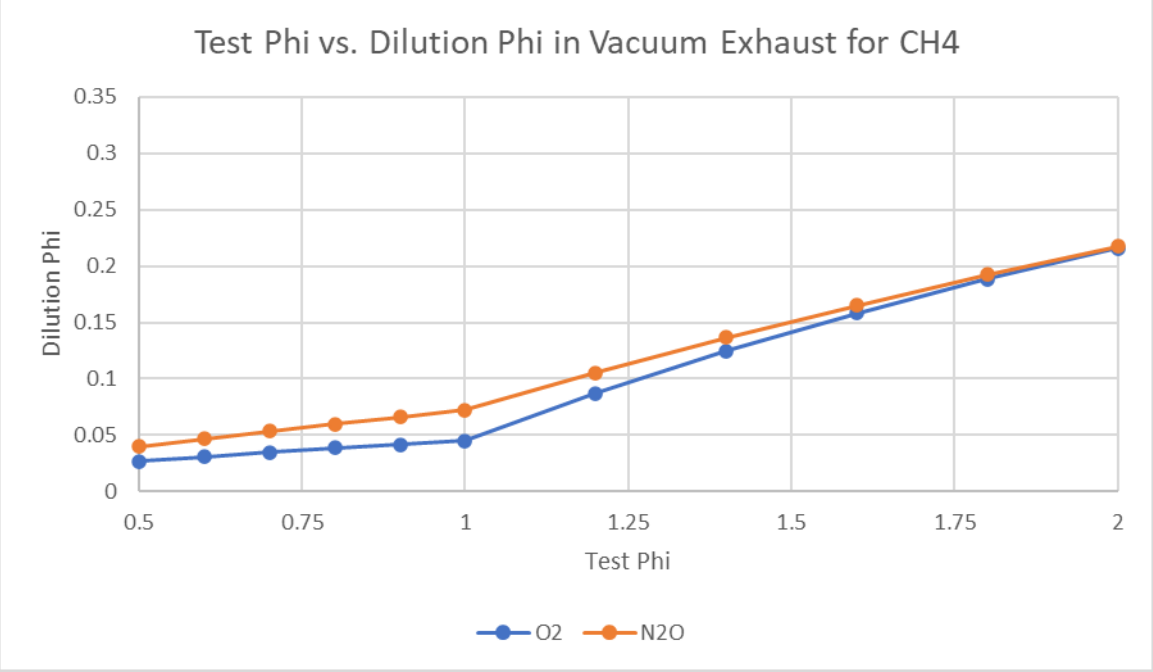

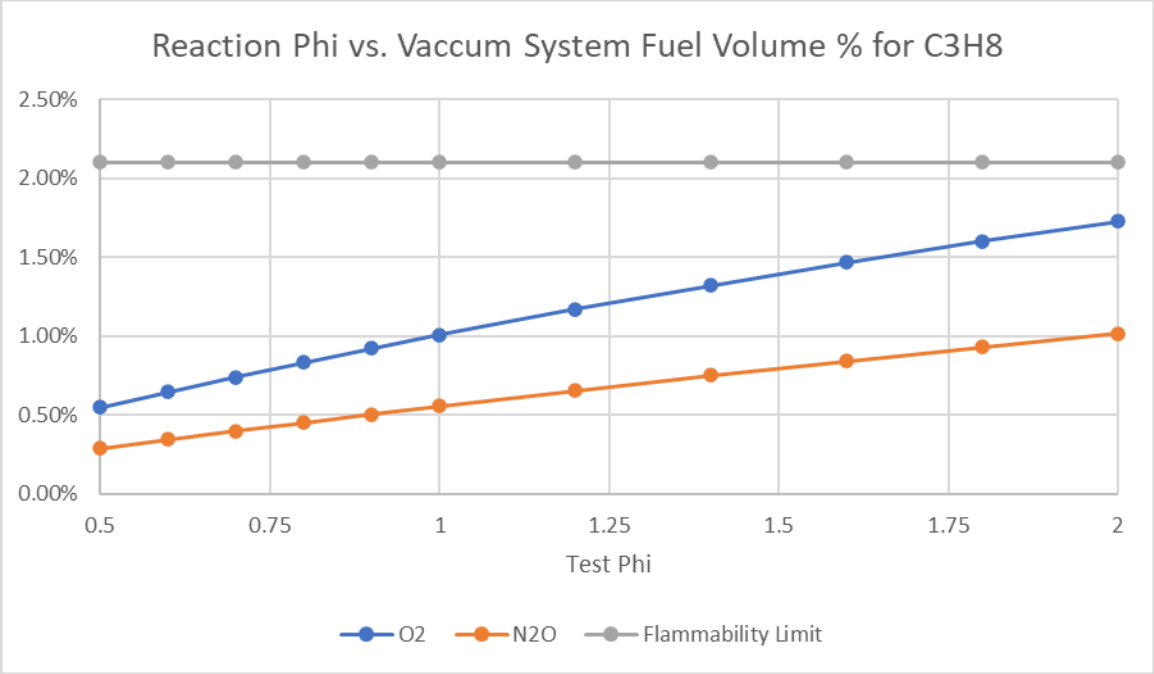
Reaction Phi vs. Vaccum System Fuel Volume % for C3H8
2.50%
2.00%
1.50%
1.00%
0.50%
0.00%
0.5
0.75
1
1.25
1.5
1.75
2
Test Phi
O2
N2O
Flammability Limit

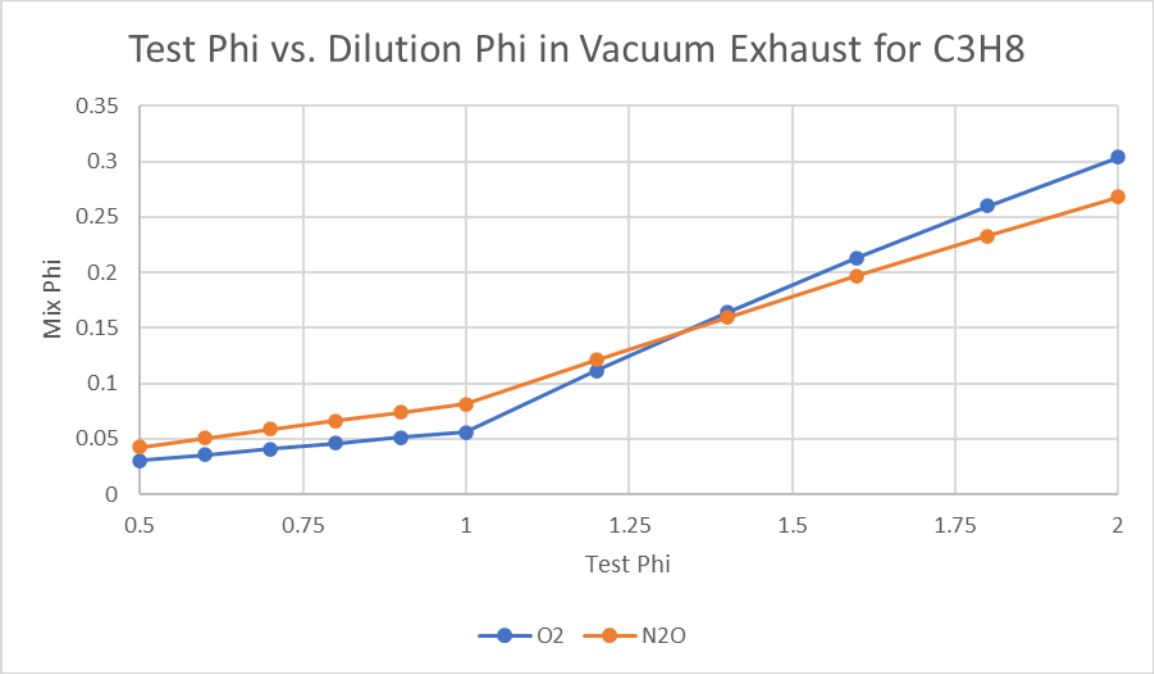
Test Phi vs. Dilution Phi in Vacuum Exhaust for C3H8
0.35
0.3
0.25
0.2
0.15
0.1
0.05
0
Mix Phi
0.5
0.75
1
1.25
1.5
1.75
2
Test Phi
O2
N2O

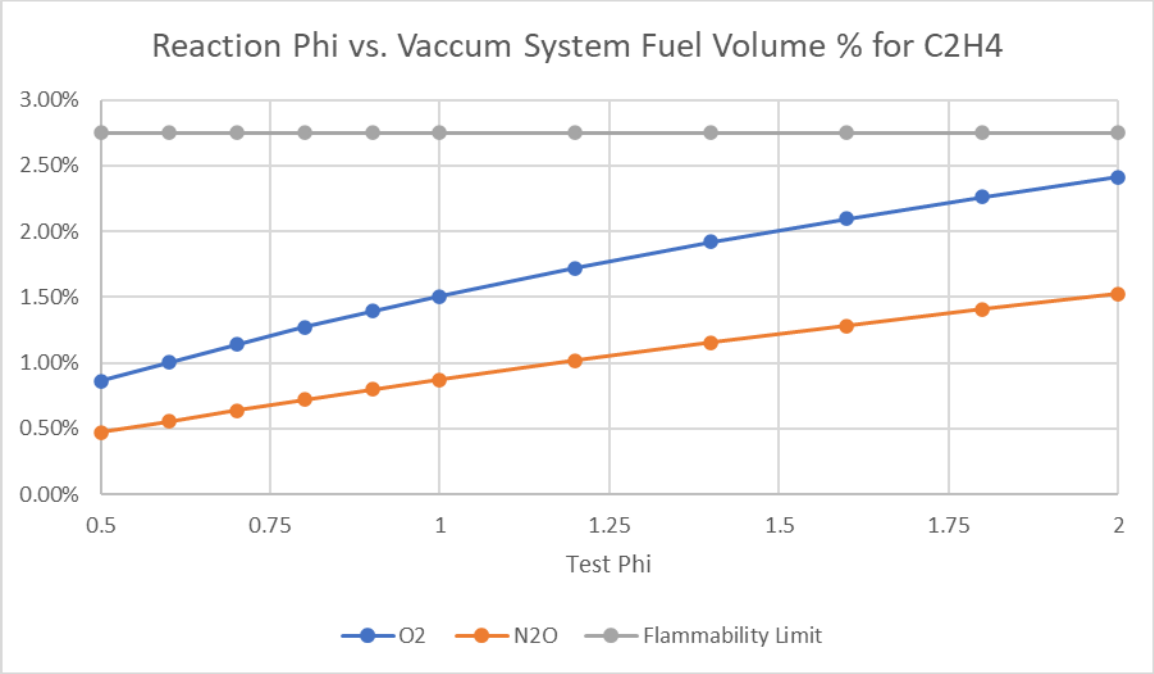
Reaction Phi vs. Vaccum System Fuel Volume % for C2H4
3.00%
2.50%
2.00%
1.50%
1.00%
0.50%
0.00%
0.5
0.75
1
1.25
1.5
1.75
2
Test Phi
O2
N2O
Flammability Limit

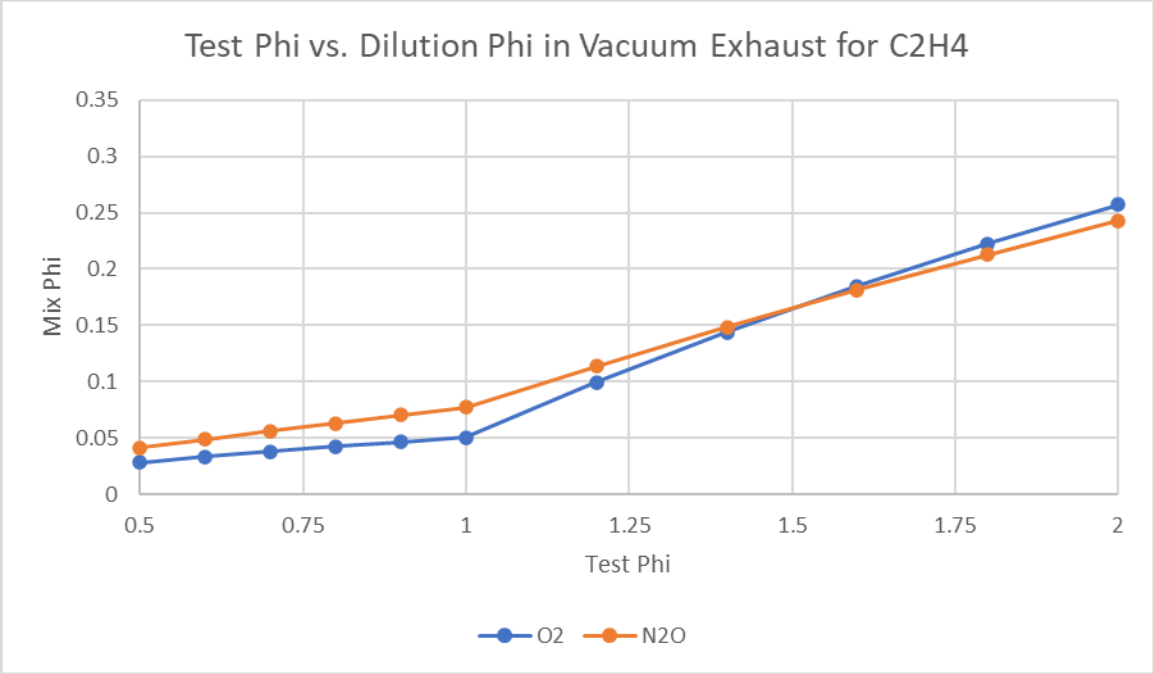
Test Phi vs. Dilution Phi in Vacuum Exhaust for C2H4
0.35
0.3
0.25
0.2
0.15
0.1
0.05
0
Mix Phi
0.5
0.75
1
1.25
1.5
1.75
2
Test Phi
O2
N2O

Appendix 6: Exhaust Flow Safety Calculation for Fuel Volume Percentage and Mixture Φ

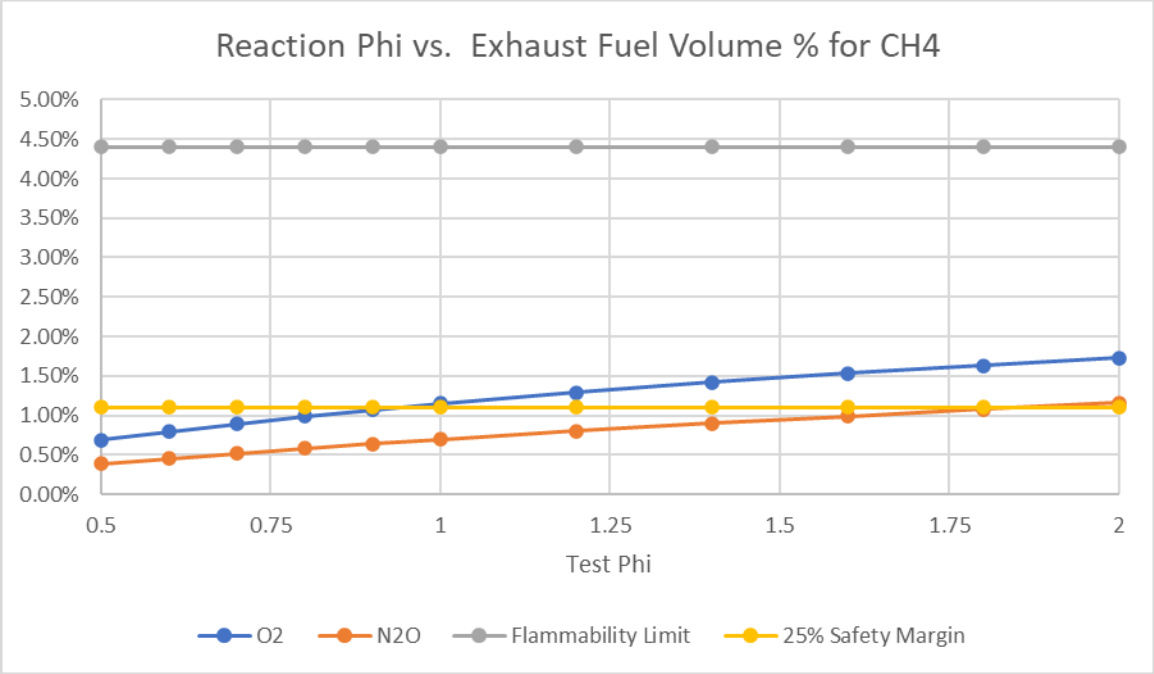

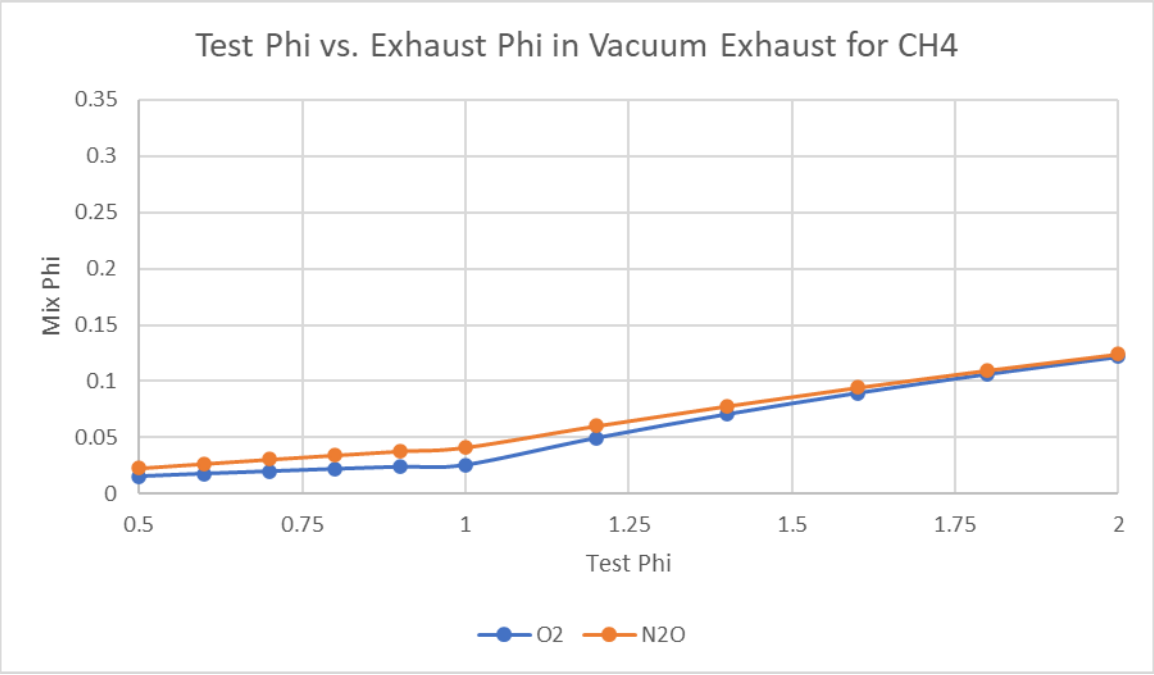

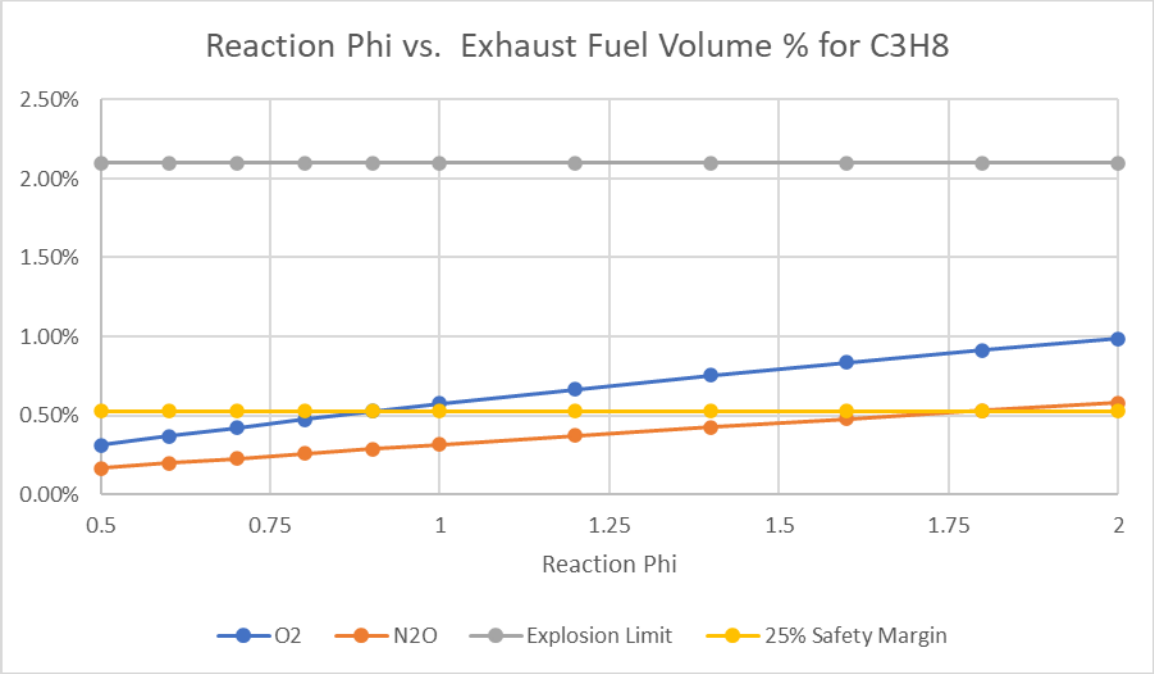
Reaction Phi vs. Exhaust Fuel Volume % for C3H8
2.50%
2.00%
1.50%
1.00%
0.50%
0.00%
0.5
0.75
1
1.25
1.5
1.75
2
Reaction Phi
O2
N2O
Explosion Limit
25% Safety Margin

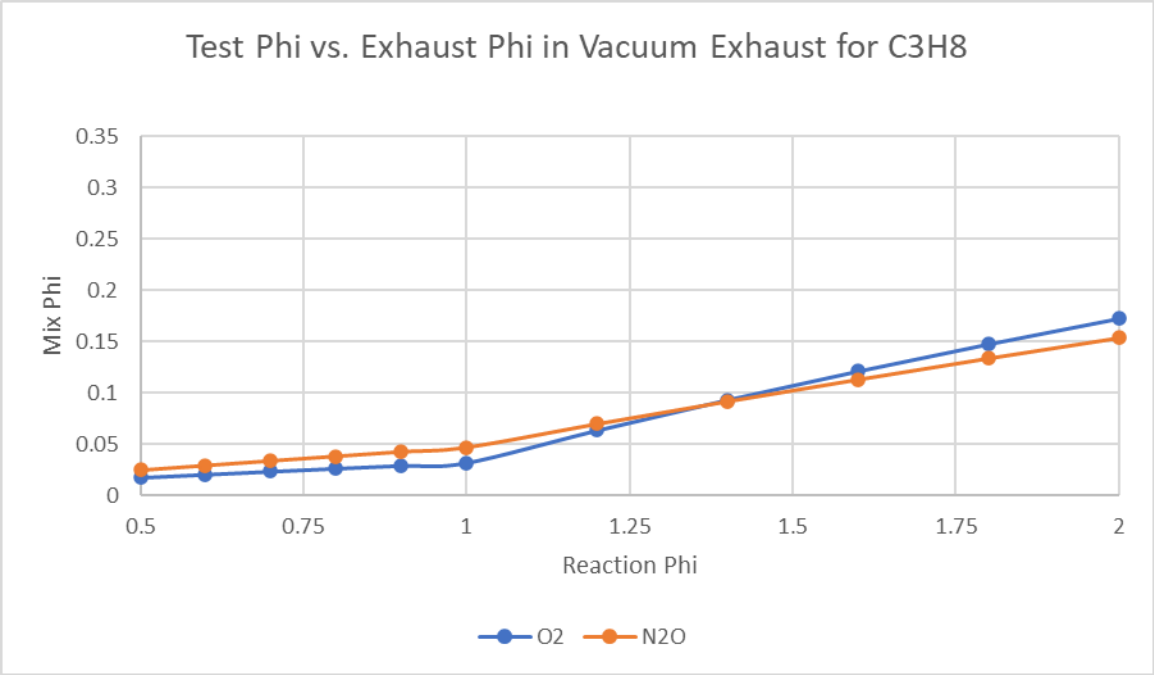
Test Phi vs. Exhaust Phi in Vacuum Exhaust for C3H8
0.35
0.3
0.25
0.2
0.15
0.1
0.05
0
Mix Phi
0.5
0.75
1
1.25
1.5
1.75
2
Reaction Phi
O2
N2O

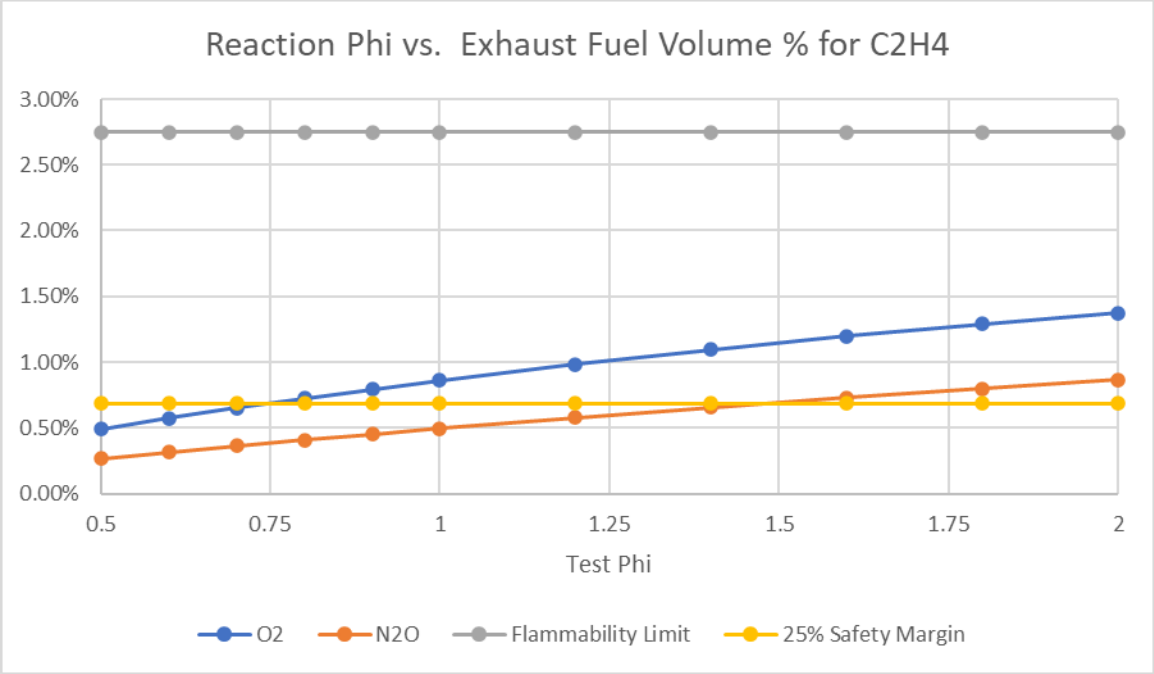
Reaction Phi vs. Exhaust Fuel Volume % for C2H4
3.00%
2.50%
2.00%
1.50%
1.00%
0.50%
0.00%
0.5
0.75
1
1.25
1.5
1.75
2
Test Phi
O2
N2O
Flammability Limit
25% Safety Margin

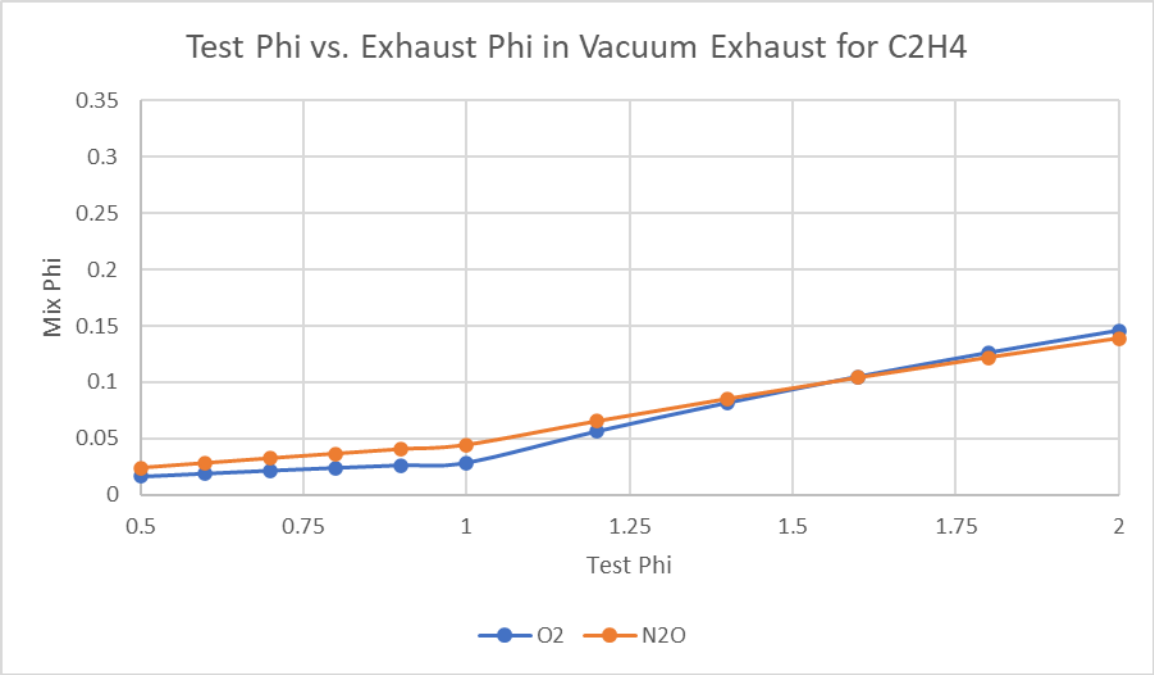
Test Phi vs. Exhaust Phi in Vacuum Exhaust for C2H4
0.35
0.3
0.25
0.2
0.15
0.1
0.05
0
Mix Phi
0.5
0.75
1
1.25
1.5
1.75
2
Test Phi
O2
N2O